Probing Molecular Interactions in Metal-Aβ Complexes and Supramolecular Coiled Coil Assemblies Using Electron Spin Resonance

by

K. Ishara Silva

B.S., University of Peradeniya, Sri Lanka, 2007

Submitted to the Graduate Faculty of the Kenneth P. Dietrich

School of Arts and Sciences in partial fulfillment

of the requirements for the degree of

Doctor of Philosophy

University of Pittsburgh

2015

UNIVERSITY OF PITTSBURGH

DIETRICH SCHOOL OF ARTS AND SCIENCES

This dissertation was presented

by

K. Ishara Silva

It was defended on

December 4th, 2014

and approved by

David. H. Waldeck, Ph.D., Professor, Department of Chemistry

Seth Horne, Ph.D., Assistant Professor, Department of Chemistry

Patrick van der Wel, Ph.D., Assistant Professor, Department of Structural Biology

Dissertation Advisor: Sunil K. Saxena, Ph.D., Professor, Department of Chemistry

Probing Molecular Interactions in Metal-Aβ Complexes and Supramolecular Coiled Coil Assemblies Using Electron Spin Resonance

K. Ishara Silva, PhD

University of Pittsburgh, 2015

In this work we focus on details of Cu(II) coordination in amyloid-β (Aβ) peptide. Aggregation of Aβ, and modulation of morphology of aggregates by divalent metal ions, such as Cu(II) and Zn(II), are important in the etiology of Alzheimer's disease. The metal ion coordination in amyloidogenic proteins is heterogeneous and involves one or more histidine residues. The Aβ peptide contains three histidine residues at positions 6, 13, and 14. The number of histidine residues coordinated to Cu(II) depends on environmental factors such as pH, Cu(II) concentration, presence of other metals, ionic strength etc. With the aid of electron spin resonance (ESR) we show that at physiological pH, Zn(II) ions selectively substitute Cu(II) ions coordinated to Aβ, and disrupt the distribution of Cu(II) population among different coordination modes. We also quantify the number of histidine residues coordinated to Cu(II) at higher pH of 8.7. Our results suggests that Cu(II) coordinated to simultaneous His13-His14 may lead to the formation of Aβ aggregates with more amorphous morphology. Furthermore we suggests the importance of His13 in the formation of ordered β-sheets. Overall we rationalize the impact of metal ion coordination in modulating the morphology of Aβ aggregates.

In the second part of our research we examine the molecular origins of flexibility associated with supramolecular polymer subunits with double electron electron resonance (DEER) spectroscopy. It has been shown that coiled coil subunits appended with different organic linkers, ethylenediamide (EDA) and piperazine (PIP), led to the formation of supramolecular polymer

assemblies with different apparent hydrodynamic radii. With the strategic placement of the spin label near the cross linking site and near the N-terminus we were able to monitor a range of conformations of each subunit when linked with the two linkers. Molecular dynamics simulations guided by DEER distance distributions were conducted to show that the PIP linker stabilizes a folded coiled coil population where the positioning of the cross linking site of outer helices is constrained. We suggest that this subpopulation facilitates the chain propagation in the same direction leading to the formation of polymers with larger hydrodynamic radius.

TABLE OF CONTENTS

LIST OF TABLES

LIST OF FIGURES

PREFACE

First and foremost I would like to thank my research advisor Prof. Sunil Saxena, for the tremendous support and the guidance given throughout my PhD. His patience and mentorship enabled me to become a more productive graduate student.

Then, I would like to thank my committees; Prof. David Waldeck, Prof. Seth Horne, and Prof. Patrick van der Wel for serving in my dissertation committee. My thanks goes to Prof. Renã Robinson for serving in my comprehensive exam committee. I would also like to thank Prof. Daniel Lambrecht for serving as my proposal mentor.

My special thanks goes to all the collaborators I have worked with. Prof. Seth Horne has always been great to work with and his graduate student Nathan Tavenor always tried to give me the best possible samples. It was great fun to work with you guys. Prof. Valerian Kagan was a great inspiration in our work in *cytochrome c*. Prof. Daniel Lambrecht was always great to talk to about quantum mechanical calculations related to ESR measurements.

I would like to acknowledge all the past and present group members of the Saxena group. Dr. Katherine Stone, Dr. Sangmi Jun, Dr. Zhongyu Yang, Dr. Sharon Ruthstein, Dr. Jessica Sarver, Dr. Ming Ji, Gayathri Rajapakse, Marshall McGoff, Yoojin Lee for all the help given during my stay in Saxena lab. Dr. Byong-kyu Shin was a great mentor when I started the grad school and taught me the basics in ESR and instrumentation. Brian Michael was a great undergrad I had the privilege of working with. Special thanks goes to soon to be Dr. Tim Cunningham who was there to share all my ups and downs in grad school. Your friendship is really valued and appreciated. Matt Lawless was a great friend willing to help out anyway he can and it was a pleasure to see him blossoming as a scientist.

I would not be here today defending my PhD if not for my loving parents. Thank you very much for the great foundation you laid, to be the person who I am today. My two brothers have always been a great source of inspiration.

Finally, the person who help me out the most during my PhD, my lovely wife Masha. She was patient enough to listen to all my frustrations and successes in grad school. She did not complain a bit when we had to live through minimal resources during the final stages of my PhD. You helped me out a lot to get through the rocky periods sorry for taking a long time to finish my PhD, when I promised otherwise when we got married. Hopefully we can catch up the times that we missed.

1.0 INTRODUCTION

Figure 1-1, shows the overall interests that drive the work described in this thesis. We use electron spin resonance (ESR) spectroscopy to elucidate the coordination environment of Cu(II) ions in Amyloid-β (Aβ). The aggregation of Aβ is inherently linked with the pathogenesis of Alzheimer's disease.[1-2] Earlier work by our group indicate that the overall morphology of Aβ aggregates depends on Cu(II) concentration (cf. Atomic force microscopy images shown in Figure 1-1A).[3-4]As the morphology of the aggregates are related to the toxicity in Alzheimer's disease, it is critical to understand how metal ion binding affects the overall morphology.[5] There are three histidine residues found at positions 6, 13 and 14 in Aβ and Cu(II) coordination involves different number of histidine residues bound to Cu(II) in different coordination modes as shown in Figure 1-1A.[5-6] The specific Cu(II) coordination environment in Aβ is affected by factors such as pH, ionic strength, concentration of Cu(II), and the presence of other metal ions such as Zn(II).[5, 7] The different coordination modes can have different roles in the etiology of the Alzheimer's disease. Therefore, a thorough analysis of the subcomponent populations and how they change with environmental factors (eg: pH, presence of Zn(II)) is performed in this thesis. As described in Figure 1-1A, we use continuous wave (CW) ESR spectroscopy to obtain information on directly coordinated ligand atoms. In this research we use two pulsed ESR methods [electron spin echo envelope modulation (ESEEM) and hyperfine sublevel correlation (HYSCORE)] to probe and quantify the Cu(II) histidine coordination in Aβ.

In the next section we probe the structural flexibility of protein based supramolecular polymers. The genesis of this work has been the early efforts by the Horne group that showed, supramolecular polymers made with subunits of coiled coil peptides appended with small organic linkers ethylenediamide (EDA) and piperazine (PIP) formed assemblies of different sizes (Figure 1-1B).[8] PIP linked peptides led to the formation of assemblies with a larger apparent hydrodynamic radius,[8] than the EDA linked peptides as shown in Figure 1-1B. To understand the molecular basis of this observation we isolated a single subunit of the polymer and used pulsed ESR method double electron electron resonance (DEER) along with site directed spin labeling (SDSL) (Figure 1-1B). Molecular dynamics aided modeling of the DEER data was used to show the roles of different conformer sub populations that dictate the physical properties of the supramolecular polymers. Understanding of molecular level details enables scientist to optimize the design of the supramolecular polymers.

In subsequent sections of chapter 1, we will discuss the ESR techniques used in this thesis.

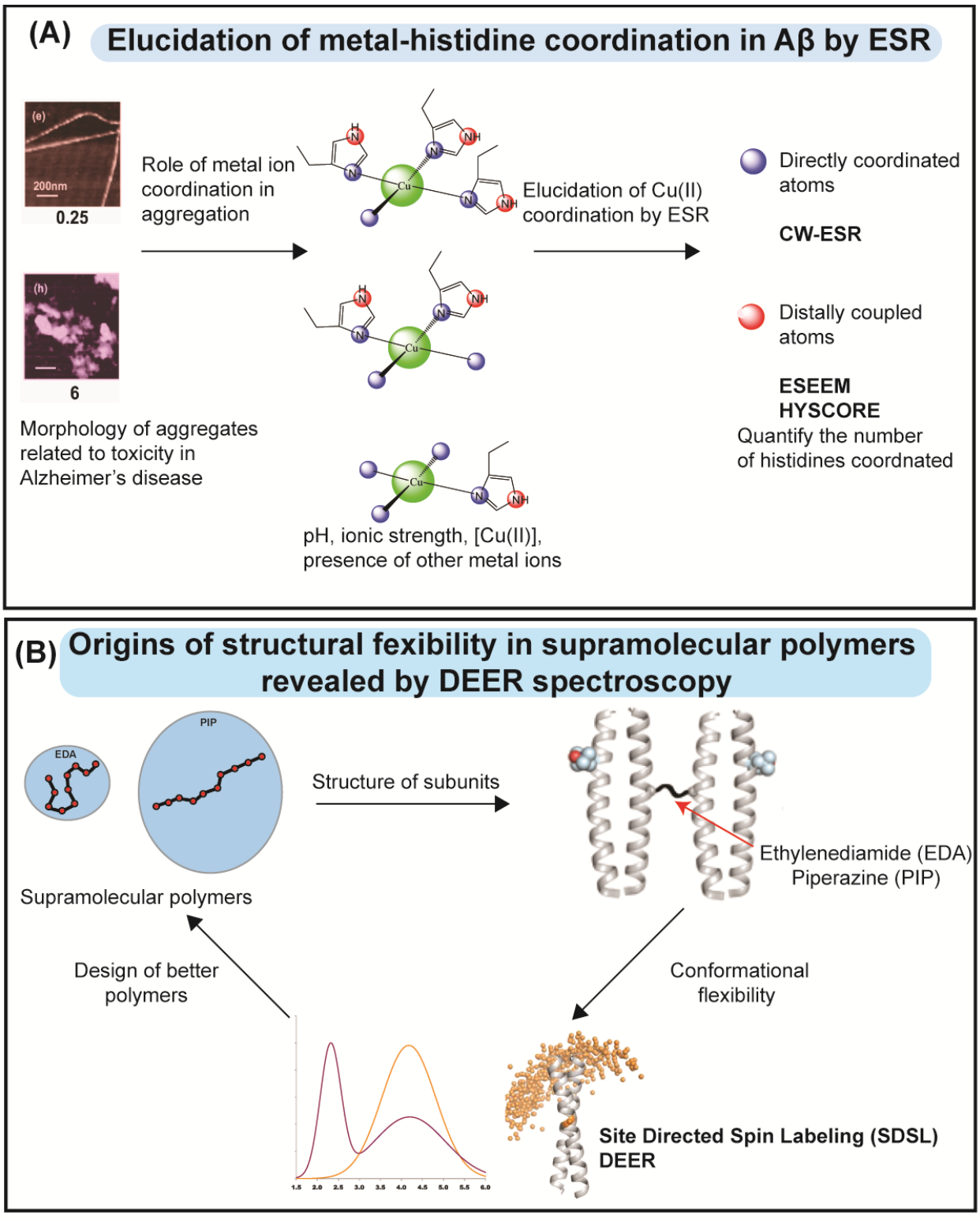

Figure 1-1 Summary of techniques used to (A) elucidate Cu(II)-histidine coordination in Aβ (B) and to probe the structural flexibility observed in supramolecular polymers.

1.1 ELUCIDATION OF Cu(II) COORDINATION IN PROTEINS/PEPTIDES USING ESR SPECTROSCOPY

Copper is an essential metal for biological function, and nature has evolved to form highly sophisticated mechanisms which allow organisms to secure, transport, sequester and transfer copper.[9-10] These mechanisms allow organisms to maintain homeostasis and prevent the accumulation of copper to toxic levels.[10] There are two main classes of copper proteins in nature. First, proteins that utilize copper as a cofactor where a specific function is carried out and second, proteins that transport copper as cargo.[10] Exploring the metal ligand coordination enables scientists to understand chemical principles used by nature to handle a potentially toxic substance for essential function.

Most of the copper binding sites in nature use histidine, cysteine and methionine residues as ligands. This phenomena is rationalized by the principle of the hard and soft acids and bases, where soft Lewis acids react with soft Lewis bases, and hard Lewis acids react with hard Lewis bases.[11-12] There are two oxidation states of copper found in nature, both capable of accepting electrons and acting as Lewis acids. Cu(I) is a soft acid, while Cu(II) is a borderline acid.[11] Hence, copper binding sites are expected to be dominated by amino acids with soft or borderline ligands. Amino acids with nitrogen or sulfur ligand donor atoms, which are soft or borderline Lewis bases, are preferred over amino acids that provide oxygen donors (hard Lewis bases).[12]

As explained in the principles of ligand field theory, the binding geometry of a metal ion is dictated by the number of *d* electrons in the valence shell and the number/type of coordinating ligands.[13] Cu(I) is a d^{10} system and due to the symmetry associated with the electron configuration, molecular geometries related with ligand field stabilization (eg: square planar, trigonal bipyramidal) are not observed.[13] Cu(I) systems in nature often employ linear, trigonal planar or

tetrahedral geometries where 2, 3, and 4 ligands are coordinated, respectively. On the other hand Cu(II), a d^9 system, exhibits geometries based on ligand field stabilization energies.[13] Cu(II) is often coordinated to 4, 5, and 6 ligands with square planar, square pyramidal, and axially distorted octahedral geometries, respectively.[13] Axially distorted octahedral geometries are observed as a result of Jahn-Teller distortion.[14] In this thesis we will focus on coordination of Cu(II), as this oxidation state is paramagnetic and ESR active while Cu(I) is diamagnetic and ESR silent.

ESR of a free electron: ESR is a spectroscopic method used to probe systems containing unpaired electrons. The simplest system that can be studied by ESR is a free radical. If we assume the unpaired electron is a free electron, with a mass of m_e and a charge of e, the spin angular momentum gives rise to a magnetic moment of

$$\overrightarrow{\mu}_e = -g_e\beta_e\overrightarrow{S} \qquad (1)$$

where β_e is the Bohr magneton defined by $\beta_e = e\hbar/2m_e$ ($\hbar$ is the reduced Planck's constant). g_e is the g factor of a free electron which is ~ 2.00232, and $\overrightarrow{S}$ is the electron spin angular momentum. The degeneracy of the electron spin states, characterized by quantum number m_s = ±1/2, is lifted by the application of an external magnetic field (B_0) as shown by Figure 1-2. This interaction between the magnetic moment and the external magnetic field is called the Zeeman interaction. The Hamiltonian that describes the Zeeman interaction for a free electron can be written as,

$$\hat{\mathcal{H}} = \beta_e g_e \overrightarrow{B}.\overrightarrow{S} = m_s \hbar g_e \beta_e B_0 \qquad (2)$$

The transition between the two states can be induced by the application of radiation in the microwave frequency (υ), and the resonance condition is given by,

$$\Delta E = h\upsilon = g_e\beta_e B_0 \hbar \qquad (3)$$

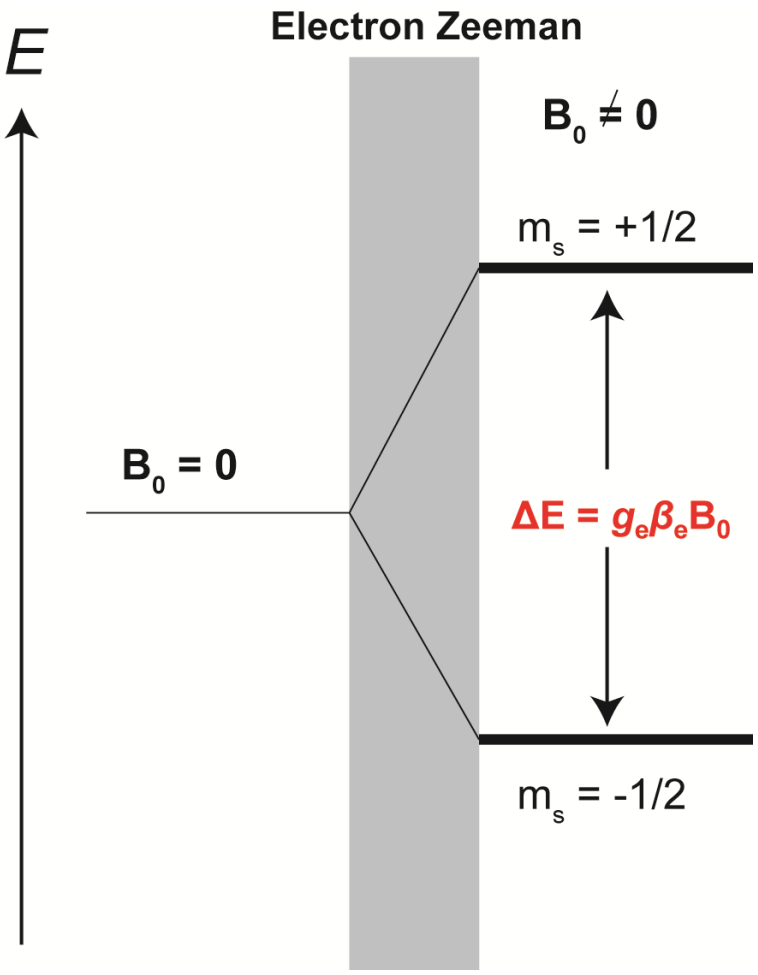

Figure 1-2 Energy levels of a free electron placed in a magnetic field. The separation between the two energy states depends on the external magnetic field.

Equation 3 depicts the fundamental equation for ESR spectroscopy. At thermal equilibrium there is a slight excess of electrons in the m_s = -1/2 state as compared to the m_s = +1/2 state. The ratio of the populations is given by the Boltzmann equation,

$$N_+/N_- = \exp - g_e\beta_e B_0/kT \qquad (4)$$

where *k* is the Boltzmann's constant and *T* is the absolute temperature. Although the probabilities of the stimulated emission and absorption are equal, due to the population difference at the resonance condition there is a net absorption. The electrons in the lower energy state m_s = -1/2, absorb energy from microwave radiation and are promoted to the higher energy level m_s = +1/2, giving rise to the ESR spectrum. For more complex systems, like Cu(II), additional terms appear in the Hamiltonian which will be discussed in the following sections.

ESR spectroscopy on Cu(II) complexes: In this section we will focus on Cu(II)-histidine coordination, given that histidine is the most common Cu(II) ligand in proteins.[15] Histidine contains an imidazole functional group which contains two nitrogen atoms as shown in Figure 1-3.[10, 15] The pKa value of the imidazole ring proton is ~6 for the free amino acid.[10] The pKa values are altered by the protein environment and the coordinated metals.[16] As there are two nitrogen ligands on either side of the imidazole ring, histidine residues often can act as bridging ligands.[10]

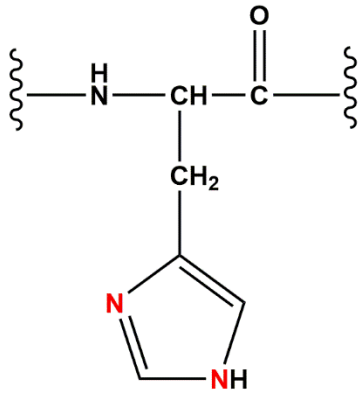

***Cu^{2+} preference**

***pKa~6 for the conjugate base (imidazolium cation)**

***Neutral or cationic, hydrophilic ~pH 7.4**

Figure 1-3 Chemical structure of histidine. The two nitrogen atoms in the imidazole ring are shown in red. A summary of chemical properties of the histidine is provided.

Copper coordination in amyloidogenic proteins such as amyloid-β, α-synuclein, and prion involves multiple histidine residues.[17] The copper coordination sites in these proteins are classified as type II copper centers (T2Cu).[18] In T2Cu centers, copper is predominantly coordinated by histidine residues mixed with oxygen containing ligands.[18] Figure 1-4A shows a type II Cu(II) complex we studied in this thesis. There are four nitrogen ligands equatorially coordinated to Cu(II), with three from a chelating ligand and one from the imidazole ring. The unpaired electron spin on Cu(II) interacts with the applied magnetic field and the surrounding nuclei such as Cu, ^{14}N and ^{1}H (highlighted by red circles in Figure 1-4A). The corresponding spin Hamiltonian for this system is,

$$\widehat{\mathcal{H}} = \widehat{\mathcal{H}}_{ez} + \widehat{\mathcal{H}}_{hf} + \widehat{\mathcal{H}}_{nz} + \widehat{\mathcal{H}}_{nq}$$

$$\widehat{\mathcal{H}} = \beta_e \overrightarrow{B}.\ \overleftrightarrow{g}.\overrightarrow{S} + \sum_{i=1}^{k} \overrightarrow{S}.\ \overleftrightarrow{A}_i.\ \overrightarrow{I_i} - \beta_n \sum_{i=1}^{k} \left(\overrightarrow{B}.\ \overleftrightarrow{g}_{in}.\ \overrightarrow{I_i}\right) + \sum_{i=1}^{k} \overrightarrow{I_i}.\ \overleftrightarrow{Q}_i.\ \overrightarrow{I_i} \qquad (5)$$

The four major terms in the equation are the electron Zeeman interaction ($\widehat{\mathcal{H}}_{ez}$), the electron-nuclear hyperfine interaction ($\widehat{\mathcal{H}}_{hf}$), the nuclear Zeeman ($\widehat{\mathcal{H}}_{nz}$), and the nuclear quadrupole interaction ($\widehat{\mathcal{H}}_{nq}$). Also, β_e is the Bohr magneton, β_n is the nuclear magneton, $\overrightarrow{B}$ is the external magnetic field, $\overleftrightarrow{g}$ and $\overleftrightarrow{g}_{in}$ are the g-tensor of the electron spin and the i th nuclear spin. $\overleftrightarrow{A}_i$ and $\overleftrightarrow{Q}_i$ are the hyperfine tensor and nuclear quadrupole tensor, respectively. $\overrightarrow{S}$ and $\overrightarrow{I_i}$ are the electron and nuclear spin angular momentums, respectively.

Figure 1-4B shows the CW-ESR spectrum of a Cu(II) imidazole complex at 293K. This spectrum is helpful to briefly describe spectral features before we go into more details. The ESR signal is centered at ~3250 G (~9730 MHz) due to the electron Zeeman interaction ($\widehat{\mathcal{H}}_{ez}$). As we will see below each hyperfine interaction causes a splitting in the ESR spectrum. The spectrum contains four peaks with peak widths of ~75G (~225 MHz) separated by ~ 70 G (~ 210 MHz). These peaks are observed due to the hyperfine interaction ($\widehat{\mathcal{H}}_{hf}$) of the Cu(II) nucleus. The

hyperfine interaction of the ^{14}N directly coordinated to Cu(II) is ~ 15 G and are lost in the peak widths. Hyperfine interaction of ^{1}H is even smaller in magnitude and not resolved. As given in equation 5, the nuclear Zeeman interaction depends on the nuclear Bohr magneton. The Bohr magneton of an electron (~9.274 x 10^{-24} J/T) is ~1864 times greater than the nuclear Bohr magneton of a proton (~5.050 x 10^{-27} J/T). Hence, the nuclear Zeeman interaction has a magnitude that is less than 2 G and is not resolved in the peak widths of ~75 G. The non-spherical charge distribution in nuclei with spin $I \geq 1$ gives rise to a nuclear quadrupole interaction (4^{th} term equation 5). Typically the magnitude of the quadrupole interaction is ~ 1G and is not resolved in the much larger peak widths. Hence, for CW-ESR, equation 5 can be simplified as;

$$\hat{\mathcal{H}} = \hat{\mathcal{H}}_{ez} + \hat{\mathcal{H}}_{hf} = \beta_e \overrightarrow{B}.\ \overleftrightarrow{g}.\overrightarrow{S} + \overrightarrow{S}.\ \overleftrightarrow{A}_{Cu}.\ \overrightarrow{I_{Cu}} \qquad (6)$$

At room temperature, when the rotational motion of the molecules is faster than the time scale of the ESR experiment, the anisotropy of the *g* and the *A* tensors are averaged out. Hence, at room temperature, under the high field approximation equation 1-6 can be rewritten as,

$$\hat{\mathcal{H}} = \hat{\mathcal{H}}_{ez} + \hat{\mathcal{H}}_{hf} = g_{iso}\beta_e B_0 \hat{S_z} + A_{iso}\hat{S_z}\hat{I_z} \qquad (7)$$

where *z*-axis is defined as the direction of the external magnetic field B_0, and $\hat{S_z}$ and $\hat{I_z}$ are the *z*-components of the angular momentums of Cu(II) unpaired electron the Cu(II) nuclear spin. For Cu(II), where the nuclear spin (I) is 3/2, the interaction between the electron spin and the Cu(II) nucleus results in four possible sub states shown in Figure 1-5. The peaks corresponding to these four transitions are observed in the CW-ESR spectra acquired at 293 K. The four peaks are separated by ~ 70 G which is the isotropic hyperfine value, A_{iso} for Cu(II) in this imidazole complex. (Figure 1-4B upper panel)

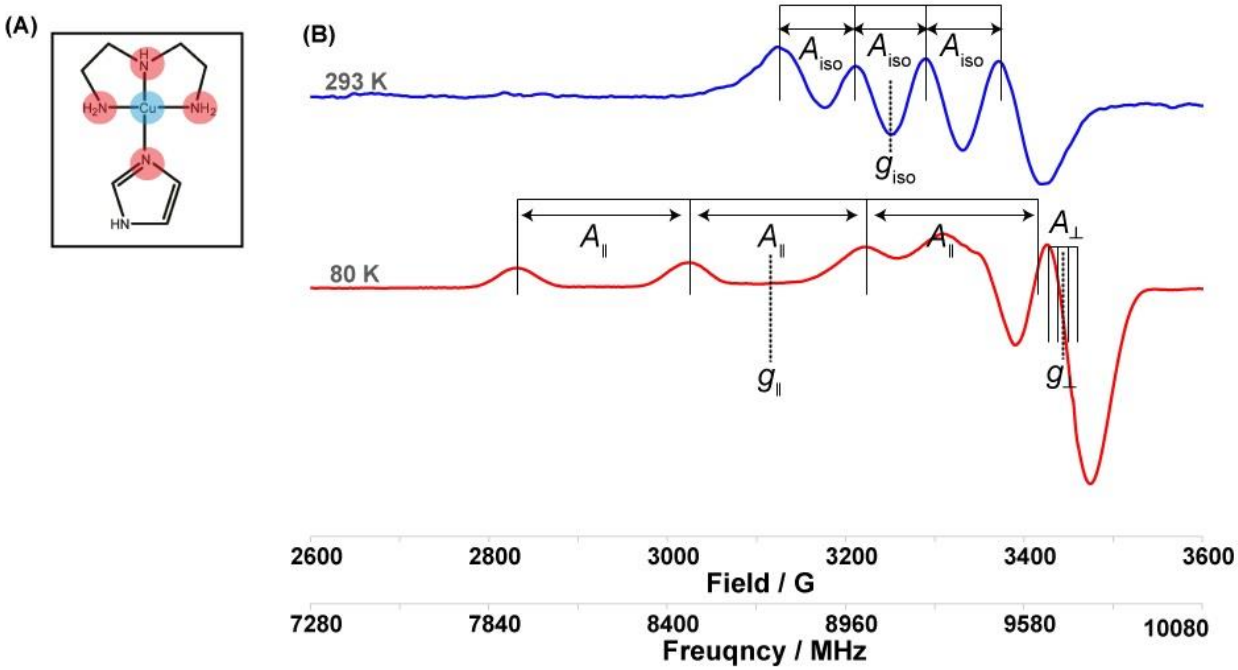

Figure 1-4 (A) Structure of an imidazole-Cu(II) complex used in this thesis (B) The upper panel shows the CW-ESR spectrum acquired at 293 K; the lower panel shows the spectrum acquired at 80 K.

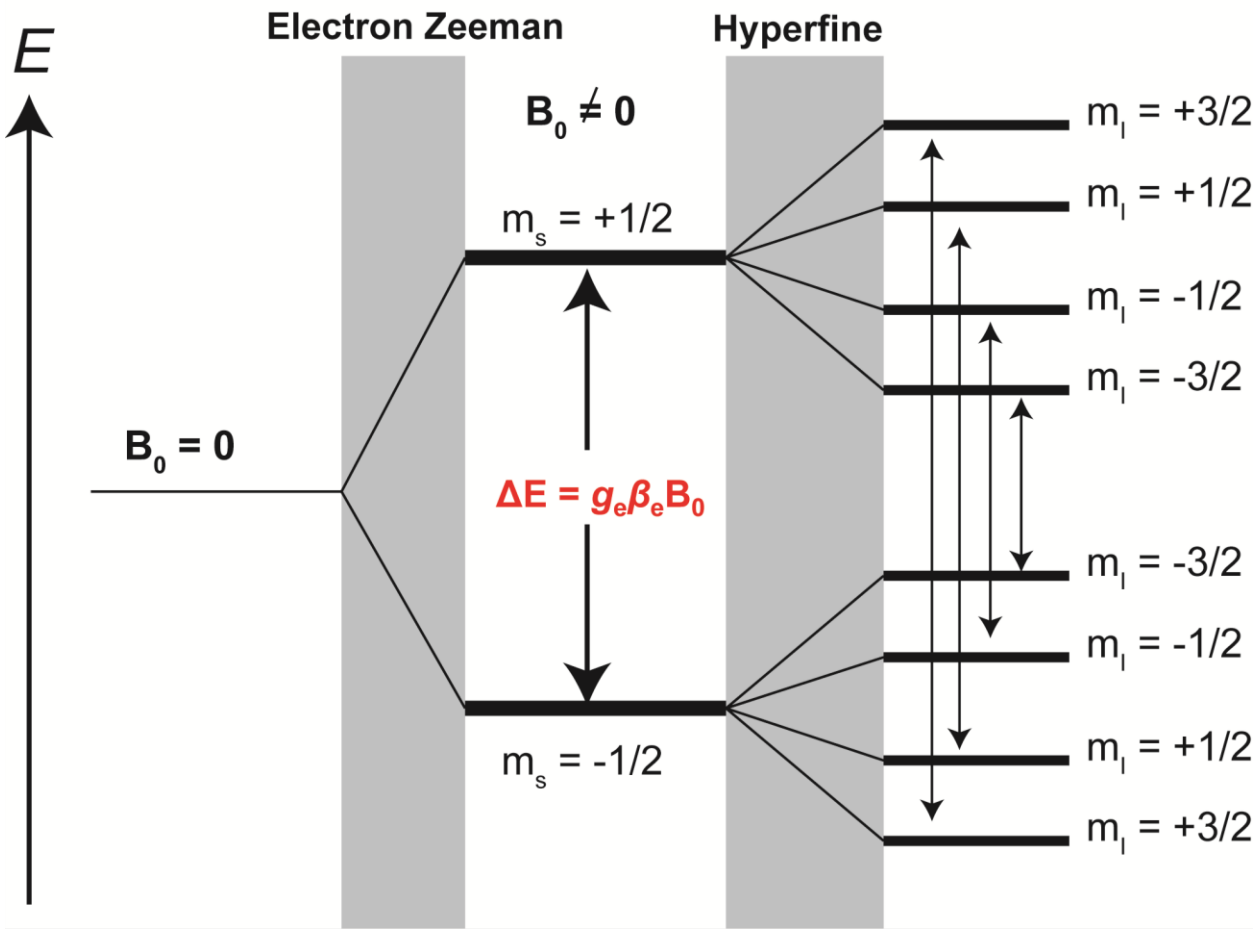

Figure 1-5 The energy level diagram for a Cu(II) with isotropic *g* and *A* values. Application of the magnetic field lifts the degeneracy of the Zeeman levels. The hyperfine interaction further splits the levels. The allowed ESR transitions are shown by arrows.

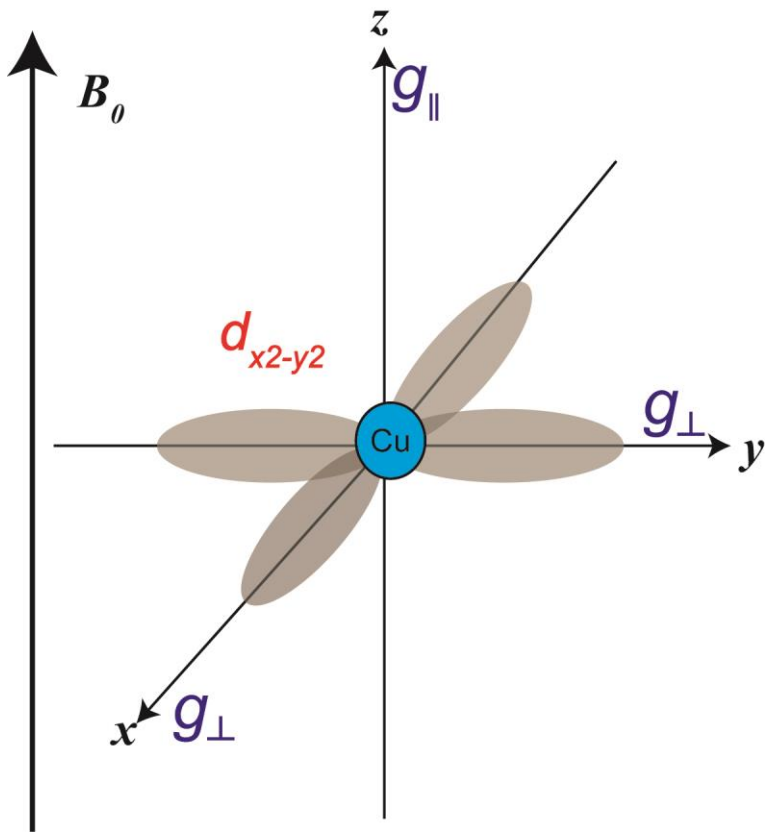

Figure 1-6 The origin of axial symmetry in type II Cu(II) complexes. The unpaired electron is delocalized in the $3d_{x^2-y^2}$ orbital. Values of *g* in the *xy* plane of the molecule are the same and are defined as $g_{\perp}$, and the value of *g*, parallel to the symmetry axis z is defined as $g_{\parallel}$.

At lower temperatures, the rotational motion of the molecules is slow enough, that we can detect values of g and A at different directions of the molecule. Type II copper complexes are axially symmetrical, due to the square planar geometry as shown in Figure 1-6. The values of the g-tensor and A-tensor on the equatorial plane (xy plane in Figure 1-6) of the molecule are the same i.e: $g_{xx} = g_{yy}$ ($g_{\perp}$) and $A_{xx} = A_{yy}$ ($A_{\perp}$) (Figure 1-6). The values of the g-tensor and A-tensor perpendicular to the equatorial plane of the molecule are defined as g_{zz} ($g_{\parallel}$) and A_{yy} ($A_{\parallel}$). Hence, the CW spectrum will be a result of superposition of the all possible orientations with respect to the external magnetic field and will broadened out at lower temperatures. Figure 1-4B lower panel shows the CW-ESR spectrum of the one imidazole-Cu(II) complex at 80 K.

Peisach and Blumberg have shown that the $g_{\parallel}$ and the $A_{\parallel}$ values of the central Cu(II) depends on the chemical nature of directly coordinated atoms.[19] This trend arises from the different electronegativities associated with the ligand atoms. As shown in Figure 1-7, they showed that the $g_{\parallel}$ and the $A_{\parallel}$ values vary with the number of nitrogen and oxygen atoms equatorially coordinated to Cu(II). There is significant overlap (Figure 1-7) which can lead to ambiguities in assignments. Furthermore, the distortions from the square planar to tetrahedral geometry increases the $g_{\parallel}$ and decreases the $A_{\parallel}$.[20] Hence, this method is used as a guide to obtain information about Cu(II) coordination. If there are two or more different chemical structures with different g and A values for the Cu(II) complex, multiple components are observed. Spectral simulations can be used to quantify the proportions of each component.

Therefore, in the context of our research CW-ESR is used primarily to predict the directly coordinated ligands as well as to quantify the Cu(II) components present in Aβ.

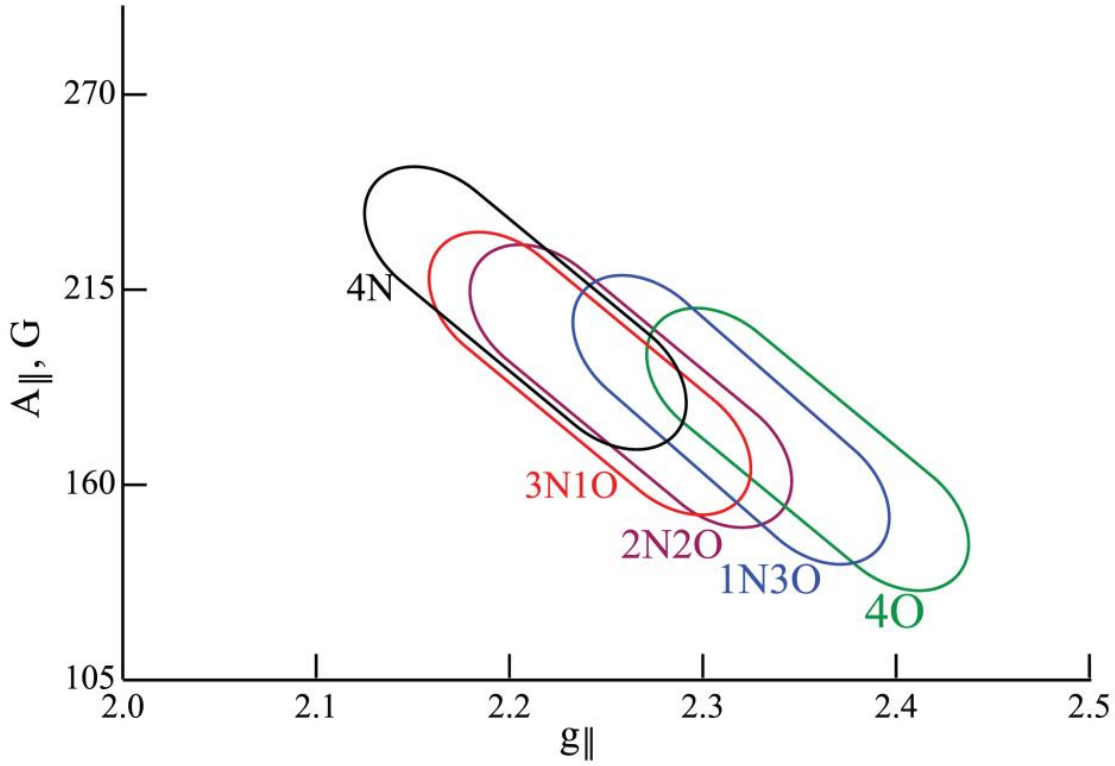

Figure 1-7 The Peisach and Blumberg plot for type II Cu(II) centers, showing the range of $A_{\parallel}$ and $g_{\parallel}$ for different equatorially coordinated atoms. The figure is recreated from Peisach et.al. *Archives of Biochemistry and Biophysics*, 1974, 165, 691–708.

Electron Spin Echo Envelope Modulation (ESEEM)

In our work, after predicting the directly coordinated ligands with the aid of CW-ESR (Figure 1-1B), we use pulsed ESR to determine the distally coupled nuclei to Cu(II). The development of pulsed ESR techniques enabled to overcome the ambiguities observed in CW-ESR ligand assignments by measuring hyperfine and quadrupole interactions given in equation 5 for nuclei such as ^{14}N and ^{1}H as shown in Figure 1-8. Information on these interactions allows us to predict a more precise coordination environment around the Cu(II) ion.

To this end we carried out ESEEM experiments at X-band (~9.5 GHz). These experiments provide information about the hyperfine and the quadrupole interactions of the nuclear spins coupled to the electron spin within ~ 8 Å.[21-23] However, at X-band with a $\pi/2$ pulse length of 16 ns (coverage of 31.25 MHz), the hyperfine interaction of the directly coordinated atoms (nitrogen imidazole shown in red in Figure 1-8) are too large to be detected.

In the three pulse ESEEM experiment used in this thesis, three $\pi/2$ pulses are used. The first two pulses are separated by a time τ, and the third pulse is applied after time T as shown Figure 1-9. The spin echo is formed at time τ after the third pulse. During the experiment τ will be fixed while T will be varied. The echo intensity is modulated with the periodicities related to the interaction between the electron spin and the coupled nuclei.

S = 1/2, I = 1/2, case: The baseline subtracted time domain signal of a three pulse ESEEM signal for a S=1/2 and I = 1/2 can be represented as follows,

$$V_{3p}(\tau,T) = 1 - \frac{k}{4}\{(1-cos\omega_\alpha\tau)[1-cos\omega_\beta(T+\tau)] + (1-cos\omega_\beta\tau)[1-cos\omega_\alpha(T+\tau)]\} \quad (8)$$

where, τ and T are the separation between pulses and ω_α and ω_β are the nuclear transition frequencies of the two spin manifolds (Figure 1-10). Fourier transformation of the time domain gives the nuclear transition frequencies as,[21]

$$\omega_\alpha = [(\omega_I - A/2)^2 + B^2/4]^{1/2} \quad (9)$$

$$\omega_\beta = [(\omega_I + A/2)^2 + B^2/4]^{1/2} \quad (10)$$

where $A = A_{zz}, B = \sqrt{A_{zx}^2 + A_{zy}^2}$. A_{zz}, A_{zx}, and A_{zy} are elements of the hyperfine tensor. ω_I is the Larmor frequency of the nucleus. For protons ^{1}H nucleus yields an ESEEM peak around ~14 MHz at a magnetic field of 3360 G.[24-25]

In equation 8, *k* , the modulation depth parameter, is given by

$$k = \left(\frac{\omega_I B}{\omega_\alpha \omega_\beta}\right)^2 \quad (11)$$

S = 1/2, I = 1, case: For I > 1/2 nucleus such as ^{14}N (*I* =1) the existence of the nuclear quadrupole interaction provides characteristic spectral lines. Figure 1-11 shows a typical ^{14}N-ESEEM spectrum of a single imidazole coordinated to a Cu(II) in the equatorial plane. There are three narrow peaks around 0.55, 1.01, and 1.54 MHz, while there is a broad peak approximately around 4 MHz.[24, 26] As shown in Figure 1-11 when the hyperfine interaction between ^{14}N and the electron spin is comparable to the nuclear Zeeman interaction they cancel each other. This condition is known as the "exact cancelation condition".[26-28] At the exact cancellation condition, only the nuclear quadrupole interactions (NQI) are observed in this electron spin manifold.[26-28] Three NQI transitions can be given as,

$$v_0 = \frac{e^2 qQ\eta}{2h};\ v_- = \frac{e^2 qQ(3-\eta)}{4h};\ v_+ = \frac{e^2 qQ(3+\eta)}{4h} \quad (12)$$

In the equations above *e* is the electron charge, *q* is the *z*-component of the electric field gradient across the nucleus, *Q* is the ^{14}N nuclear quadrupole moment, η is the asymmetry parameter, and *h* is Planck's constant.

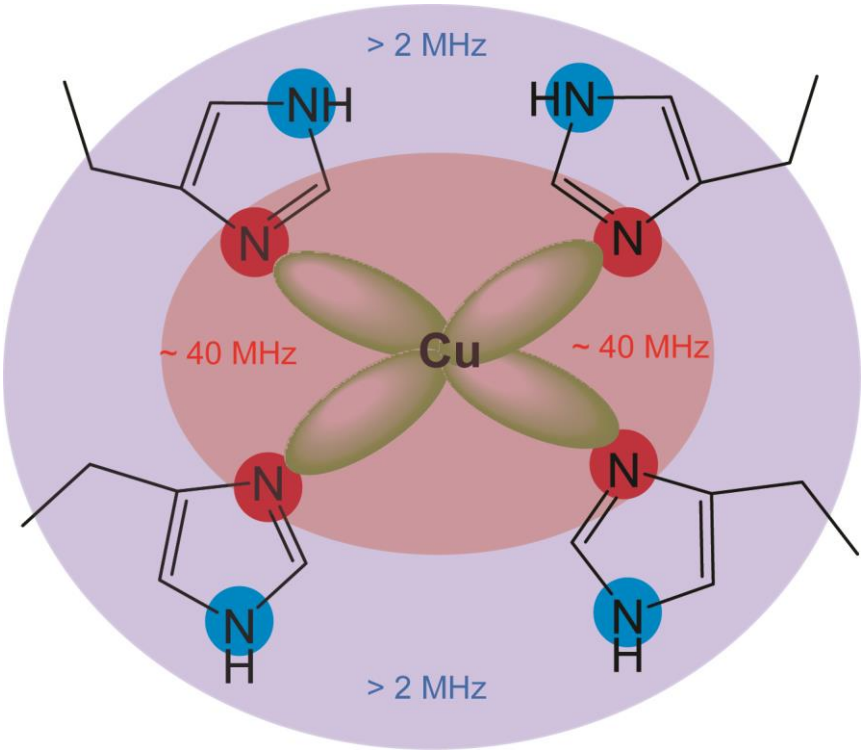

Figure 1-8 The hyperfine interactions of the imidazole nitrogen atoms coordinated to Cu(II). The directly coordinated N has a hyperfine interaction of ~40 MHz, while the remote N of the ring has a hyperfine interaction of ~ 2MHz. With a $\pi/2$ pulse of 16 ns a coverage of 31.25 MHz is obtained, which does not detect the directly coordinated Nitrogen.

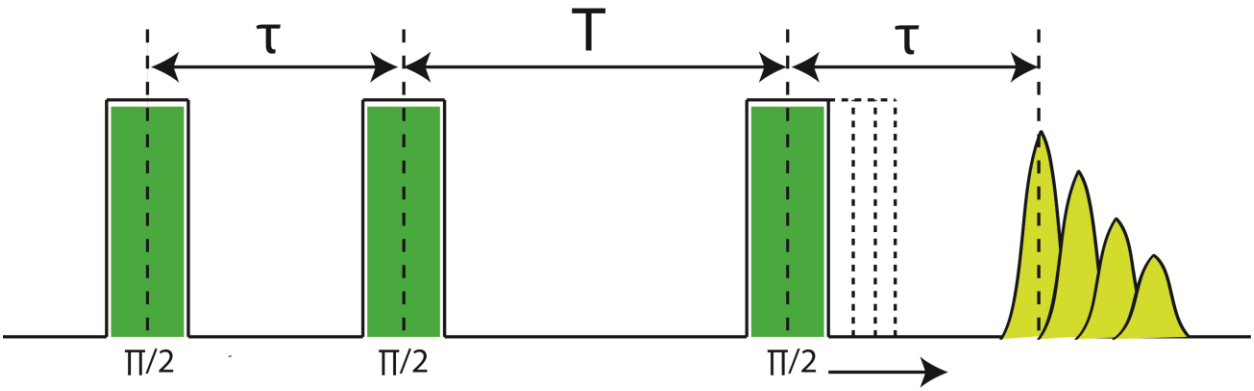

Figure 1-9 The three pulse ESEEM pulse sequence (Mims et.al. Phys. Rev. B, 1972, 5, 2409–2419 and Mims et.al. J. Chem. Phys, 1978, 69, 4921–4930). In the experiment the pulse separation between the first pulse and the second pulse (τ) is kept constant. The separation between the second and the third pulse T is increased during the experiment. The spin echo is formed after a time τ following the third pulse and is modulated with the periodicities related to the nuclei coupled to the electron spin.

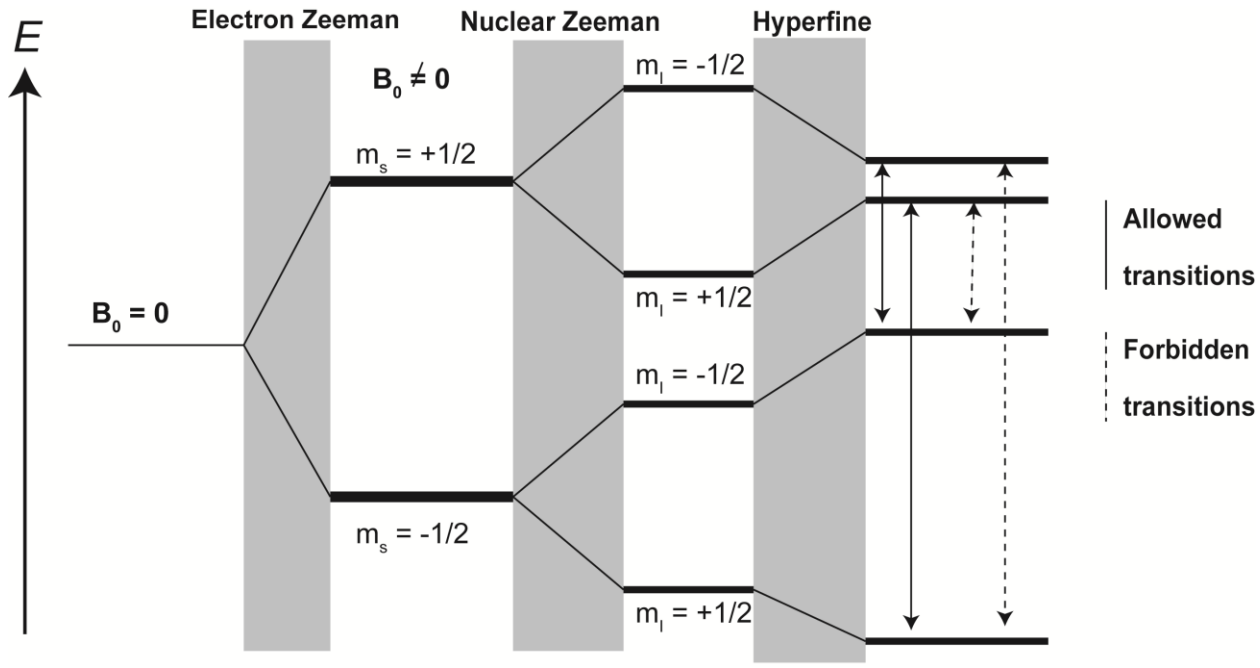

Figure 1-10 The energy level diagram of a S=1/2 and I=1/2 system. Four different ESR transitions can be considered for this system where only two fulfill ESR selection rules and are allowed transitions ($\Delta m_S = \pm 1$ and $\Delta m_I = 0$). The other two transitions are named as forbidden transitions.

The broad peak around ~4 MHz, which is attributed to a double quantum transition (DQ) [27-31]. The double quantum transition frequency is given by[32]

$$\nu_{DQ} = 2\sqrt{\left(\nu_I + \frac{A}{2}^2\right) + \left(\frac{B}{2}\right)^2 + \left(\frac{e^2qQ}{4h}\right)(3+\eta^2)} \qquad [13]$$

Where ν_{DQ} is the double quantum transition frequency, ν_I is the Larmor frequency of ^{14}N, and A and B are the secular and the pseudo secular part of the hyperfine interaction, respectively. The intensity of the DQ peak is indicative of the number of histidine residues coordinated to Cu(II).[27-28, 33]

In the case of multiple histidine coordination to Cu(II), combination peaks can appear between 2 – 3.5 MHz[34] and around ~ 8 MHz.[33, 35] On the other hand an ESEEM peak around 2.8 MHz is observed for a backbone coordination of Cu(II) via a carbonyl oxygen, which will result in an interaction between backbone ^{14}N and the electron spin.[36-37] Hence, ESEEM spectroscopy is a great diagnostic tool to explore the distal coordination environment around a Cu(II) center.

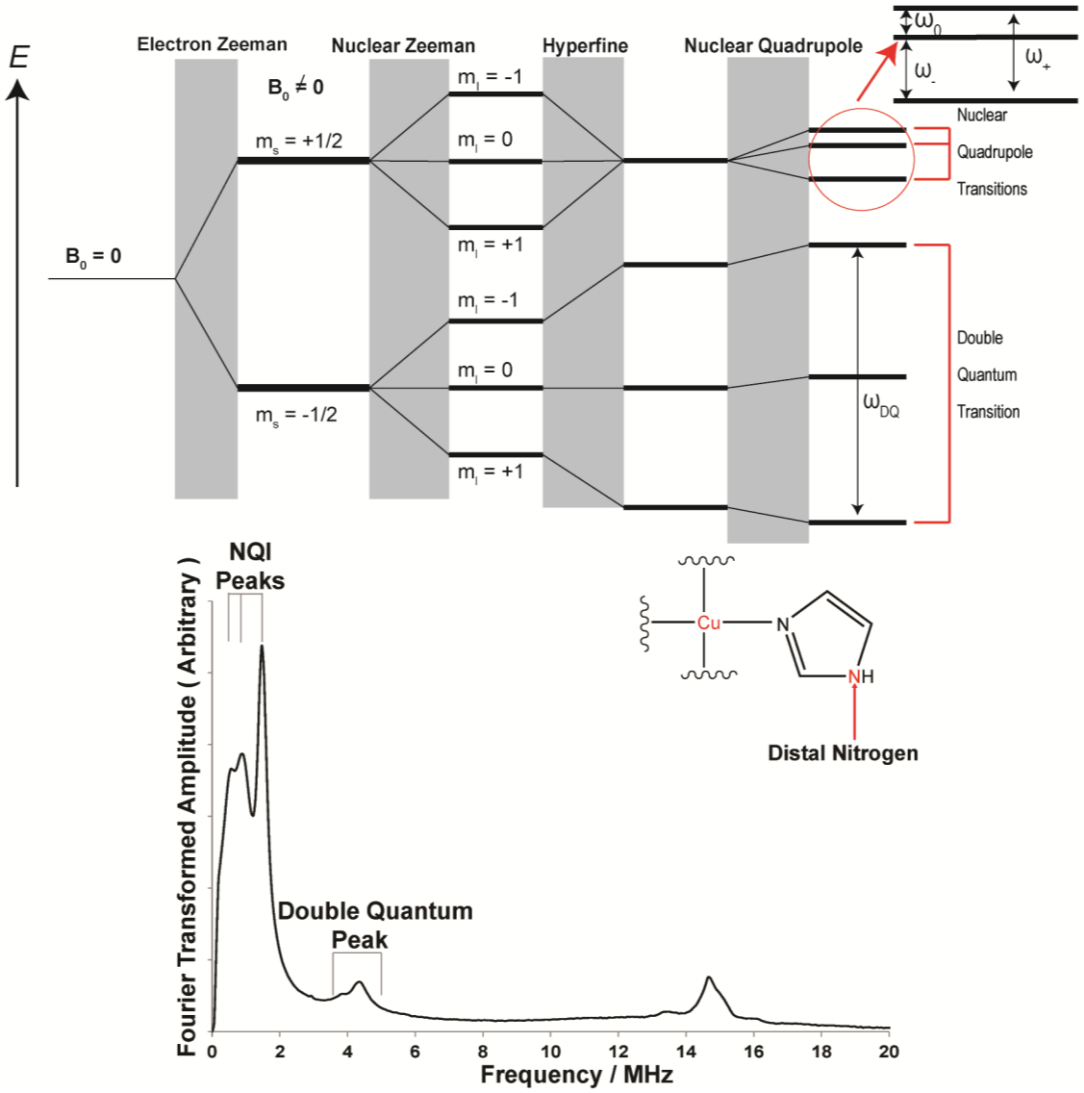

Figure 1-11 The energy level diagram for the ^{14}N nucleus. The transitions related to the nuclear quadrupolar interactions (NQI) and double quantum (DQ) transitions are shown in the energy level diagram. The ESEEM spectrum is shown in the lower panel. The peaks are due to NQI and DQ transitions in the distal ^{14}N in the imidazole ring.

Quantification of number of ^{14}N nuclei coupled to a Cu(II) center from ESEEM: In our research it is important to quantify the number of ^{14}N nuclei coupled to a Cu(II) center. Spectral simulations have been used to quantify the number of ^{14}N nuclei coupled to a Cu(II) center.[28] There are seven parameters needed to simulate the ESEEM signal for each coupled ^{14}N nuclei. These parameters are quadrupolar interaction (Q) , asymmetry parameter (η) , hyperfine constants (A and B) and three Euler angles between the quadrupolar tensor and the hyperfine tensor (cf. equations 12 and 13). If there is more than one component, these parameters as well as the proportions must be included for each component. The increase in parameter space makes accurate simulations difficult to achieve.

The modulation depth parameter [eg: k in equation 11] provides another way to quantify the number of ^{14}N nuclei that are coupled to a Cu(II) center. Figure 1-12A shows an ESEEM signal for a Cu(II) complex where n number of ^{1}H nuclei are remotely coupled to the electron spin. The modulation depth parameter (k in equation 11) can be determined by measuring the ratio of $a/(a+b)$, where a is the depth of the first modulation and b is the difference in normalized echo intensity (y-axis) from the bottom of the first modulation to the zero of the y-axis. These are shown in Figure 1-12A.

For a ^{14}N nucleus there are multiple modulations, such as the three NQI frequencies (equation 12) and the DQ frequency (equation 13) overlaid in the time domain curve as shown by Figure 1-12B. Hence, it is difficult to obtain modulation depth information for a specific frequency. Shin et. al. showed that the integrated intensities of the ^{14}N ESEEM region can be used to account for the changes observed in modulation depths.[38] As the peak intensities are arbitrary in ESEEM spectra, ^{1}H ESEEM integrated intensity is used as an internal standard to normalize spectra. Here it was assumed that the number of ^{1}H nuclei coupled to a Cu(II) center is the same for an open

coordination site, as the ^{1}H ESEEM signal that arises from the solvent water molecules interacting with the metal center.

In Aβ, where more than one histidine residues can coordinate to Cu(II), the ^{14}N ESEEM signal results from all the histidine residues coordinated. Isotopic enrichment of a magnetic nucleus with another magnetic isotope of the same element enables us to assign applicable modulations observed in an ESEEM signal. To this end we substitute ^{14}N nuclei in histidine with a ^{15}N isotope. The spin of ^{15}N nuclei is I = 1/2 and does not have a quadrupole moment. Hence, the ESEEM of ^{15}N nucleus is determined by hyperfine and nuclear Zeeman interaction. When ^{14}N nuclei in histidine are replaced with isotopic ^{15}N, if the histidine is involved in Cu(II) coordination the modulation depth of the ESEEM will decrease (k_{14N}~ 0.3 vs k_{15N}~0.006) .[31, 39] As the contribution from ^{15}N nuclei is ~2% towards the ESEEM signal, ^{15}N isotopic substitution provides a direct method of quantifying the number of histidine residues coordinated to a Cu(II).

In this thesis we use ESEEM integrated intensities in conjunction with systematic ^{15}N labeling to obtain precise information about different coordination modes of Cu(II) in Aβ.

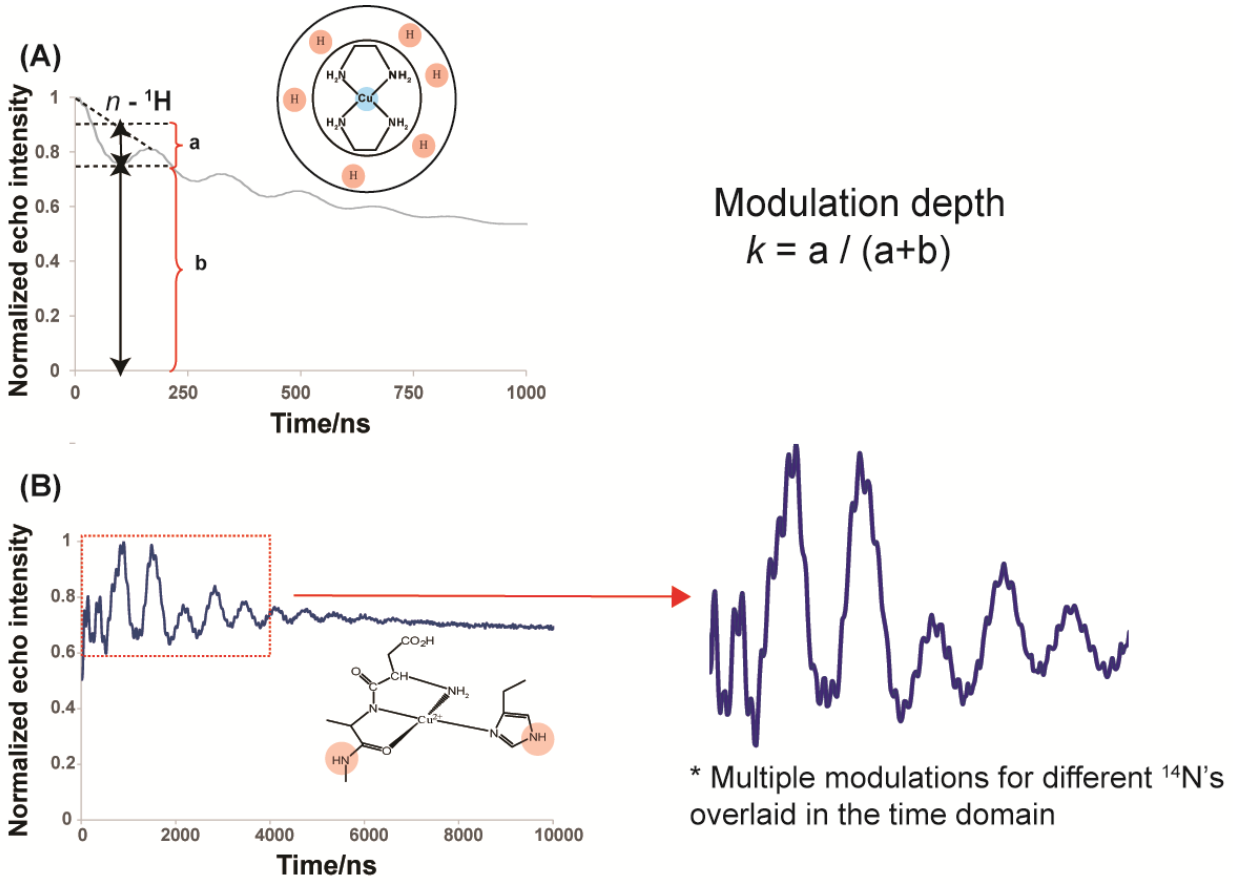

Figure 1-12 (A) Experimental ESEEM spectrum for *n* number of ^{1}H nuclei coupled to a Cu(II) spin. The data presented in the panel A is acquired for the Cu(II) complex shown in the inset. The modulation depth is defined in the time domain signal (B) The ESEEM spectrum of a Cu(II)-Aβ(1-16) complex at pH 8.7 is shown. Here a histidine imidazole is coordinated to the Cu(II) leading to several different modulations in the ESEEM signal.

Hyperfine Sublevel Correlation (HYSCORE)

In one dimensional (1D) ESEEM, certain ESEEM peaks overlap, making it difficult to unambiguously identify the coordination environment.[25, 40] Höfer et.al., introduced the hyperfine sublevel correlation,[40] a 2D experiment with a four pulse sequence, (Figure 1-13) which simplifies the detection and the analysis of multiple nuclear-nuclear interactions. Furthermore, the addition of the second dimension improves the spectral resolution. 1D ESEEM experiments further suffer from a blind spot effect. For example, this effect is observed for ^{1}H ESEEM because at certain τ (Figure 1-9), the value of $(1 - cos\omega_{\alpha}\tau)$ or $\left(1 - cos\omega_{\beta}\tau\right)$ in equation 8 is zero. Hence, to avoid the blind spot effect the ESEEM experiment needs to be done at several τ values. The use of 2D HYSCORE allow us to overcome the blind spot effect without performing multiple experiments.

Compared to the 1D ESEEM pulse sequence (Figure 1-9), there is an additional π pulse inserted between the 2nd and 3rd $\pi/2$ pulses as shown in Figure 1-13A. The interval between the 2nd and 3rd pulses, t_1, and the interval between the 3rd and the 4th pulses, t_2, are incremented independently. The π pulse allows the transfer of the nuclear coherence between the two electron spin manifolds (m_s= +1/2 and m_s= -1/2) shown in Figure 1-10. The echo intensity is recorded as a function of time t_1 and t_2, as shown in Figure 1-13A. Hence if the nuclear coherence evolves at a frequency of ν_A during time t_1, and with a frequency ν_B during time t_2 then a cross peak at (ν_A, ν_B) is observed in the HYSCORE spectrum.

The HYSCORE spectrum shown in Figure 1-13C is acquired for a Cu(II) coordinated with Prion protein derived peptide PHGGGW. Millhauser and co-workers (Figure 1-13C) resolved the structure of the Cu(II)-PHGGGW fragment with the aid of ESEEM, HYSCORE and X-ray crystallography.[36, 41-42] We show the HYSCORE data of this structure because its spectrum clearly illustrates how peaks from backbone coordination (Figure 1-13B purple circle) are separated from

peaks for histidine coordination (Figure 1-13B red circle). Along the diagonal of the HYSCORE spectrum shown in Figure 1-13C the peaks corresponding to ESEEM signals are observed. In addition cross peaks corresponding to correlation between the NQI and the DQ frequencies for histidine coordination (red dashed circles) and backbone coordination (purple dashed circles) are observed as shown in Figure 1-13C.[36-37, 41, 43] The existence of these cross peaks provide further information about the frequencies observed in the ESEEM experiment.

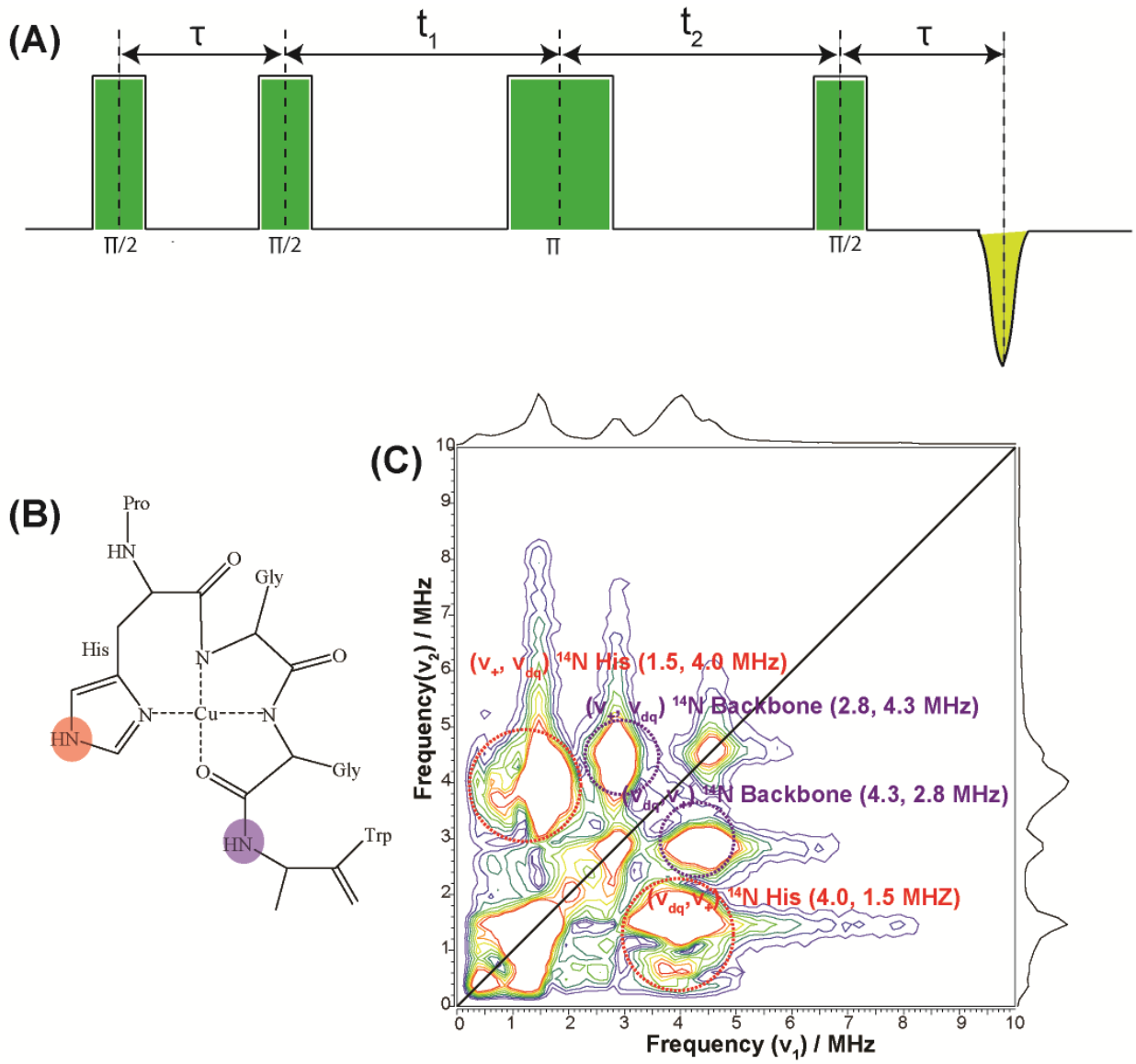

Figure 1-13 (A) The HYSCORE pulse sequence (Höfer et. al. *Chem. Phys. Lett.* 1986, *132*, 279–282). (B) Prion protein based PHGGGW fragment coordinated to Cu(II). (C) Experimentally obtained HYSCORE spectrum for Cu(II)-PHGGGW complex at 80 K. Dashed circles in red correspond to cross peaks due to correlation of the NQI and the DQ transitions of a histidine imidazole (red circle in the structure). Dashed circles in purple correspond to cross peaks due to correlation of the NQI and the DQ transitions of a backbone coordination (purple circle in the structure).

1.2 DISTANCE MEASUREMENTS USING DEER SPECTROSCOPY

In the chapters 4 and 5 we use site directed spin labeling and DEER spectroscopy, which enable us to understand the origins of the structural flexibility in supramolecular polymers as shown in Figure 1-1B.

Several ESR methods have been used to extract distance between two paramagnetic centers.[44-45] These methods include continuous wave (CW),[46-49] double electron electron resonance (DEER),[50-52] and double quantum coherence (DQC) experiments.[53-54] Additionally relaxation based methods are used to estimate distances between spin pairs.[55-56] ESR based methods are advantageous for systems that cannot be investigated by techniques such as X-ray crystallography and NMR. For the remainder of this section, we will focus on DEER spectroscopy as this method has been used to probe the systems discussed in this dissertation.

Site directed spin labeling

Hubbell and coworkers developed the site directed spin labeling (SDSL) methodology to introduce an unpaired electron to selected positions in a protein.[57-58] This introduction is achieved by cysteine mutagenesis and covalent modification of the sulfydryl group with a selective nitroxide group. The most common nitroxide label used is 1-oxyl-2,2,5,5-tetramethylpyrroline-3-methyl)methanethiosulfonate (MTSSL) and the reaction involved is shown in Figure 1-14A. The ESR spectrum of MTSSL spin label probes information on side chain dynamics and protein backbone dynamics.[59-60] For peptides the α-amino acid 2,2,6,6-tetramethyl-N-oxyl-4-amino-4-carboxylic acid (TOAC) can also be used to introduce a nitroxide group via peptide synthesis.[59, 61] In this scheme the spin label is placed in the peptide backbone and exclusively probes backbone dynamics.[59] The only degree of freedom associated with TOAC is the conformation of the six membered ring.[59] (Figure 1-14B).

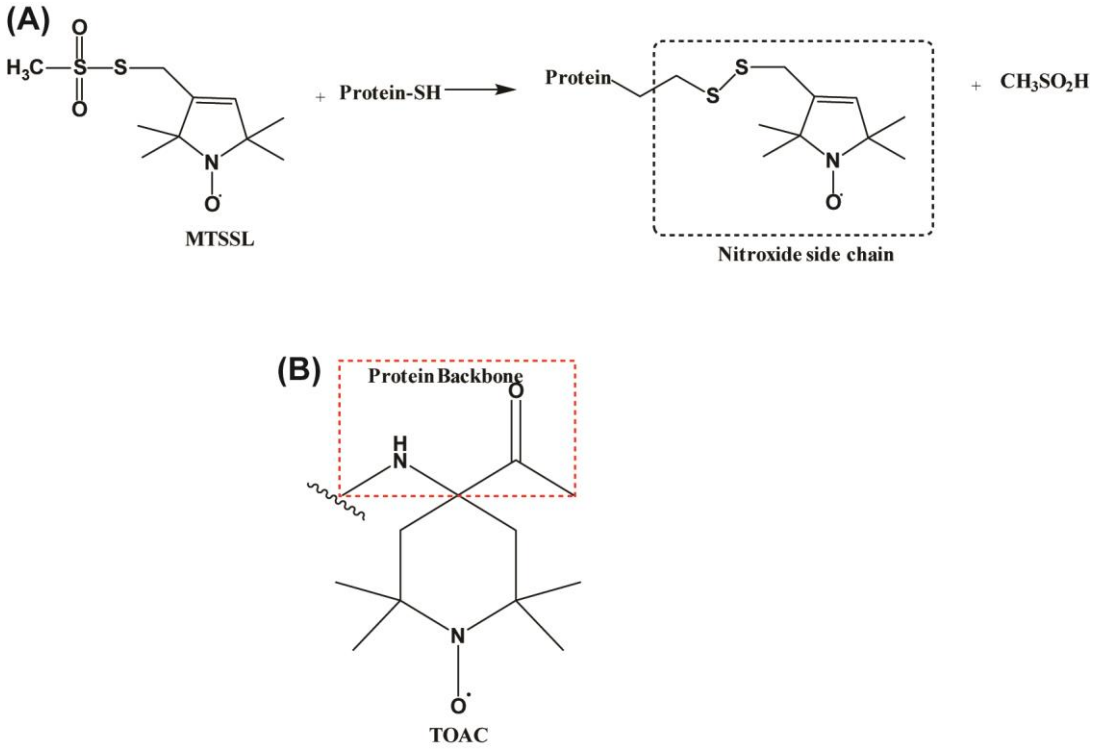

Figure 1-14 (A) Site directed spin labeling reaction (B) Chemical structure of the TOAC label.

DEER spectroscopy

DEER spectroscopy is the most common ESR technique used to measure distances between two paramagnetic centers. In the DEER experiment the electron dipolar interaction between two spins is detected as a modulation in a spin echo at low temperatures. The Hamiltonian for the dipolar interaction can be simplified as follows,

$$\hat{\mathcal{H}}_{dipolar} = \frac{\mu_0}{4\pi\hbar} g_A g_B \beta_e^2 \left[\frac{(\hat{S}_A . \hat{S}_B)}{r_{AB}^3} - \frac{3(\hat{S}_A . \vec{r}_{AB})(\hat{S}_B . \vec{r}_{AB})}{r_{AB}^5} \right] \quad (14)$$

Where, μ_0 is the permeability of the vacuum, β_e is the Bohr magneton, $\hbar$ is the reduced Planck constant, g_A and g_B are the g-factors of the spins A and B, respectively. $\hat{S}_A$ and $\hat{S}_B$ are the electron spin angular momentum operators for A and B spins and $\vec{r}_{AB}$ is the interspin vector connecting the spins (Figure 1-15A).

The dipolar interaction can be written as,

$$\hat{\mathcal{H}}_{dipolar} = \frac{\mu_0}{4\pi\hbar r_{AB}^3} g_A g_B \beta_e^2 (\hat{a} + \hat{b} + \hat{c} + \hat{d} + \hat{e} + \hat{f}) \quad (15)$$

Where,

$$\hat{a} = \hat{S}_{A,z}\hat{S}_{B,z}(3cos^2\theta - 1)$$

$$\hat{b} = -\frac{1}{4}(\hat{S}_{A+}\hat{S}_{B-} + \hat{S}_{A-}\hat{S}_{B+})(3cos^2\theta - 1)$$

$$\hat{c} = -\frac{3}{2}\sin\theta\cos\theta e^{-i\varphi}(\hat{S}_{A,z}\hat{S}_{B+} + \hat{S}_{A+}\hat{S}_{B,z})$$

$$\hat{d} = -\frac{3}{2}\sin\theta\cos\theta e^{i\varphi}(\hat{S}_{A,z}\hat{S}_{B-} + \hat{S}_{A-}\hat{S}_{B,z})$$

$$\hat{e} = -\frac{3}{4}\sin^2\theta\, e^{-2i\varphi}\hat{S}_{A+}\hat{S}_{B+}$$

$$\hat{f} = -\frac{3}{4}\sin^2\theta\, e^{2i\varphi}\hat{S}_{A-}\hat{S}_{B-}$$

θ is the orientation of the interspin vector (Figure 1-15A) with respect to the external magnetic field and φ is the angle between the projection of the interspin vector on the x-y plane and the x-axis. Term "a" from equation 15 is the most dominant dipolar term in the DEER experiment and the dipolar Hamiltonain for the DEER experiment can be written as,

$$\hat{\mathcal{H}}_{dipolar} = \frac{\mu_0}{4\pi\hbar r_{AB}^3} g_A g_B \beta_e^2 \hat{S}_{A,z}\hat{S}_{B,z}(3cos^2\theta - 1) = \omega_{AB}\hat{S}_{A,z}\hat{S}_{B,z} \qquad (16)$$

Where, ω_{AB} is defined as,

$$\omega_{AB} = \frac{\mu_0 g_A g_B \beta_e^2}{4\pi\hbar r_{AB}^3}(3cos^2\theta - 1) \qquad (17)$$

At low temperatures, due to anisotropy of *g* and *A* tensors, all θ angles are typically excited at X-band. In the DEER experiment, the pulses are applied at two different frequencies to measure the dipolar interaction between the two electron spins. In Figure 1-15A, a nitroxide field sweep echo detected spectra acquired at X-band is shown. Here, the positions of the observer frequency, which excites the A spins, and the pump frequency which excites the B spins are shown. The pump frequency is applied ~ 70 MHz away from the observer frequency position.

The pulse sequence of the four pulse DEER experiment is shown in Figure 1-15B. The pulse sequence has a fixed inter-pulse delay at the observer frequency (A spins) which forms a primary refocused echo. Then an inversion pulse is applied at the pump frequency (B spins) at variable time *t* with respect to the refocused echo. The pump pulse flips the B spins by 180^0 and this inverts the dipolar interaction between the A and B spins. This inversion changes the Larmor frequency of the A spins by ω_{AB} and changes the echo signal intensity.

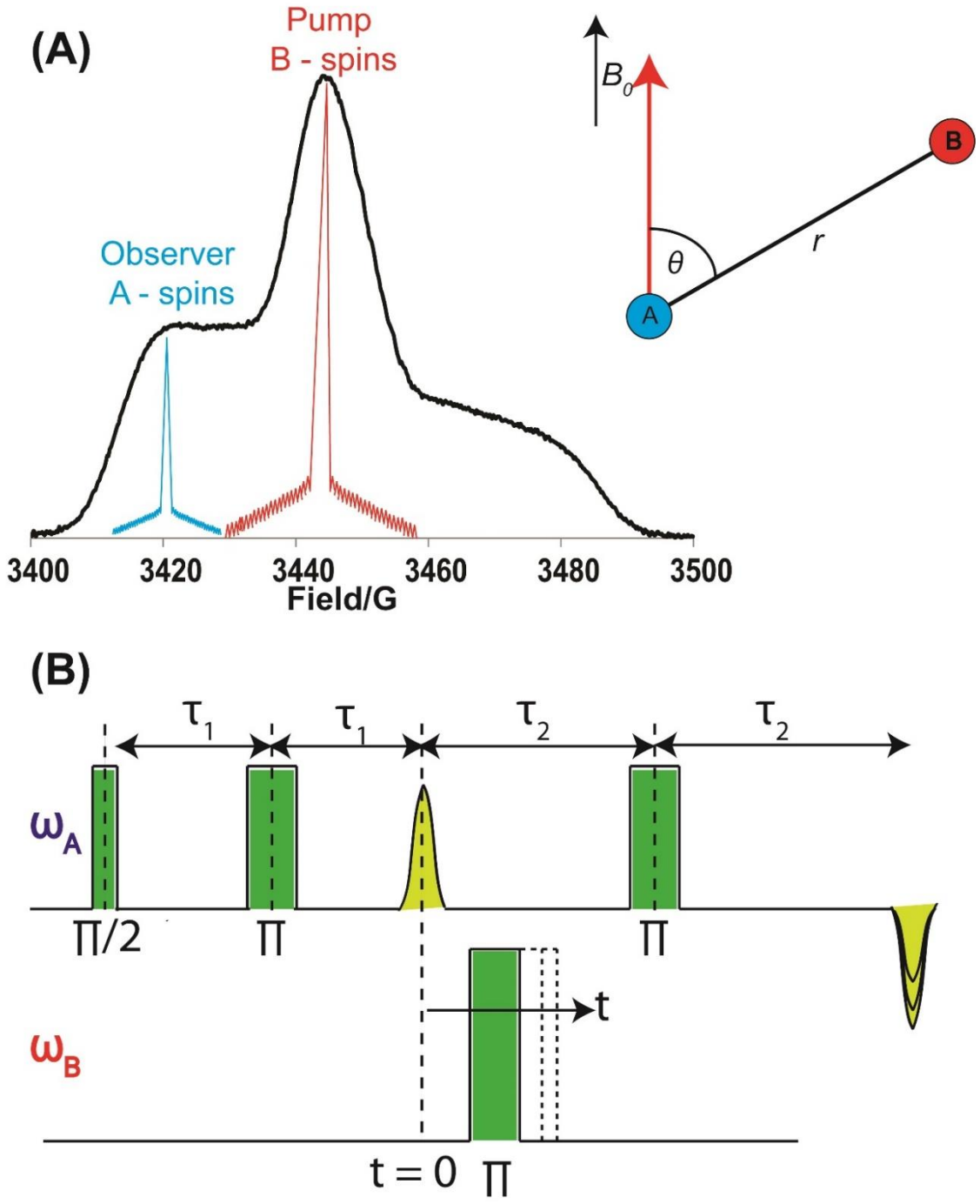

Figure 1-15 (A) The echo detected spectrum of a nitroxide spectrum showing the positions of the observer and the pump frequencies. The inset illustrates the distance vector *r* between spin A and spin B at an angle of θ with the magnetic field vector B_0. (B) Pulse sequence for the four pulse DEER experiment (Pannier et. al. *J. Magn. Reson.* 2000, *142*, 331–340).

Ideally, the DEER experiment should measure the distance between the two electron spins within a molecule, i.e. the intramolecular distance. In frozen samples two types of distances contribute to the DEER signal. Intramolecular distance (solid lines in Figure 1-16A) leads to an oscillating echo decay, where the period is related to the distance. However, the spins on other molecules in the neighborhood contribute to the signal, creating an intermolecular distance (dashed lines in Figure 1-16A). Thus, the time domain signal for the DEER experiment is a product of the intra and intermolecular interactions (Figure 1-15B)

$$S(t) = V_{intra}(t)V_{inter}(t) \quad (18)$$

Because, the intermolecular interaction consists of a large range of distances and orientations, the $V_{inter}(t)$ signal is just an exponential decay. $V_{inter}(t)$ signal depends on spin concentration (C) and the fraction of the B spins (λ_B) excited by the pump pulse as given by equation 19.[62]

$$V_{inter}(t) = \exp(-kC\lambda_B t) \qquad (19)$$

$$k = \frac{8\pi^2}{9\sqrt{3}}\frac{g_A g_B \beta_e^2}{\hbar}$$

The intermolecular interaction dominates at longer *t* values, and to obtain the $V_{intra}(t)$ signal, the raw DEER data is background subtracted. This procedure is shown in Figure 1-16B. The $V_{intra}(t)$ is given as,

$$V_{intra}(t) = 1 - \iint p(r)\,(\lambda_B - \lambda_B cos[\omega_{AB}t])\xi(\theta)d(\theta)dr \qquad (20)$$

where, $p(r)$ is the distance distribution, λ_B is the fraction of B spins excited by the pump pulse, hence the fraction of spins that perturb the A spins, and $\xi(\theta)$ is the geometrical form factor.

To extract the distance distribution from the time domain data, model independent fits based on Tikhonov regularization or model dependent fits such as a Gaussian distribution can be used.[63]

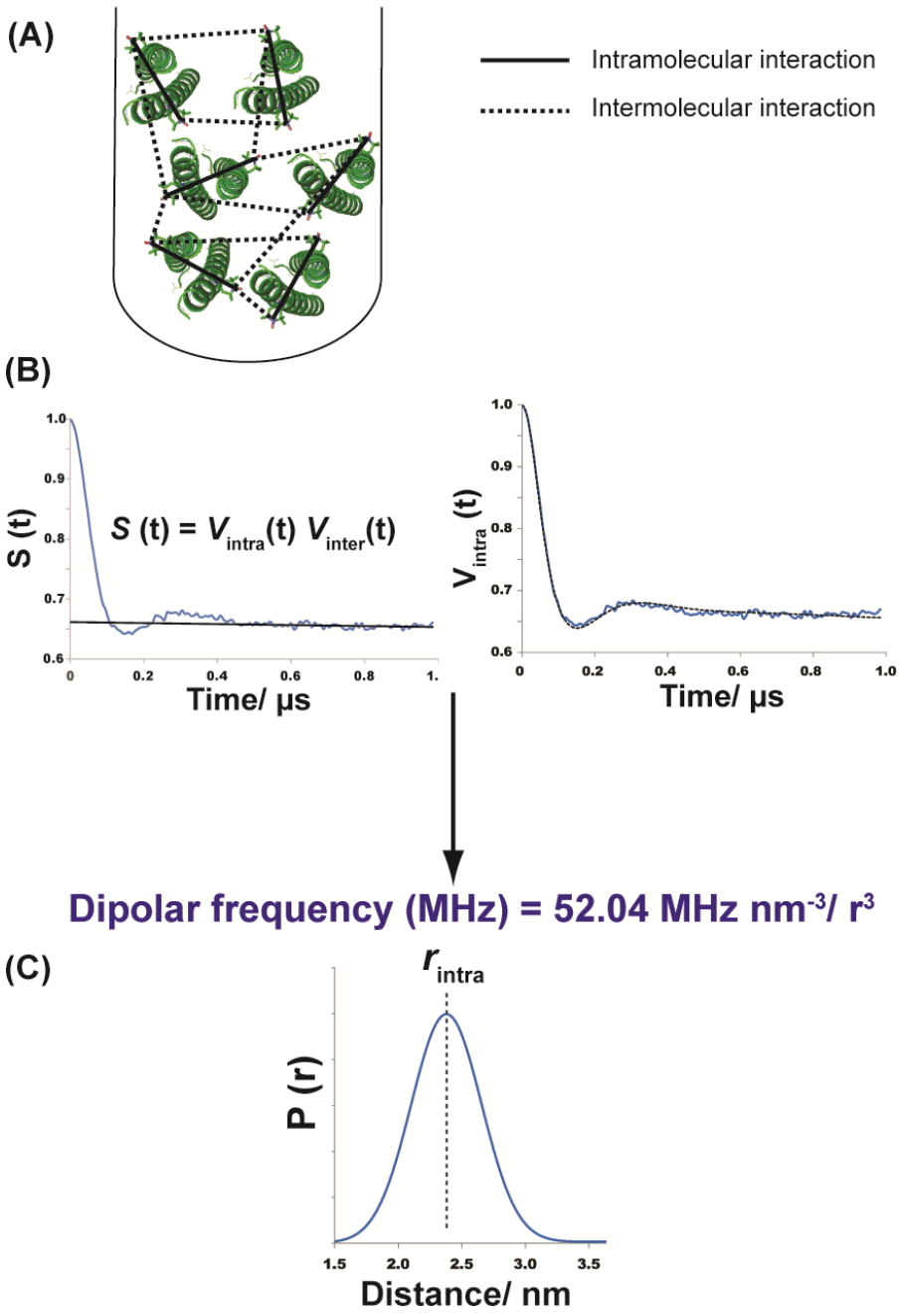

Figure 1-16 (A) Illustration of the intramolecular and the intermolecular interactions (B) The procedure used to subtract the background subtracted DEER data to obtain V_{intra} is shown. (C) The distance distribution obtained for the GCN4 peptide.

2.0 ESEEM ANALYSIS OF MULTI-HISTIDINE Cu(II) COORDINATION IN MODEL COMPLEXES, PEPTIDES, AND AMYLOID BETA

Part of this work is written in collaboration with Brian C. Michael, Steven J. Geib, and Sunil Saxena and has been published in Journal of Physical Chemistry B, 2014, V. 118, 8935-8944

2.1 INTRODUCTION

Among natural amino acids histidine is one of the strongest metal ion coordinators.[9] Hence, histidine plays an important role in metal ion coordination in proteins and peptides. Histidine is a tridentate ligand, which provides ligands at the imidazole imido nitrogen, the amino nitrogen, and the carboxylate oxygen.[15] The imidazole ring nitrogen of histidine residues often provides the primary coordination site for metal ions.[15] Copper is an essential metal ion for biological functions and is found in bound forms in metalloproteins and in low molecular weight complexes to avoid toxicity associated with free copper.[15] Copper-containing proteins often have binding sites with irregular geometries containing one or more histidine ligands.

Copper coordination in amyloidogenic proteins such as amyloid-β (Aβ), prion, and α-synuclein is achieved through histidine residues.[17] All these systems contain highly heterogeneous copper coordination environments. Small changes in the coordination may have an effect on aggregation and other chemical mechanisms in the diseased state.[5] Hence, it is critical to elucidate the structural details of the different coordination modes to completely understand the biological role played by metal−protein complexes.[9]

In α-synuclein two Cu(II) coordination sites at the N-terminal region were identified using mass spectrometry (MS)[64] and nuclear magnetic resonance (NMR).[65] Later circular dichroism (CD)[65] and electron spin resonance (ESR) results indicated that these sites are independent of each other.[66-68] The high affinity site is anchored by the N-terminus, and the second site is anchored by the histidine at position 50.[69] Other than these two sites, recent NMR and ESR results propose a low affinity Cu(II) binding site at the C-terminal region.[66, 70] In prion protein the presence of four binding sites at higher Cu(II) occupancy in each of the PHGGGWGQ octarepeat regions were identified based on ESR,[36, 42-43, 71-73] CD,[43, 71-72] NMR,[74-75] and X-ray absorption spectroscopy (XAS)[76-77] results. Two additional Cu(II) equivalents coordinate via the histidine residues located at positions 96 and 111.[17, 36, 73, 76] Additionally, the Cu(II) coordination environment in prion octarepeat domain has been extensively studied by ab initio methods.[78-80]

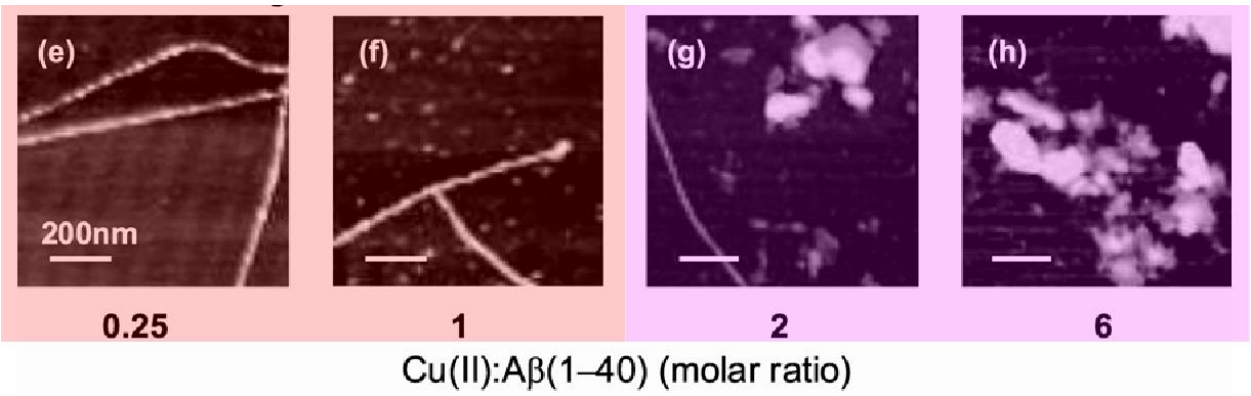

Figure 2-1 The morphology of the amyloid aggregates is affected by the Cu(II):peptide ratio in vitro. At sub equimolar and equimolar Cu(II) ratios the fibrils are more dominant, while at greater than equimolar Cu(II) ratios amorphous aggregates become more dominant. The image was adapted from Jun et.al. *Biochemistry*, **2009**, 48 10724-10732.

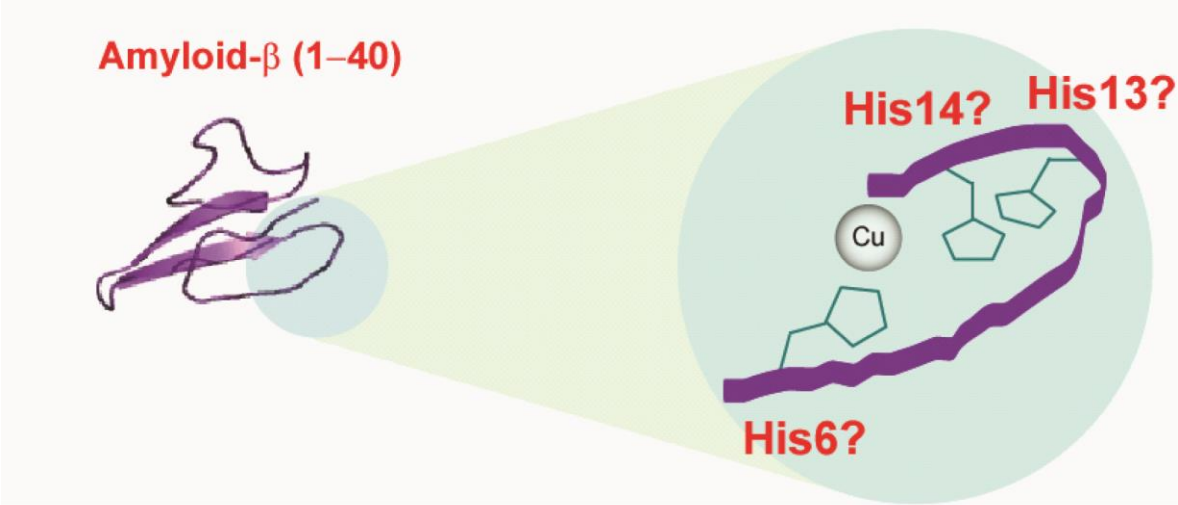

Aβ (1-40) DAEFRHDSGYEVHHQKLVFFAEDVGSNKGAIIGLMVGGVVIA
Aβ (1-16) DAEFRHDSGYEVHHQK

Figure 2-2 Metal binding domain of the Aβ (1-40) peptide is located in the N-terminus region in the peptide. The metal binding site contains three histidine residues at positions 6, 13, and 14 which act as the anchoring residues. Aβ (1-16) is used as a model complex to understand the coordination of metal ions to Aβ.

The copper coordination to Aβ is highly heterogeneous, with the specific coordination environment depending on the pH, ionic strength, concentration of the metal ions, and the presence of other metal ions. Jun et.al showed that the morphology of Aβ aggregates depends on the Cu(II) ratio in vitro as shown in Figure 2-1.[3-4] The metal binding domain of Aβ contains three histidine residues at positions 6, 13, and 14as shown in Figure 2-2.[5, 81] The Cu(II) ion coordination in Aβ(1−16) has been shown to be identical to that in the full length Aβ.[5-7] Hence, Aβ(1−16) is used as a model system understand the metal ion interaction with Aβ. The presence of all three histidine residues in Cu(II) coordination spheres was initially proposed by NMR[81-82] and was later confirmed by ESR.[83] Other techniques such as XAS,[84-85] Fourier transform infrared spectroscopy (FTIR),[5] CD,[81, 86-87] ultraviolet−visible (UV−vis),[87] MS,[88] and ab initio calculations[84, 89-90] also proposed the involvement of histidine residues in Cu(II) coordination.

A number of ESR studies have suggested an equilibrium between two different Cu(II) coordination modes in an equimolar Aβ−Cu(II) complex at pH 7.4, known as component I and component II.[34, 38, 81, 91-93] The component I is predominant at lower pH values (∼pH 6.0).[5] Component II is dominant at higher pH (∼pH 8.7).[5]

These two components are believed to have a different number of histidine residues coordinated to the Cu(II) ion.[6] Component I is believed to have two histidine residues that simultaneously coordinate to Cu(II).[6, 38] Previously Shin and Saxena used electron spin echo envelope modulation (ESEEM) in conjunction with ^{15}N isotopic labeling, to determine that the Aβ component I consists of three subcomponents, at physiological pH where two of the three histidines are simultaneously coordinated to Cu(II) ion, as shown in Figure 2-3.[38] Interestingly, only two of these subcomponents, are present at lower pH values.[6, 34] Cu(II) coordinated to His 6−His 13 and His 6−His 14 are found in equal proportions, while the His 13−His 14 coordination

is absent at lower pH.[34, 38] These measurements were able to uncover the critical role of His 13−His 14 in Cu(II) coordination at physiological pH and provide a possible rationale for the presence of amorphous aggregates, rather than fibrils at high Cu(II) concentrations.[4, 38]

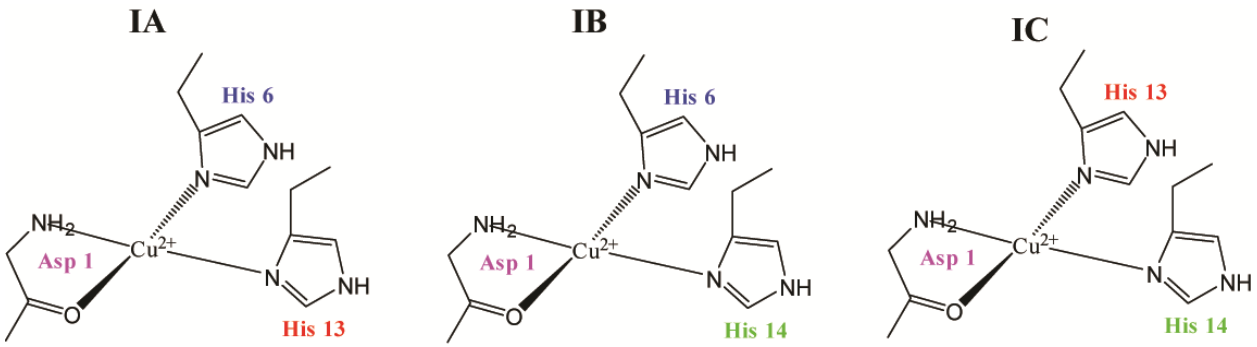

Figure 2-3 Three proposed subcomponents for component I in Aβ-Cu(II) complex.

The number of histidine residues coordinated to Cu(II) in component II is controversial. One hypothesis proposes that Cu(II) is coordinated to the CO group of the Ala 2−Glu 3 bond and three histidine residues as shown in Figure 2-4.[91] The second proposition involves the N-terminus, one N atom from one of the three histidine imidazoles, the backbone N from Asp 1-Ala 2 peptide bond, and the CO group of the Ala 2−Glu 3 peptide bond (Figure 2-4).[34] The elucidation of the coordination in component II is critical as a recent research shows that, in the presence of Zn(II), Cu(II) coordination moves to a component II-like coordination.[92, 94] Furthermore, it has been shown that Zn(II) can only displace Cu(II) from component I coordination as discussed in chapter 3.[92] One equivalent of Zn(II) ions displaces ~25% of the bound Cu(II) from Aβ(1−16) at physiological pH, while rearranging the rest of the bound Cu(II) in component I.[92] In the presence of one equivalent of Zn(II) ions, components I and II account equally for Cu(II) coordination in Aβ.[92] However, at excess amounts of Zn(II), component II becomes the dominant Cu(II) coordination mode.[92] In brain tissues affected by the Alzheimer's disease, the concentration of Zn(II) is approximately three times higher than Cu(II).[1] Therefore, component II Cu(II) coordination may be the most dominant coordination mode in vivo. Shedding light into the coordination of component II is critical to understand the behavior of Cu(II) in AD etiology.

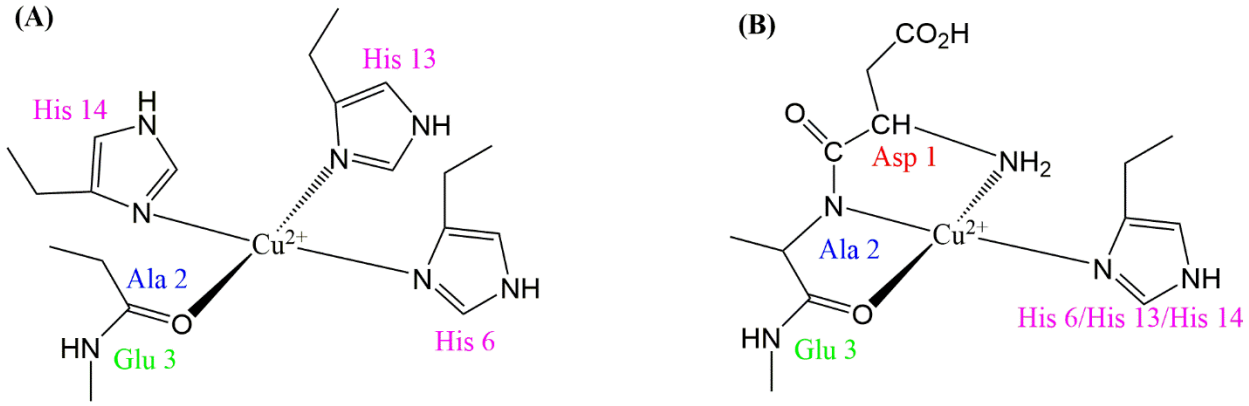

Figure 2-4 Two proposed structures for the component II Cu(II) coordination (A) Three histidine coordination proposed by Drew et. al. *J. Am. Chem. Soc.* **2009**, 131, 1195−1207 (B) One histidine coordination proposed by Dorlet et. al. *Angew. Chem., Int. Ed.* **2009**, 48, 9273−9276.

Herein, we propose a method to quantify the number of ^{14}N nuclei coordinated to a Cu(II) center by the use of integrated intensities of the Fourier-transformed ESEEM. ESEEM spectroscopy is a pulsed ESR technique that has been used to identify and quantify the number of histidine imidazoles coupled to a Cu(II) center. Spectral simulations of the ESEEM spectra are often used to determine the number of coupled ^{14}N nuclei.[28, 95] However, as shown by Figure 2-5, different number of ^{14}N nuclei coupled to the Cu(II) yield similar fits. Also, when the number of ^{14}N nuclei increased, the number of ESR parameters required is increased, making simulations less reliable. Furthermore, the heterogeneous coordination environment of metal ions, makes it hard to disentangle different subcomponents, since additional parameters for the proportions of each subcomponent have to be included in the simulation.

Alternatively, Shin et al. compared the normalized integrated intensities of the frequency domain ESEEM spectra to calculate the intensity reduction resulting from the replacement of a ^{14}N with ^{15}N in Aβ(1−16)−Cu(II) complexes.[38] Although, the use of integration method was useful in elucidating important structural information, the validity of the method was not tested experimentally. Here we obtained ESEEM data from simple model complexes with different numbers of imidazoles coordinated to Cu(II). The normalized integrated intensities of the model complexes increased monotonically, when the number of imidazole rings increased in model complexes. Two small peptides with known Cu(II) coordination was used to test the validity of the method. The DAHK−Cu(II) complex contains a single ^{14}N ESEEM active nucleus, while PHGGGW−Cu(II) complex contains two nonidentical ^{14}N ESEEM active nuclei. Finally, our method was used to distinguish between the two proposed modes of Cu(II) coordination. Then, in conjunction with ^{15}N isotopic labeling we quantified the subcomponent proportions in component II.

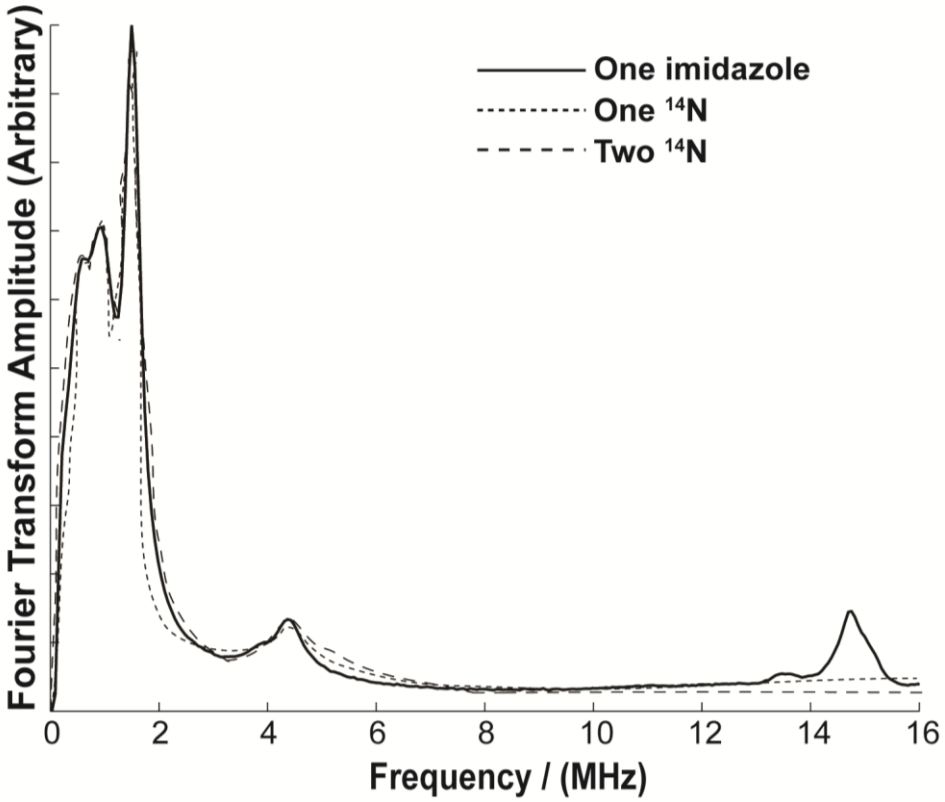

Figure 2-5 Experimental ESEEM spectrum of the one imidazole complex overlaid with simulations performed using one and two ^{14}N nucleus.

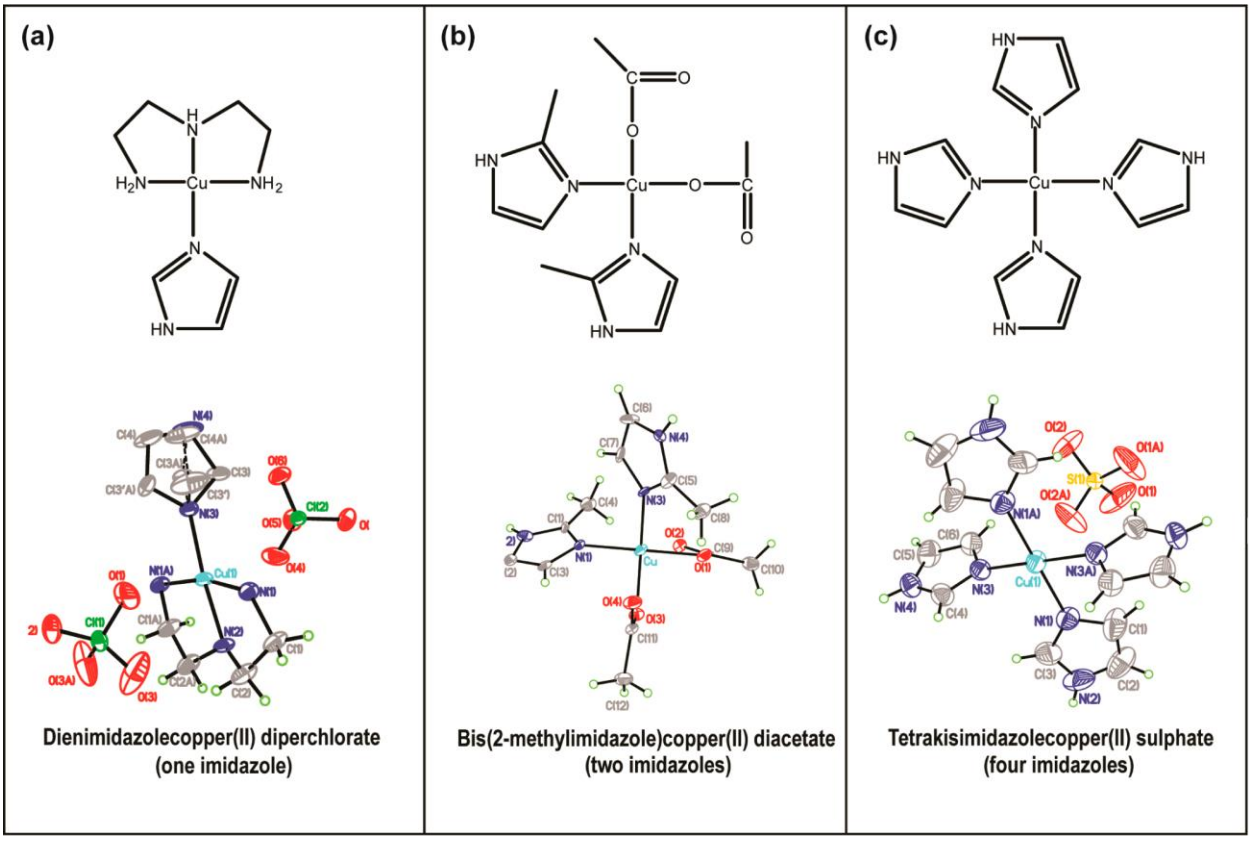

Figure 2-6 Structures of the model complexes with 1, 2, and 4 imidazole rings with respective crystal structures.

2.2 EXPERIMENTAL SECTION

Synthesis of Copper−Imidazole Complexes

For the preparation of tetrakisimidazolecopper(II) sulfate (see Figure 2-6a), 40 mL of a 1 M imidazole (99% Sigma-Aldrich Co., St. Louis, MO) solution was added to 10 mL of 1 M $CuSO_4 \cdot 5H_2O$ (98+% Sigma-Aldrich Co., St. Louis, MO) solution and left at room temperature to evaporate. After a few days, dark blue colored crystals formed.[96] For the preparation of bis(2-methylimidazole)copper(II) diacetate[97] (see Figure 2-6b), 0.5 g of Cu(II) acetate hydrate (98% Sigma-Aldrich Co., St. Louis, MO) and 1.0 g of 2 methylimidazole (99% Sigma-Aldrich Co., St. Louis, MO) were added and dissolved in a mixture of chloroform (10 mL) and methanol (2.5 mL). This mixture was stirred for 30 min at 50 °C and filtered. Then, 15 mL of diethyl ether was added to the filtrate and stirred for 10 min. Then another 5 mL of diethyl ether was added and filtered under reduced pressure and washed with diethyl ether and chloroform. The solid was air-dried and recrystallized from methanol/diethyl ether. For dienimidazolecopper(II) diperchlorate (see Figure 2-6c), 30 mL of 2 mM $Cu(ClO_4)_2 \cdot 6H_2O$ (98% ACROS Organics, New Jersey) in a methanol/acetonitrile (5:1) mixture was stirred with 3 mL of 2 mM triethylenediamine (≥97% Fluka, Netherlands) in water. Then, 10 mL of 2 mM imidazole in methanol was added to the mixture. After being left overnight, blue colored crystals were obtained.[98] All the solvents used in synthesis were purchased from Sigma-Aldrich Co., St. Louis, MO. Crystals were dissolved in water to make 10 mM stock solutions. For ESR experiments, samples were prepared in the presence of 25% (v/v) glycerol (≥99% Sigma-Aldrich Co., St. Louis, MO), with a final Cu(II) concentration of 1.25 mM.

The peptide PHGGGW, the Cu(II) binding domain of prion, was synthesized at the Molecular Medicine Institute, University of Pittsburgh, using standard fluorenylmethoxycarbonyl

chemistry.[99-100] Isotopically enriched [G-^{15}N]-Nα-Fmoc-Nτ-trityl-L-histidine was purchased from Cambridge Isotope

Laboratory (Andover, MA), in which all nitrogen atoms are ^{15}N enriched. Three different variants of amyloid-β(1−16) (DAEFRHDSGYEVHHQK) with each containing an ^{15}N enriched histidine at either position 6, 13, or 14 were synthesized at the Molecular Medicine Institute, University of Pittsburgh, using standard fluorenylmethoxycarbonyl chemistry.[99-100] Double-labeled peptides containing two ^{15}N enriched histidine residues were synthesized in the same manner. All the labeled amyloid-β (1−16) variants were purified by high performance liquid chromatography and characterized by mass spectroscopy. Nonlabeled amyloid-β (1−16) peptide was purchased from rPeptide (Bogart, GA). The peptide fragment DAHK, the N-terminus region of the human serum albumin, was purchased from Fisher Scientific, Hanover Park, IL. For peptide samples, the concentration of the peptide was 1.25 mM and an equimolar amount of Cu(II) was present in both the samples. Samples were prepared in Nethylmorpholine (NEM) buffer at pH 7.4 in 25% (v/v) glycerol and appropriate amounts of hydrochloric acid.

Single Crystal X-ray Data Collection

X-ray diffraction data for the one-imidazole and two-imidazole model complex structures were collected using a single crystal on a Bruker X8 Prospector Ultra CCD diffractometer with a CuKα (λ = 1.54178 A) ImuS radiation source. The parameters used during the collection of diffraction data for each structure are summarized in Supporting Information. Crystals were mounted in Fluorolube oil on a Mitegen mount and placed in a cold N_2 stream (150(1) K) for data collection. X-ray diffraction data for the four-imidazole model complex was collected on a Bruker Smart Apex CCD diffractometer with graphite-monochromated MoKα (λ = 0.71073 Å) radiation at room temperature. A single crystal was mounted with epoxy onto a glass fiber.

For each structure, unit-cell dimensions were derived from the least-squares fit of the angular settings of 999 strong reflections from the data collection. Data were corrected for absorption using the Bruker AXS program SADABS. Each structure was solved via direct methods, which located the positions of the non-hydrogen atoms. All non-hydrogen atoms were refined anisotropically. Final difference Fourier syntheses showed only chemically insignificant electron density. An inspection of F_o vs Fc values and trends based upon sin θ, Miller index, or parity group failed to reveal any systematic error in the data. All computer programs used in the data collection and refinements are contained in the Bruker program package Apex2 v.2013.10−0. All three crystal structures have been reported previously, and our results are in substantial agreement with those previously reported structures.[96-98]

Electron Spin Resonance Spectroscopy

A 200 mL aliquot of complex samples with a concentration of 1.25 mM was transferred into a quartz tube with an inner diameter of 3 mm. Glycerol (25%, v/v) was added as a cryoprotectant. All ESR experiments were performed on a Bruker ElexSys E580 Xband or a Bruker ElexSys E680 X-band FT/CW spectrometer equipped with Bruker ER4118X-MD5 and EN4118X-MD4 resonators, respectively. The temperature was controlled using an Oxford ITC503 temperature controller and an Oxford CF935 dynamic continuous flow cryostat connected to an Oxford LLT 650 low-loss transfer tube. Continuous-wave ESR experiments were carried out on sample solutions at 80 K and at X-band microwave frequency. The magnetic field was swept from 2600 to 3600 G for 1024 data points. A time constant of 10.24 ms, a conversion time of 20.48 ms, modulation amplitude of 4 G, a modulation frequency of 100 kHz, and a microwave power of 0.1993 mW were the other instrument parameters used for the CW experiment.

The three-pulse ESEEM experiments were performed on the sample solutions at 20 or 80 K, by using a $\pi/2 - \tau - \pi/2 - T - \pi/2$-echo pulse sequence with a $\pi/2$ pulse width of 16 ns. The first pulse separation, τ, was set at 144 ns, and the second pulse separation, T, was varied from 288 ns with a step size of 16 ns. The experiments were carried out at the magnetic field, where the ESR intensity was maximum. A four-step phase cycling was employed to eliminate unwanted echoes.[95, 101] The raw data was phase corrected, and the real part was selected. After the baseline correction, the spectra were fast Fourier transformed. Then the final spectra were obtained as the magnitude of the Fourier transforms.

ESEEM Data Analysis

We normalized the ESEEM spectra using the integrated intensity of ^{1}H ESEEM signal (13−16 MHz). Possible limitations of the above method are discussed in the results section. For a single ^{14}N nucleus coupled to an electron spin, the relative modulation depth is[38]

$$K_{14}^{\alpha}/K_1 = \frac{K_{14}^{\alpha}(1-K_1)}{K_1\left(2-K_{14}^{\alpha}-K_{14}^{\beta}\right)} \quad [1]$$

Where K is the modulation depth and subscripts 14 and 1 denote the ^{14}N and ^{1}H spin, respectively. Superscripts α and β denote the α and β spin manifolds of the electron spin, respectively.[38]

For two equivalent ^{14}N nuclei coupled to an electron spin the relative modulation depth becomes[38]

$$K_{14}^{\alpha\prime}/K_1 = \frac{4K_{14}^{\alpha}(1-K_{14}^{\alpha})(1-K_1)}{K_1[2(1-K_{14}^{\alpha})^2+(K_{14}^{\alpha})^2+2\left(1-K_{14}^{\beta}\right)^2+(K_{14}^{\beta})^2]} \quad [2]$$

$K_{14}^{\alpha\prime}$ is the modulation depth of the α spin manifolds of the two equivalent ^{14}N nuclei. The relative modulation depth of 1^{4N} increases with the addition of the ^{14}N nucleus, and the factor of increase is given by

$$\frac{(K_{14}^{\alpha\prime}/K_1)}{(K_{14}^{\alpha}/K_1)} = \frac{4(1-K_{14}^{\alpha})(2-K_{14}^{\alpha}-K_{14}^{\beta})}{2(1-K_{14}^{\alpha})^2+(K_{14}^{\alpha})^2+2\left(1-K_{14}^{\beta}\right)^2+(K_{14}^{\beta})^2} \quad [3]$$

If K_{14}^{α} and K_{14}^{β} are much smaller than 1, the factor converges to 2. The theoretical value for K_{14}^{α} and $K_{14}^{\beta}$is approximately 0.15, for a π/2 pulse length of 16 ns.

If two nonequivalent ^{14}N nuclei are coupled to the electron spin, the relative modulation depth is given as[38]

$$K_{14}^{\alpha\prime\prime}/K_1 \quad = \frac{(K_{14}^{\alpha}+K_{14'}^{\alpha}-2K_{14}^{\alpha}K_{14'}^{\alpha})(1-K_1)}{K_1[(1-K_{14}^{\alpha})(1-K_{14'}^{\alpha})+(1-K_{14}^{\beta})(1-K_{14'}^{\beta})]} \quad [4]$$

$K_{14}^{\alpha\prime\prime}$ is the modulation depth of the α spin manifolds of the two nonequivalent ^{14}N nuclei. The increase in the relative modulation depth with the additional ^{14}N nuclei is given by

$$\frac{(K_{14}^{\alpha\prime\prime}/K_1)}{(K_{14}^{\alpha}/K_1)} = \frac{(K_{14}^{\alpha}+K_{14'}^{\alpha}-2K_{14}^{\alpha}K_{14'}^{\alpha})(2-K_{14}^{\alpha}-K_{14}^{\beta})}{K_{14}^{\alpha}[(1-K_{14}^{\alpha})\left(1-K_{14'}^{\alpha}\right)+\left(1-K_{14}^{\beta}\right)\left(1-K_{14'}^{\beta}\right)]} \quad [5]$$

If K_{14}^{α} , $K_{14'}^{\alpha}$, K_{14}^{β} , and $K_{14'}^{\beta}$ are much smaller than 1, eq 5 simplifies to

$$\frac{(K_{14}^{\alpha\prime\prime}/K_1)}{(K_{14}^{\alpha}/K_1)} = 1+\frac{K_{14'}^{\alpha}}{K_{14}^{\alpha}} \quad [6]$$

If two 14N nuclei are equivalent (i.e., $K_{14}^{\alpha} = K_{14'}^{\alpha}$), the factor in eq 6 becomes 2.

However, obtaining modulation depth information from ESEEM time domain data is difficult as many components are overlaid in the signal. It has been shown that integrated intensities can be used to account for the changes in the modulation depth.[38] In the frequency domain ^{14}N ESEEM signal is well separated from the ^{1}H ESEEM signal, so it is possible to integrate separately. The ^{14}N ESEEM intensity is obtained by integrating between 0−11 MHz, and the ^{1}H ESEEM intensity is obtained for the region between 13−16 MHz.

2.3 RESULTS AND DISCUSSION

In this work we experimentally determine the validity of the use of ESEEM integration intensities to quantify the number of ^{14}N nuclei coupled to a Cu(II) center. To this end a series of model complexes with different numbers of imidazole ligands coordinated to copper are used. Then, the ESEEM analysis was carried out on two small peptides with known Cu(II)−histidine coordination, namely DAHK and PHGGGW peptides. The DAHK peptide is the N-terminus region of the human serum albumin (HSA) and coordinate Cu(II) in the well characterized ATCUN motive.[102] The DAHK−Cu(II) complex contains a single ^{14}N ESEEM active nucleus through the histidine imidazole coordination. The peptide PHGGGW is a truncated fragment of the octarepeat Cu(II) binding domain of the prion protein and has a known Cu(II) coordination including a crystal structure.[41] The PHGGGW−Cu(II) complex is specifically used as there are two nonidentical ^{14}N ESEEM active nuclei coupled to Cu(II). One ^{14}N nucleus is from the histidine imidazole coordination and the other from the peptide backbone coordination.[73] Then we used ESEEM to distinguish between the two proposed modes of coordination for component II of Aβ. Furthermore, the proportions of each histidine residue coordinated to Cu(II) ion as an equatorial ligand were measured with the use of systematic ^{15}N-labeled histidine residues.

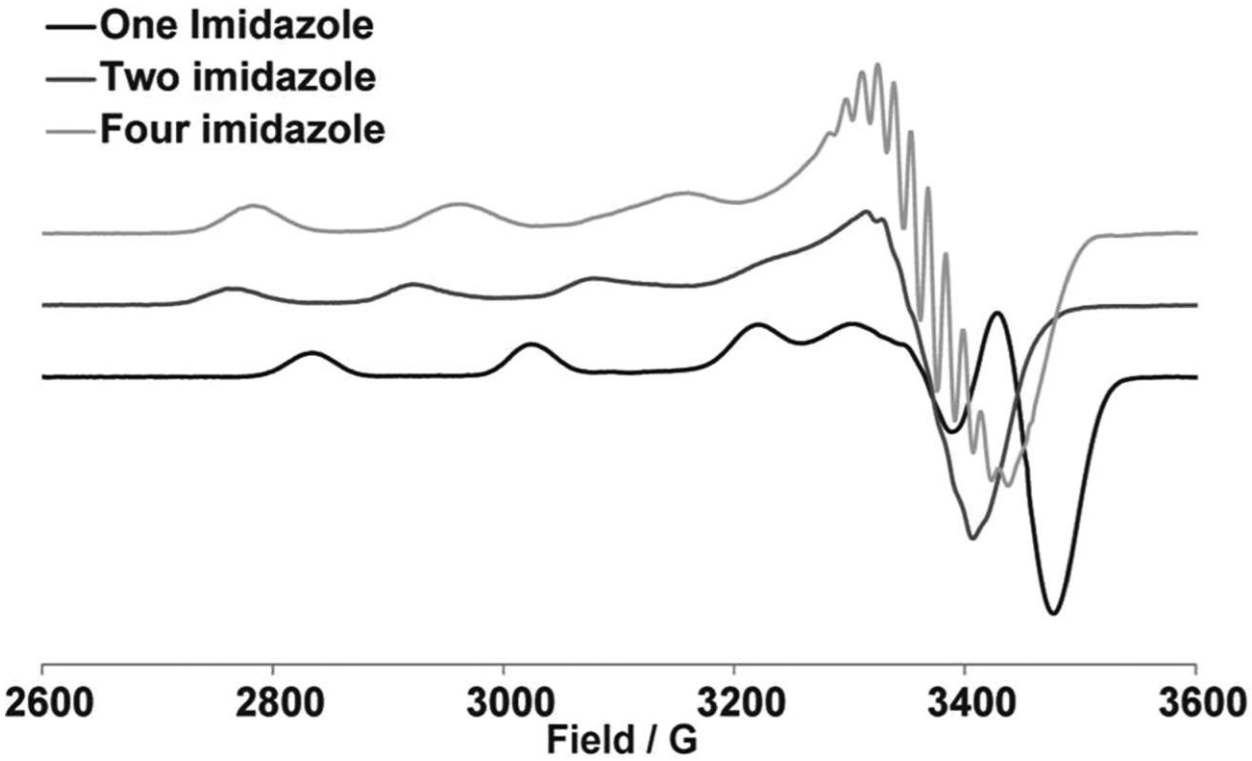

Figure 2-7 CW-ESR spectra of model complexes acquired at 80 K.

Electron Spin Resonance of Model Complexes.

In copper−imidazole complexes, the imidazole ring has a noncoordinated distal nitrogen, which contributes toward the ESEEM signal at X-band frequencies (~9.5 GHz), with pulse lengths used in this work ($\pi/2$ = 16 ns).[24] Hence, the ^{14}N ESEEM intensity will increase with the addition of imidazole rings to the coordination. In order to quantify the increase in ^{14}N ESEEM intensity we synthesized three model complexes (shown in Figure 2-6) containing 1, 2, and 4 imidazoles coordinated to a copper center, respectively. All three complexes were crystalized, and the structure of the complexes was verified using X-ray crystallography. The crystal structures of the complexes are shown in Figure 2-6. All these structures contain copper centers coordinated with four equatorial ligands according to the information gained from crystal structures. In the one-imidazole and the four-imidazole complexes, structures of the counter ion ligands perchlorate and the sulfate, respectively, are resolved as shown in Figure 2-6. ESR measurements are less sensitive to axial ligands[24] and are not considered in the analysis. The one-imidazole complex contains four directly coordinated nitrogens; three from the tridentate ligand, and one from the imidazole ring. Directly coordinated nitrogens do not contribute to ESEEM at X-band, with pulse lengths used in this work. The one-imidazole model complex contains just a single ^{14}N ESEEM active nucleus, which is in the imidazole ring.

First, CW-ESR experiments were carried out on the model complexes. As shown in Figure 2-7, the one-imidazole complex has $g_{\|}$ and $A_{\|}$ values of (2.22 ± 0.005) and (191 ± 1) Gauss, respectively. These ESR parameters correspond to four nitrogen nuclei coordinated to the Cu(II) center in the equatorial plane,[19] which is consistent with the structure of the one-imidazole complex, as shown in Figure 2-6a. The two imidazole complex has $g_{\|}$ and $A_{\|}$ values of (2.30 ± 0.005) and (158 ± 1) Gauss, respectively, which is consistent with a two nitrogen and two oxygen

nuclei equatorial coordination.[19] For the four-imidazole complex, $g_{\parallel}$ and $A_{\parallel}$ values are (2.26 ± 0.005) and (182 ± 1) Gauss, respectively, which again is consistent for four directly coordinated nitrogen nuclei.[19] Hence, CW-ESR parameters clearly show that model complexes maintain the same Cu(II) coordination environment in solution.

Then the ESEEM experiments were performed on model complexes. The ESEEM spectra of these complexes are shown in Figure 2-8. Nuclear quadrupole interactions (NQI) of ^{14}N give rise to features below 2 MHz. The broad feature around 4 MHz is due to the double quantum (DQ) transition of the remote nitrogen in an imidazole ring.[24, 41] The intensity of the DQ peak increases with the number of imidazole rings coordinated to the Cu(II) center.[95] A peak around 9 MHz (black arrow in Figure 2-8) is also indicative of multiple imidazole coordination.[35, 95] This peak is clearly observed in the two- and four-imidazole complexes.

The integrated intensity for ^{14}N-ESEEM was calculated for the region between 0−11 MHz and then divided by the ^{1}H ESEEM intensity integrated between 13 and 16 MHz. Details of the error calculation are provided in Appendix A. The normalized ^{14}N-ESEEM intensity increases from 8.4 to 21 when going from single imidazole to two imidazoles as shown in Table 2-1. When there are four imidazoles coordinated to the Cu(II) center, normalized ^{14}N-ESEEM intensity is increased to 40. Hence, there is a monotonic increase in the normalized ^{14}N-ESEEM intensity with the increase of number of imidazole rings coordinated.

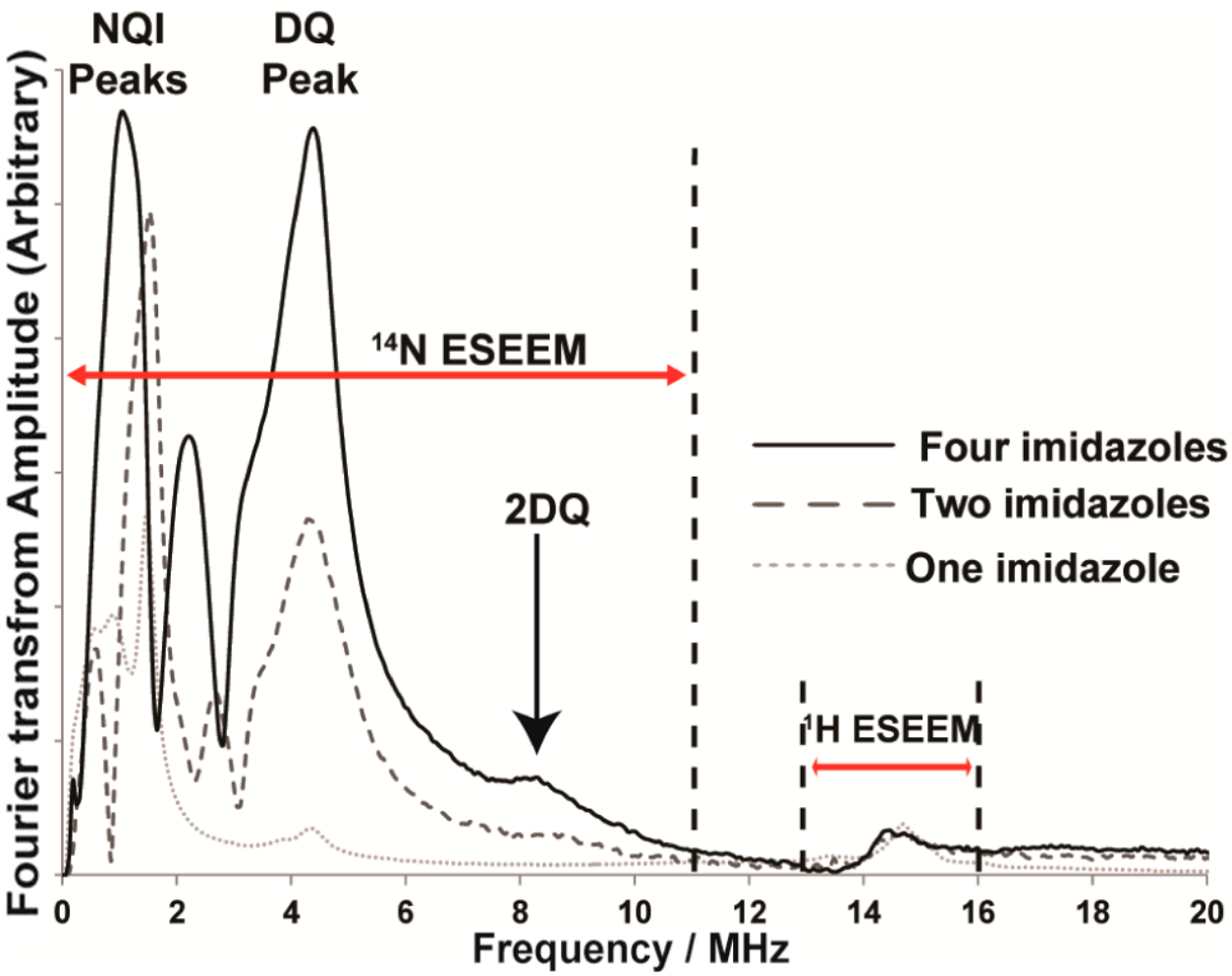

Figure 2-8 Experimentally obtained three-pulse ESEEM spectra model complexes at maximum $g_{\perp}$ position. Appearance of a peak around 9 MHz in two and four imidazole complexes is indicative of multiple imidazole coordination.

ESEEM Analysis on Cu(II)−Peptide Complexes with Known Coordination

In order to test our claim in a biologically relevant system, ESEEM experiments were conducted on two different peptide fragments with well-known Cu(II) coordination. The four amino acid peptide DAHK is the N-terminus fragment of the human serum albumin.[102] In the DAHK peptide, the imidazole ring of the histidine residue coordinates to the Cu(II) ion, and the distal nitrogen of the imidazole ring is the only ESEEM active nucleus as shown in Figure 2-9. The comparison between the ESEEM spectra of Cu(II)−DAHK and one-imidazole complex is shown in Figure 2-9. Both complexes show the characteristic three NQI peaks and the broad DQ peak. The intensities of the DQ peaks are comparable in the two complexes. The intensity of DQ peak reflects the number of imidazoles coordinated to the Cu(II) center.[29] The normalized integrated intensity for Cu(II)−DAHK is 7.0 ± 0.1 compared to 8.4 ± 0.1 for the one-imidazole complex (Table 2-1).

Then we used the PHGGGW peptide fragment, which is the Cu(II) binding domain of the prion protein.[41-42] Burns et al. resolved the Cu(II) coordination environment of the octarepeat fragment using ESR experiments and a crystal structure of the Cu(II)−PHGGGW complex.[41] As shown in Figure 2-10, Cu(II) is coordinated to an imidazole nitrogen in a histidine, two backbone nitrogens from two glycine residues,and an oxygen from a carboxylic group. The structure of the Cu(II) bound HGGGW pentapeptide was found to be unstable in solution due to the breaking of the axial water coordination.[78] However, the complex still maintains the equatorial square planar coordination.[78] Also, ESEEM results have indicated that histidine imidazole coordination and backbone coordination is present in the Cu(II)−PHGGGW complex in solution.[36, 71] The ESEEM spectra of the Cu(II)−PHGGGW complex and the two-imidazole complex are shown in Figure 2-10 for comparison. Given the different coordination environments the two spectra do not have

identical peak positions. Importantly, the intensity of the DQ peak is different. The two-imidazole complex has a larger DQ peak compared to the PHGGGW complex. The reported structure for the Cu(II)−PHGGGW structure contains two ^{14}N-ESEEM active nuclei from the distal nitrogen of the imidazole histidine and the backbone coordination as shown in Figure 2-10.[36] Hence, the intensity of the DQ peak is expected to be different between the two complexes, as DQ peak intensity is indicative of the number of imidazoles coordinated.[28-29] However, the normalized ^{14}N-ESEEM integrated intensity obtained for the Cu(II)−PHGGGW complex is similar to the integrated intensity of the two-imidazole complex. This information verifies that the integration method can predict the number of ^{14}N nuclei coupled to a Cu(II) center.

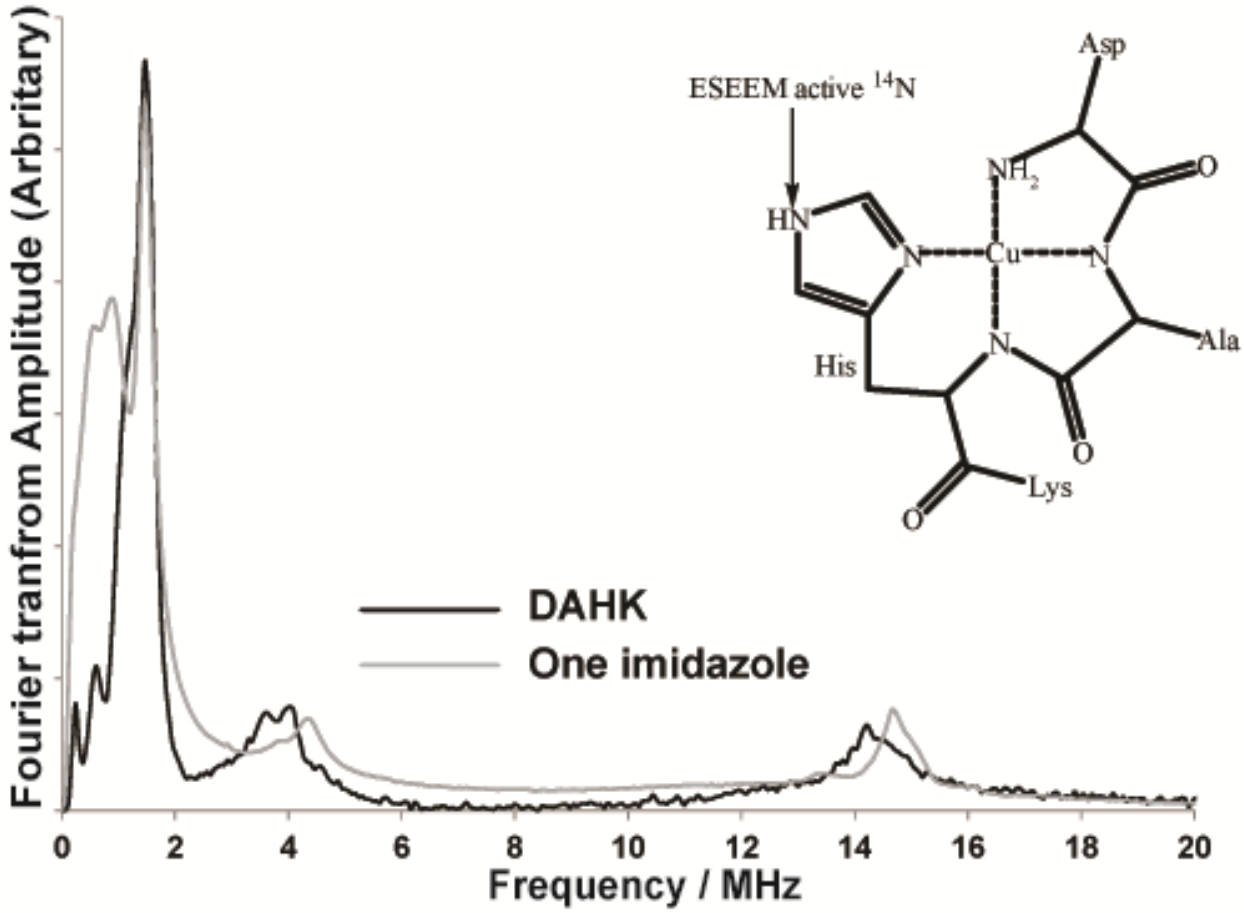

Figure 2-9 The comparison of ESEEM spectra of Cu(II) – DAHK complex and one imidazole complex. Only one ^{14}N-ESEEM active nuclei is present in the reported coordination of DAHK.

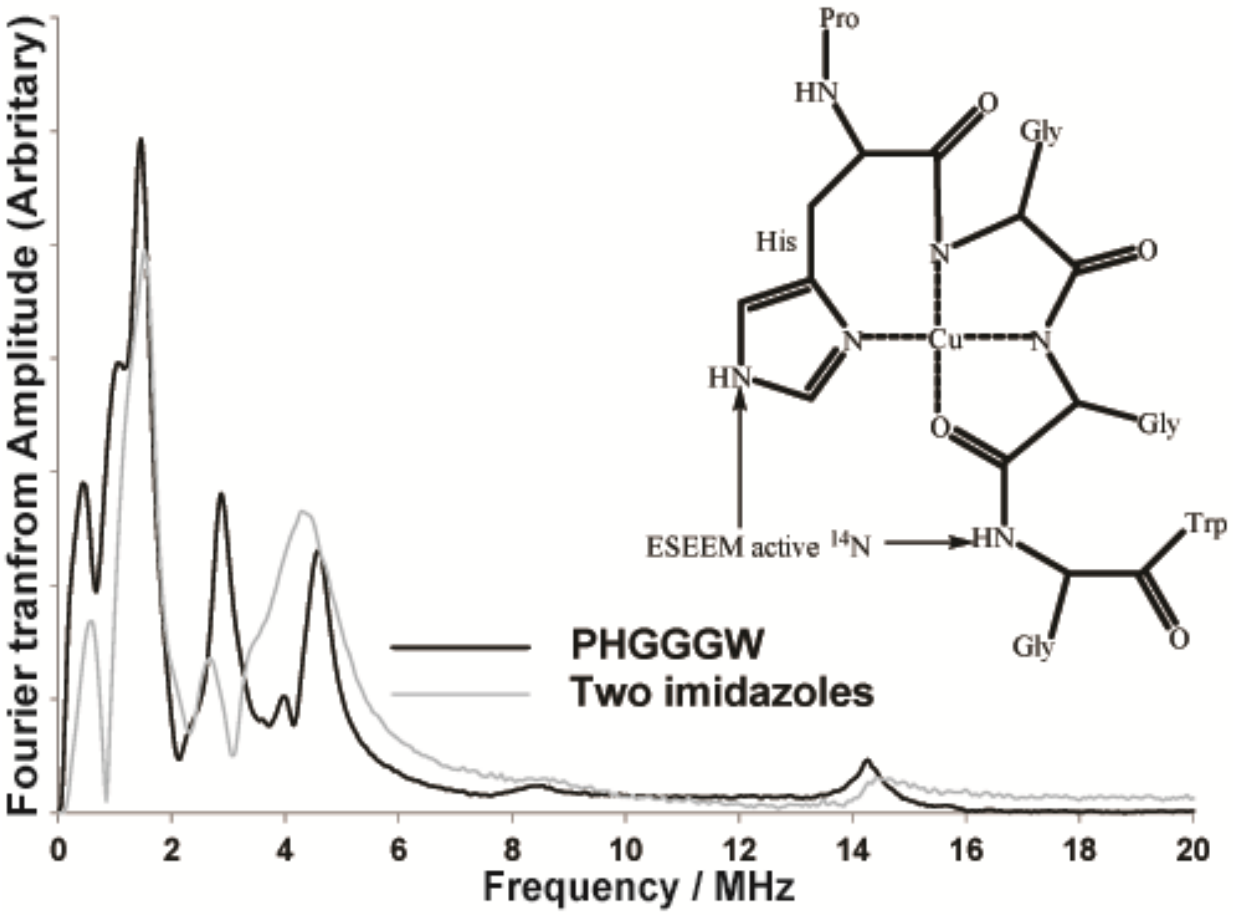

Figure 2-10 The comparison of ESEEM spectra of Cu(II)-PHGGGW complex and the two imidazole complex. Cu(II)-PHGGGW complex contains two ^{14}N-ESEEM active nuclei.

Quantification of Histidine Residues Coordinated to Component II of Cu(II)−Aβ(1−16) Complex.

The integration analysis was used to determine the number of nitrogens coupled to the Cu(II) ion in Aβ(1−16) in component II. As shown in the inset of Figure 2-11, Zn(II) selectively displaces Cu(II) coordinated to component I. At excess amounts of Zn(II) (ten equivalents of Zn(II)), component II accounts for ∼65% of the overall coordination (inset of Figure 2-11), where in the absence of Zn(II) the percentage is only 35%.[92] Amyloid aggregates in brain tissues contain approximately three times Zn(II) than Cu(II).[1] Hence, component II becomes the dominant Cu(II) coordination mode in vivo. Figure 2-11 shows the comparison between the two-imidazole complex and the Aβ(1−16)−Cu(II) complex at pH 8.7. At pH 8.7 only the component II of Cu(II) coordination exists.[5, 34] The integrated intensities tabulated in Table 2-1 suggest that two ^{14}N nuclei are coupled to the Cu(II) ion. The features of the ESEEM spectrum clearly illustrate the imidazole histidine coordination as shown in Figure 2-11. The peak around 2.8 MHz is indicative of backbone coordination.[41] The backbone coordination peak is possibly due to the coupling between the Cu(II) ion with the remote backbone nitrogen nuclei of Glu 3, where Cu(II) is coordinated to the carbonyl oxygen of Ala 2.[91] To further confirm the backbone coordination we performed HYSCORE experiments and as shown in Figure 2-12, the cross peak around (2.8 MHz, 4.3 MHz) (dashed circles) was clearly observed for all the peptide analogues tested. The presence of this cross peak further confirms the backbone coordination in component II [37, 41]

The normalized integrated intensity (^{14}N-ESEEM/^{1}H-ESEEM) of Aβ(1−16) is 17 compared to 21 and 22 for the two-imidazole complex and the PHGGGW, respectively. The lower value for Aβ(1−16) is possibly due to the smaller number of protons that interact with the Cu(II) center. The Cu(II) centers in the model complexes are solvent accessible. In Aβ(1−16) the

solvent−Cu(II) interaction may be restricted because of the neighboring amino acids. In our analysis we have normalized the integrated area of the ^{1}H-ESEEM peak to be the same for all spectra. Therefore, we may be underestimating the ^{14}N-ESEEM integrated intensity for Aβ(1−16). Nevertheless, the normalization method does suggest that Cu(II) is coupled to two ^{14}N-ESEEM active nuclei, not one or three. Hence, we can answer the crucial question of the number of histidines coordinated to component II.

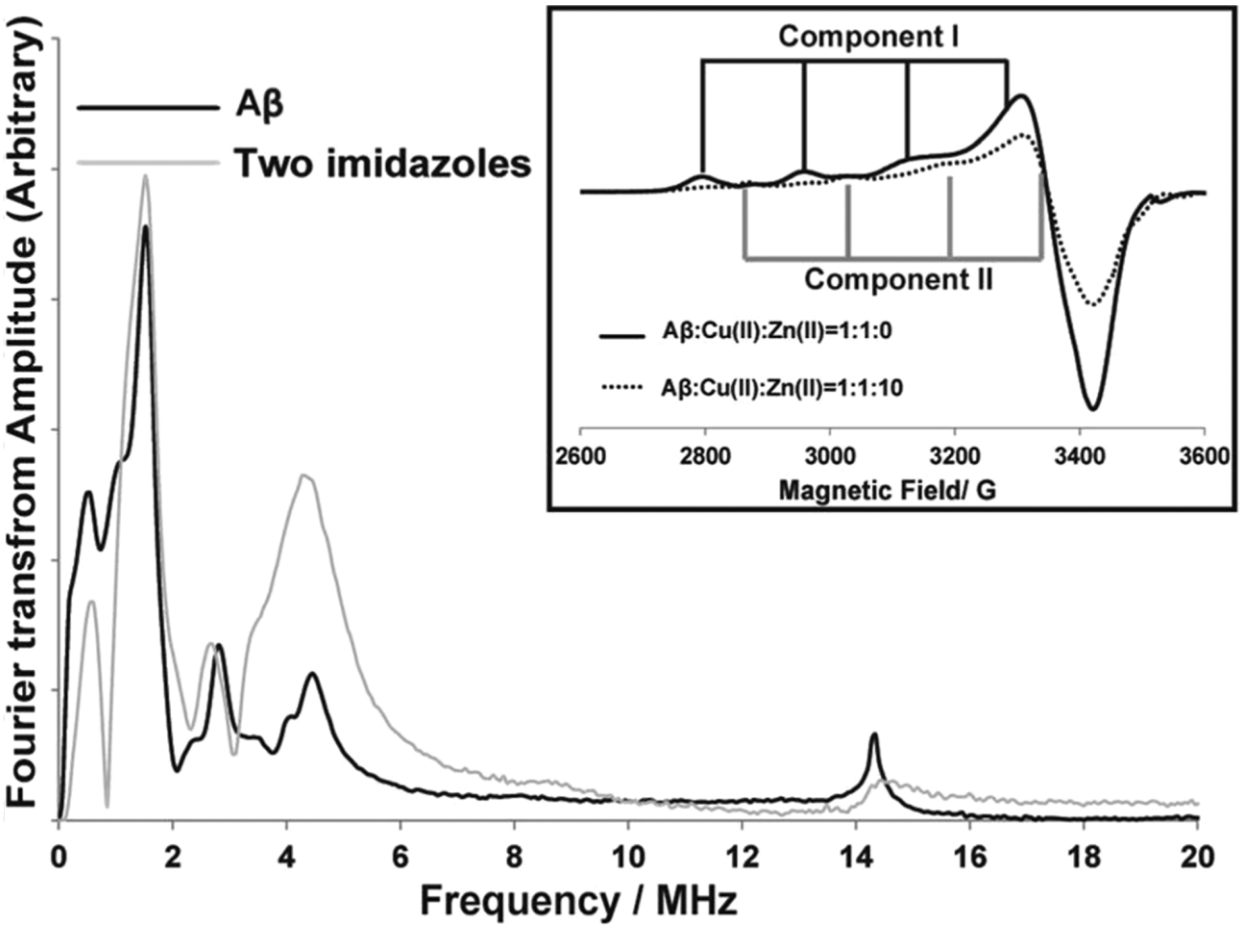

Figure 2-11 Comparison of ESEEM spectra of Cu(II)−Aβ(1−16) complex at pH 8.7 and the two-imidazole complex. The inset shows the increase of component II Cu(II) contribution in the presence of Zn(II).

Table 2-1 Integrated intensities of the peaks at the ^{14}N-ESEEM region (0–11 MHz) and ^{1}H-ESEEM region (13-16 MHz) and the ratio of ^{14}N to ^{1}H integrated intensities

Complex	**^{14}N-ESEEM**	**^{1}H-ESEEM**	**^{14}N/^{1}H**
Four imidazole	3486 ± 3	87 ± 2	40± 1.5
Two imidazole	1868 ± 2	87 ± 1	21 ± 1.0
One imidazole	723 ± 0.4	86 ± 0.2	8.4 ± 0.1
DAHK	603 ± 0.4	86 ± 0.2	7.0 ± 0.1
PHGGGW	1875 ± 0.7	86 ± 0.2	22 ± 0.1
Aβ(1 – 16) pH 8.7	1412 ± 0.7	87 ± 0.2	17 ± 0.1

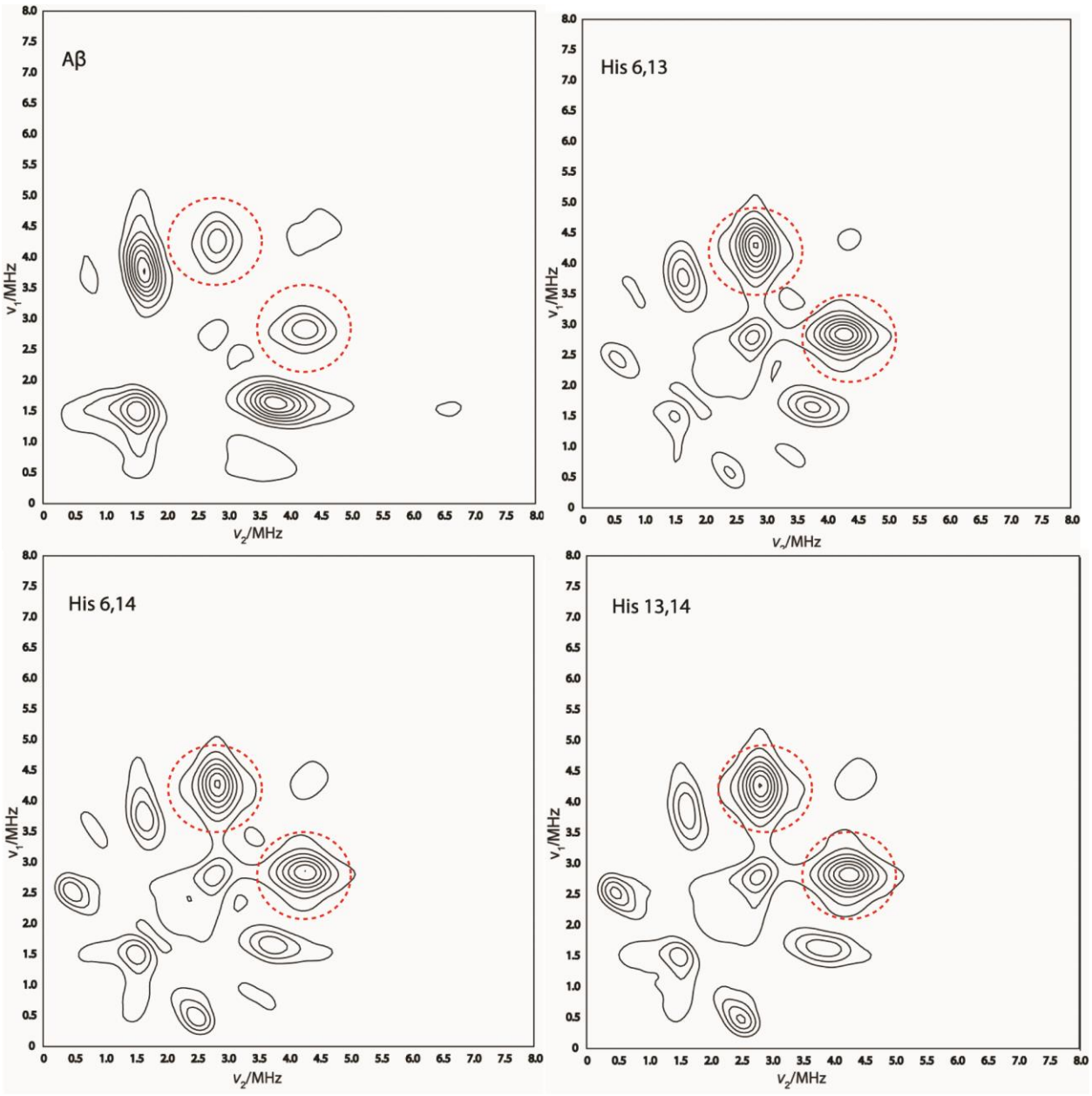

Figure 2-12 HYSCORE spectra acquired for Aβ samples at pH 8.7. Peaks resulting from the backbone coordination are indicated by dashed circles.

Contributions of Each Histidine toward Component II and Physiological Importance.

Three-pulse ESEEM spectroscopy was used in conjunction with isotopic substitution to determine the coordination of component II. Specifically the aim of these experiments was to provide more insight into the proportions of histidine residues involved in component II coordination. First, double-labeled variants of Aβ(1−16) were used. Two histidine residues at a time are isotopically labeled with ^{15}N. Upon ^{15}N substitution, the modulation depths of the frequencies due to ESEEM active ^{14}N nuclei will decrease. This decrease is because the single quantum transition of ^{15}N nuclei does not substantially contribute to the ESEEM signal.[21, 31, 39, 103-105] We compare the integrated intensities of nonlabeled and ^{15}N labeled variants. As the modulation depth of the ^{1}H frequency is not affected by the ^{15}N substitution, the ^{1}H ESEEM peak is used to normalize the integrated intensity of ^{14}N ESEEM. Because two of the three histidine residues are labeled, the ^{14}N ESEEM signal intensity results only from the single nonlabeled histidine. This isotopic substitution provides a direct method to determine the extent to which each histidine residue is involved in component II.

All the samples were at pH 8.7, and the experiments were carried out at 3355 G, which corresponded to the maximum signal in the echo detected field sweep. The ESEEM intensities are integrated between 0 and 11 MHz in all the ESEEM spectra collected (Figure 2-13). The integrated ESEEM intensity of the His 6,13-labeled variant was ∼40% of that of the nonlabeled variant. In the His 6,13 variant, His 14 is the only unlabeled histidine residue and the ^{14}N ESEEM intensity results from only His 14. Likewise, His 13 contributes ∼40% and His 6, 20%, toward the component II Cu(II) coordination (Table 2-2). The integrated intensities are tabulated in the Table 2-3.

To further confirm the proportions of the histidine residues, we performed the experiments

using single-labeled variants in which only one histidine is labeled at a time. The decrease in the signal intensity in the ^{14}N ESEEM region with respect to the nonlabeled variant indicates the extent of the involvement of the labeled histidine in the coordination. The ESEEM spectra for single-labeled variants are shown in Figure 2-14. The integrated ^{14}N ESEEM intensities for single-label variants as shown in table 2-4 follow the similar pattern of His 14 ≈ His 13> His 6 as observed with the double-label variants. This trend can be rationalized by the pKa values of the histidine side chains. His 6 has a pKa of 7.1, while for His 13 and 14 the pKa values are 7.7 and 7.8, respectively.[106] As the imidazole ring in His 6 has a lower pKa value, ring nitrogens will be deprotonated at lower pH values than in His 13 and 14. This deprotonation makes the ring nitrogens accessible for Cu(II) coordination. When the pH is raised, His 13 and 14 rings become more accessible for Cu(II) coordination. Hence the proportions of His 13 and 14 are increased with the increase in pH. These results are in accordance with an X-ray examination of Aβ(1−16), which suggests that His 13 and His 14 are readily accessible for metal ion coordination.[107] The design of a curcumin scaffold was discussed in this work, which is used to compete for Cu(II) coordination with the His 13−His 14 dyad.[107] In addition, steric reasons may play a role in this trend observed.

Hence, we suggest only one histidine residue is involved in component II, with a preference to His 13 and His 14 over His 6. The other residues involved in the component II coordination are the carbonyl oxygen of Ala 2,[108] the Nterminus (Asp 1),[34] and the amide nitrogen of Ala 2.[34] The peak around 2.8 MHz in the ESEEM spectra is indicative of backbone coordination and further confirms the involvement of the peptide backbone in component II coordination.[36-37, 41-42] The possible subcomponents of component II are shown in Figure 2-15.

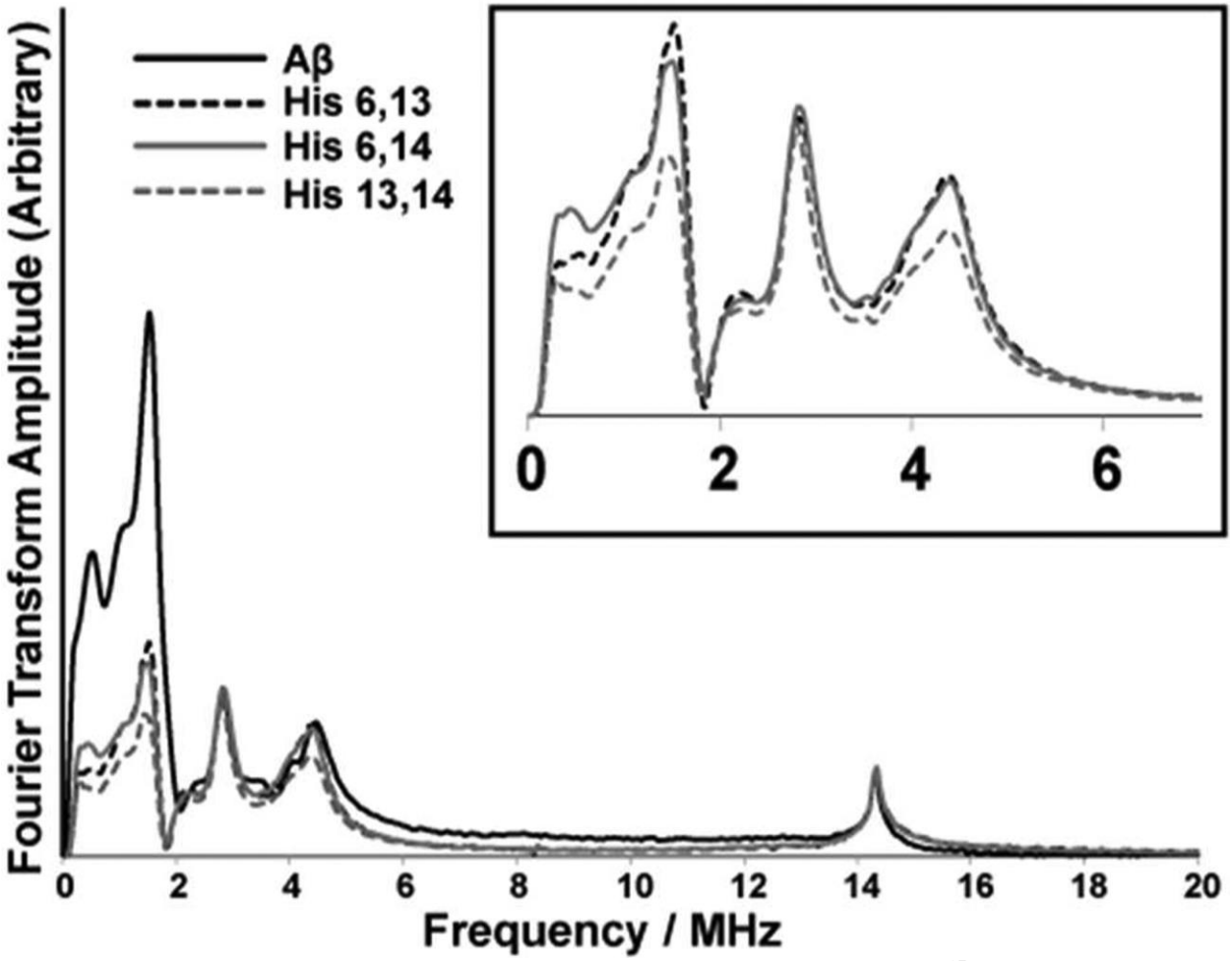

Figure 2-13 Three-pulse ESEEM spectra of the nonlabeled and single ^{15}N-labeled Aβ(1−16) variants mixed with equimolar amounts of Cu(II) at pH 8.7. The decrease in intensity below 8 MHz in ^{15}N labeled Aβ(1−16) variants gives the contribution of each histidine residue for component I in Aβ(1−16)−Cu(II). The inset shows an expanded view of the 0−6 MHz region for the labeled peptides.

Table 2-2 Contributions from each histidine residue at different pH values for Aβ (1 – 16)-Cu(II) complex.

pH	**His 6**	**His 13**	**His 14**
6.0(comp I only)[38]	50%	25%	25%
7.4(comp I and II)[83]	33%	33%	33%
8.7(comp II only)	20%	40%	40%

Table 2-3 Relative integrated intensities of ESEEM spectra of the nonlabeled and ^{15}N- double labeled Aβ(1 – 16) variants at pH 8.7 mixed with an equimolar amount of Cu(II) at the ^{14}N-ESEEM region (0 – 11 MHz) and ^{1}H-ESEEM region (13 – 16 MHz) and the relative contribution from each histidine.

Sample	**^{14}N-ESEEM**	**^{1}H-ESEEM**	**$^{14}N/^{1}H$**	**% involvement**
Aβ(1-16)	10767 ± 7	951 ± 5	11.32 ± 0.1	
His 6,13	4270 ± 7	950 ± 5	4.49 ± 0.1	39.6 ± 1
His 6,14	4313 ± 7	950 ± 5	4.54 ± 0.1	40.1 ± 1
His 13,14	2795 ± 7	950 ± 5	2.94 ± 0.1	25.9 ± 1

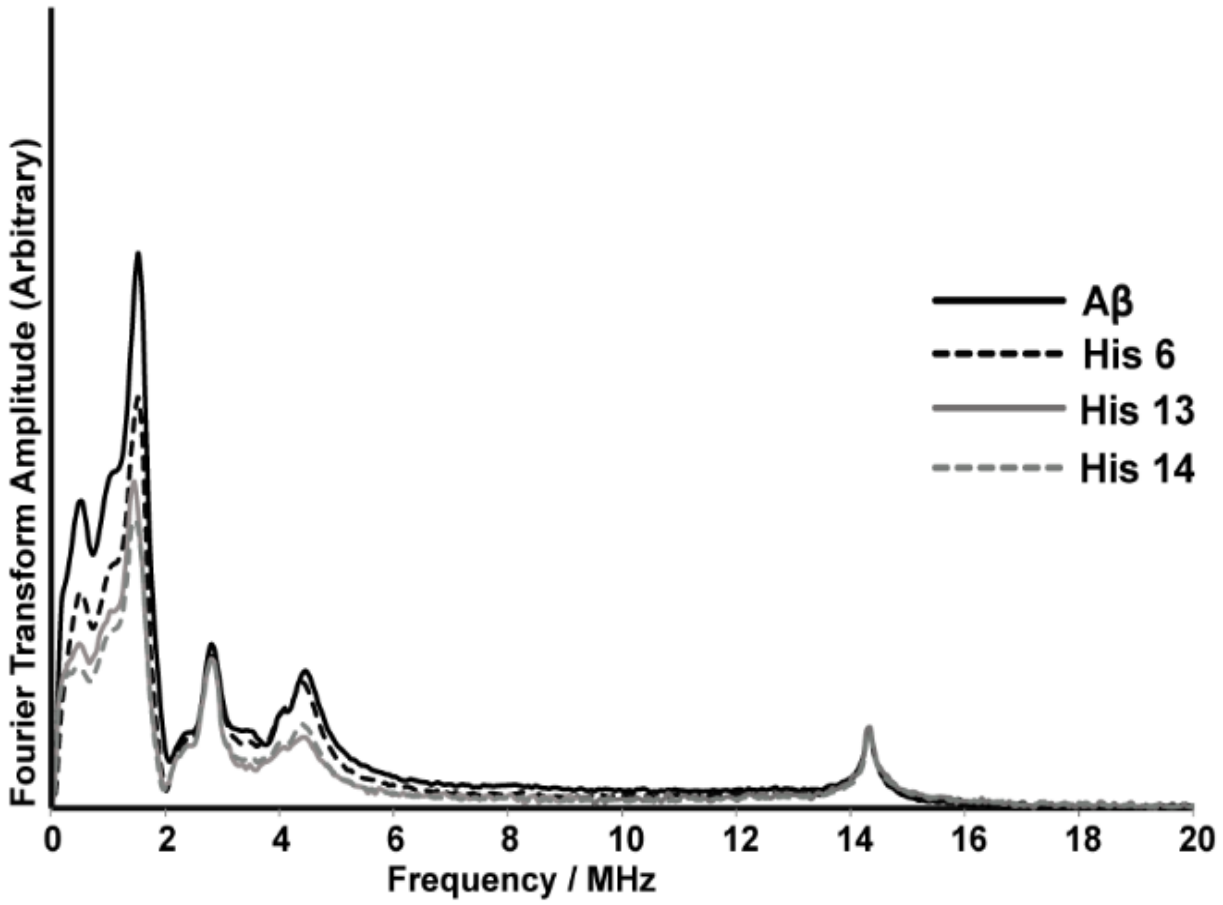

Figure 2-14 Three-pulse ESEEM spectra of the nonlabeled and single ^{15}N labeled Aβ(1 – 16) variants mixed with equimolar amounts of Cu(II) at 3355 G at pH 8.7. The decrease in intensity below 11 MHz in ^{15}N labeled Aβ(1 – 16) variants gives the contribution of each histidine residue for component II in Aβ(1 – 16)-Cu(II).

Table 2-4 Relative integrated intensities of ESEEM spectra of the nonlabeled and ^{15}N-single labeled Aβ(1 – 16) variants at pH 8.7 mixed with an equimolar amount of Cu(II) at the ^{14}N-ESEEM region (0 – 11 MHz) and ^{1}H-ESEEM region (13 – 16 MHz) and the relative contribution from each histidine.

Sample	^{14}N-ESEEM	^{1}H-ESEEM	$^{14}N/^{1}H$	% reduction
Aβ(1-16)	5847 ± 4	515 ± 3	11.35 ± 0.07	
His 6	4673 ± 3	508 ± 2	9.20 ± 0.04	18.9 ± 0.7
His 13	3329 ± 5	500 ± 4	6.66 ± 0.05	41.3 ± 0.8
His 14	3431 ± 3	466 ± 2	7.36 ± 0.03	35.1 ± 0.7

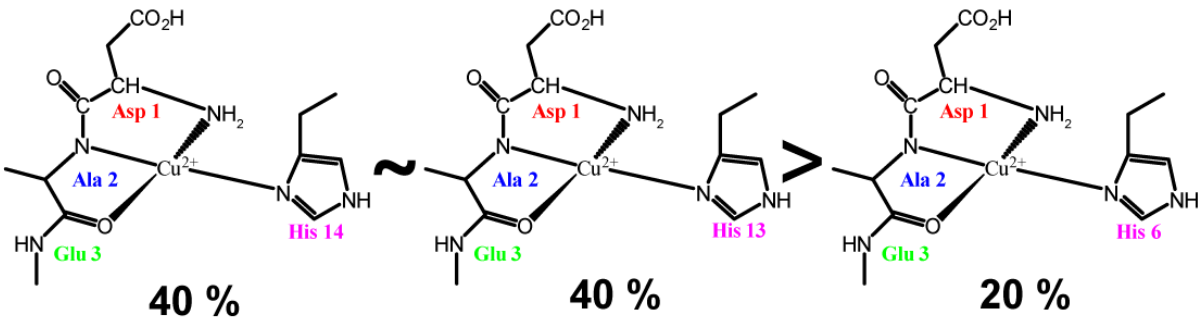

Figure 2-15 Different Cu(II) binding modes for component II. His 13 and His 14 equatorially coordinate to Cu(II) more than His 6.

Our ESEEM results performed using both the double and single ^{15}N-labeled histidine residues indicate that His 13 and His 14 have a higher preference for the equatorial coordination position in Cu(II) component II coordination. Chemically, component II Cu(II) coordination is really interesting as Zn(II) is not able to displace Cu(II).[92] Biologically, it is important to understand the component II coordination, as component II may be the most significant Cu(II) coordination in vivo, as Zn(II) coexists with Cu(II). The insight into the component II coordination, more importantly the proportions of subcomponents, will shed light on the role of metal ions in Alzheimer's disease.

2.4 SUMMARY

We experimentally validated the use of ESEEM intensities to quantify the number of ^{14}N nuclei coupled to a Cu(II) ion. A monotonic increase in the ^{14}N ESEEM intensities were observed for the model complexes synthesized with different numbers of imidazole rings. Then, the validity of the method was tested with two well-characterized Cu(II) binding peptides. We used our method to solve an important structural problem in Aβ−Cu(II) complex formation. We determined that only a single histidine residue is coordinated to Cu(II) ion in component II in Aβ. Finally, in component II, Cu(II) uses His 13 and His 14 as an equatorial ligand over His 6. The proportions of the three histidine residues in Cu(II) coordination can be rationalized by the pKa values of the histidine side chains. Shedding light into the component II coordination was critical as component II might be the dominant Cu(II) coordination mode of Aβ *in vivo*.

2.5 ACKNOWLEDGEMENTS

We are grateful to the peptide synthesis facility at the University of Pittsburgh for peptide preparation. This work was supported by a National Science Foundation (MCB 1157712) grant. The Bruker ElexSys E680 FT/CW spectrometer was purchased with funds from National Institutes of Health Grant 1S10RR028701.

3.0 Zn(II) IONS SUBSTANTIALLY PERTURB Cu(II) ION COORDINATION IN AMYLOID BETA AT PHYSIOLOGICAL pH

This work is written in collaboration with Sunil Saxena, and has been published in Journal of Physical Chemistry B, 2013, V. 117, 9986-9394

3.1 INTRODUCTION

Metal ion competition in biological systems is important for maintaining a proper ion balance, which in turn is critical for homeostasis.[109] Copper and zinc ions play critical roles in many biological pathways, including respiration, cell signaling, and electron transfer.[110-112] In the central nervous system, metal ion competition is critical as these metal ions are involved in a large variety of activities, including the development and maintenance of enzymatic activities, neuro transmission, etc.[113] Ionic imbalance in the central nervous system can lead to several neurological diseases, such as Alzheimer's disease, which is the most common cause of neurodegenerative dementia.[114-116]

Herein we examine the metal-binding competition in the Aβ peptide which is involved in Alzheimer's disease. Much research has been conducted to determine the role metal ions play in the etiology of Alzheimer's disease. Interestingly, micro-particle induced-ray emission microscopy measurements have shown that amyloid aggregates in brain tissues show abnormally high levels of Cu(II) and Zn(II)[1]. Furthermore, these metal ions are co-localized within the Aβ deposits.[1] Several coordination modes have been proposed for these metal ions in Aβ on the basis

of several spectroscopic techniques such as nuclear magnetic resonance (NMR), circular dichroism, X-ray absorption spectroscopy, electrospray-ionization mass spectroscopy, and Raman spectroscopy.[5, 7, 84, 117] Most of these investigations were focused on single metal ion coordination in Aβ. In this work, we utilize electron spin resonance (ESR) in conjunction with isotopic labeling to establish the coordination environment of Cu(II) in the presence of Zn(II).

The higher concentration of these ions in amyloid plaques[1] raises the possibility that these metal ions might be involved in the plaque formation. Aβ peptide undergoes metal-induced oligomerization under physiological conditions.[17] It is important to note that the aggregated states of Aβ-Cu(II) and Aβ-Zn(II) are very different. Saxena and co-workers reported that Cu(II) induces mature fibril formation at subequimolar concentrations, while granular amorphous aggregates are observed at higher concentrations of Cu(II).[4] Zn(II) on the other hand forms more amorphous aggregates rather than fibrillar aggregates even at sub-equimolar concentrations.[118-119] It has been suggested that the different coordination modes of Cu(II) and Zn(II) ions in Aβ are related to the different morphologies and toxicities of aggregates.[120-121]

The Cu(II) ion coordination in Aβ(1−16) has been shown to be identical to that in the full length Aβ.[122-124] Continuous wave electron spin resonance (CW-ESR) spectroscopy has revealed that there are two major coordination modes in Aβ- Cu(II), known as component I and component II.[34, 81, 91] Component I is the major Cu(II) coordination mode at physiological pH, accounting for 65−75% of the overall coordination.[5, 38] A number of experimental techniques have revealed that the histidine residues in Aβ at positions 6, 13, and 14 are involved in the Cu(II) coordination.[5, 7, 34, 84] Previous work done in our group using electron spin echo envelope modulation (ESEEM) spectroscopy and hyperfine sublevel correlation (HYSCORE) showed that all three histidine residues in Aβ(1−16) are involved in the coordination of Cu(II).[83] In component I, Cu(II) is thought

to be coordinated to two out of three histidine residues present in Aβ at positions 6, 13, and 14. Depending on which histidine residues are coordinated to Cu(II), two possible coordination modes for Cu(II) component I were proposed at pH 6.0.[91] Component IA contains simultaneous coordination of His 6 and His 13, while component IB contains His 6 and His 14 (Figure 3-1). At pH 6.0, the simultaneous coordination of Cu(II) by His 13 and His 14 is almost nonexistent. However, Shin et al. showed that simultaneous coordination of His 13 and His 14 is as important as His 6 and His 13 coordination at physiological pH.[38] Thus, a subcomponent IC, as shown in Figure 3-1, was introduced to account for the simultaneous His 13 and His 14 coordination. A recent investigation done in Aβ(1−40) fibrils using pulsed ESR revealed a bis-cis-His equatorial coordination geometry for Cu(II).[93] Also, this research proposed a structure in which Cu(II) is coordinated to His 6/His 13 and His 6/His 14 alternatively along the fibrillar axis on opposite sides of the β-sheet structure.[93] The other two equatorial ligands for Cu(II) component I are believed to be the N-terminus[34, 91, 123] and the carbonyl oxygen from Asp 1.[91]

The metal-binding site for Zn(II) ion lies in the N-terminal hydrophilic region of Aβ(1−16), as is the case for Cu(II).[125-126] It is believed that all three histidine residues are involved in the coordination of Zn(II) in Aβ(1−16).[126-130] Classically, Zn(II) coordination involves four to six ligands. The identities of other ligands are still controversial. The Aβ ligands proposed in binding Zn(II) in addition to the three histidine residues are the N-terminal amine from Asp 1, the Glu 11 carboxylate side chain, the deprotonated amide of the Arg 5 backbone, and Tyr 10.[5]

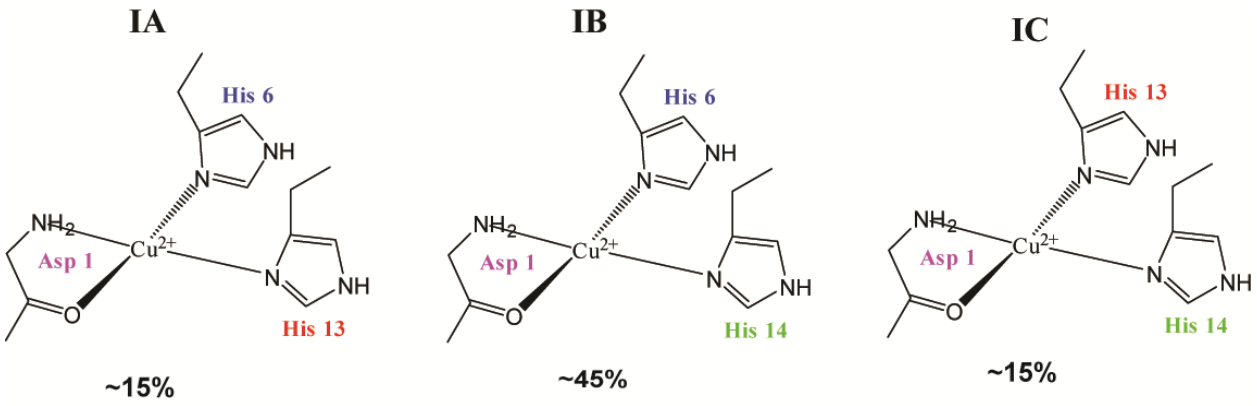

Figure 3-1 Three proposed subcomponents for component I in Cu(II) coordinated to Aβ peptide and the percentages of each component at pH 7.4. In subcomponent IA, His 6 and 13 simultaneously coordinate the Cu(II) ion in the equatorial plane. Subcomponent IB Cu(II) coordinates His 6 and 14, while subcomponent IC coordination contains His 13 and 14.

The Cu(II) coordination in Aβ(1−16) is heterogeneous and involves all three histidine residues in different coordination modes. Given the coexistence of Cu(II) and Zn(II) in amyloid plaques, it is critical to study the Cu(II) coordination in the presence of Zn(II). This represents a better depiction of the in vivo environment. We used CW-ESR spectroscopy in conjunction with simulations to determine how Zn(II) competes with Cu(II) for Aβ(1−16) coordination at physiological pH. These results show that the overall affinity of Cu(II) toward Aβ(1−16) is higher than that of Zn(II). Importantly, only component I of Cu(II) was substituted by Zn(II). ESEEM experiments were performed at low magnetic field strength (2800 G), at which only component I of Cu(II) coordination is present. Single-labeled and double-labeled peptides containing one and two ^{15}N isotopically labeled histidine residues were used to obtain detailed information on the role of each histidine residue in Cu(II) coordination. In the presence of an equimolar amount of Zn(II), the ESEEM results suggest that approximately half of the peptides in the ensemble use His 14 as an equatorial ligand for Cu(II) coordination in component I. Furthermore, the proportion of subcomponent IC was increased in the presence of Zn(II). The atomic force microscopy (AFM) results obtained using Aβ(1−40) show that amorphous aggregates are prevalent in the presence of both Zn(II) and Cu(II).

3.2 EXPERIMENTAL SECTION

Peptide Synthesis and Cu(II)/Zn(II) Complex Preparation.

Isotopically enriched [G-15N]-Nα-Fmoc-Nτ-trityl-L-histidine, in which all nitrogen atoms are ^{15}N-enriched, was purchased from Cambridge Isotope Laboratory (Andover, MA). Three different variants of amyloid-β(1−16) (DAEFRHDSGYEVHHQK) containing an ^{15}N-enriched

histidine at position 6, 13, or 14 were synthesized at the Molecular Medicine Institute, University of Pittsburgh, using standard fluorenylmethoxycarbonyl chemistry.[99-100] Double-labeled peptides containing two ^{15}N-enriched histidine residues were synthesized in the same manner. All the labeled amyloid-β(1−16) variants were purified by high-performance liquid chromatography and characterized by mass spectroscopy. Nonlabeled amyloid-β(1−16) peptide was purchased from rPeptide (Bogart, GA). Isotopically enriched (98.6%) $^{63}CuCl_2$ was purchased from Cambridge Isotope Laboratory, and anhydrous $ZnCl_2$ powder (≥99.995% metal basis) was purchased from Sigma-Aldrich Co. (St. Louis, MO). The enriched isotope was used to minimize inhomogeneous broadening of the Cu(II) ESR spectra. N-Ethylmorpholine (NEM) was purchased from Sigma-Aldrich Co.

The 2.5 mM solutions of peptides were prepared in 100 Mm NEM buffer (pKa = 7.8) at pH 7.4 in 50% (v/v) glycerol and appropriate amounts of hydrochloric acid. Cu(II) and Zn(II) stock solutions at 10 mM were prepared in NEM buffer. Appropriate amounts of stock solutions of Cu(II) and Zn(II) were added to a tube. Then the peptide was added to the tube containing Cu(II) and Zn(II) to make sure the peptide coordinates with both the metal ions simultaneously. The final peptide concentration of the ternary complexes was 1.25 mM. For all ESEEM experiments equivalent amounts of Cu(II) and Zn(II) were added (peptide:Cu(II):Zn(II) = 1:1:1). For CW experiments the metal ion concentrations were changed to provide the desired ratios. Samples of double-isotopic labeled peptide were prepared following the same procedure used for the single-isotopic labeled peptides.

Electron Spin Resonance Spectroscopy

A 200 μL aliquot of the sample was transferred into a quartz tube with an inner diameter of 3 mm. Electron spin resonance experiments were performed on either a Bruker ElexSys E580

or a Bruker ElexSys E680 X-band FT/CW spectrometer equipped with a Bruker ER4118X-MD5 or EN4118X-MD4 resonator, respectively. The temperature was controlled using an Oxford ITC503 temperature controller and an Oxford CF935 dynamic continuous flow cryostat connected to an Oxford LLT 650 lowloss transfer tube. All samples were frozen quickly by immersion in liquid nitrogen. Then the samples were inserted into the sample cavity which was precooled to the desired temperature (20 or 80 K).

Continuous-wave ESR experiments were carried out on sample solutions at 80 K with a microwave frequency of approximately 9.69 GHz. The magnetic field was swept from 2600 to 3600 G for 1024 data points. A time constant of 40.96 ms, a conversion time of 81.92 ms, a modulation amplitude of 4 G, a modulation frequency of 100 kHz, and a microwave power of 0.1993 mW were the other instrument parameters used for the CW experiment. The experimentally obtained spectra were compared with simulations using Bruker Simfonia.

Three-pulse ESEEM experiments were performed on the sample solutions at 20 K, using a $\pi/2-\tau-\pi/2-T-\pi/2-$echo pulse sequence with a $\pi/2$ pulse width of 16 ns. The first pulse separation, τ, was set at 144 ns, and the second pulse separation, T, was varied from 288 ns with a step size of 16 ns with the magnetic field strength fixed at 2800 G. Component I of the Cu(II)-Aβ(1−16) complex is almost exclusively observed at this magnetic field at physiological pH. Four-step phase cycling was employed to eliminate unwanted echoes.[95, 101] The raw data were phase corrected, and the real part was selected. After the baseline correction, the data were fast Fourier transformed. Then the final spectra were obtained as the magnitude of the Fourier transforms.

Four-pulse HYSCORE experiments were carried out at 20 K with a $\pi/2-\tau-\pi/2-t1-\pi-t2-\pi/2-\tau-$echo pulse sequence with $\pi/2$ and π pulse lengths of 16 and 32 ns, respectively. The first pulse separation, τ, was set at 144 ns, and both the second (t1) and third (t2) pulse separations were

varied with a step size of 16 ns and 100 shots per points. The final data consisted of 256 data points in both t1 and t2. The magnetic field was fixed at 3360 G, where the echo intensity is a maximum. Four-step phase cycling was employed to eliminate unwanted signals. The real parts of the collected two-dimensional data were baseline corrected and zero filled to 1024 points in both dimensions. After the two-dimensional Fourier transformation was performed, the final spectra were obtained as contour plots of the magnitude of the Fourier transforms.

ESEEM Data Analysis

For systems where Cu(II) is coordinated to ^{14}N, the ESEEM spectrum contains three characteristic peaks between 0 and 2 MHz.[27-31] When the exact cancellation condition is fulfilled, these three ESEEM frequencies correspond to υ_0, υ_-, and υ_+ for the nuclear quadrupole interaction (NQI) transitions.

$$\nu_0 = \frac{e^2qQ\eta}{2h};\ \nu_- = \frac{e^2qQ(3-\eta)}{4h};\ \nu_+ = \frac{e^2qQ(3+\eta)}{4h} \qquad [1]$$

In the equations above e is the electron charge, q is the z-component of the electric field gradient across the nucleus, Q is the ^{14}N nuclear quadrupole moment, η is the asymmetry parameter, and h is Planck's constant.

Apart from these three NQI peaks there is a broad peak around 3.8 MHz, which is attributed to a double quantum transition (DQ) [27-31]. The double quantum transition frequency is given by[32]

$$\nu_{DQ} = 2\sqrt{\left(\nu_I + \frac{A^2}{2}\right) + \left(\frac{B}{2}\right)^2 + \left(\frac{e^2qQ}{4h}\right)(3+\eta^2)} \qquad [2]$$

Where ν_{DQ} is the double quantum transition frequency, ν_I is the Larmor frequency of ^{14}N, and A and B are the secular and the pseudo secular part of the hyperfine interaction respectively.

In this work we compare the ESEEM signals of wild type Aβ (1–16) with ^{15}N labeled Aβ (1–16) peptides. Upon ^{15}N substitution the modulation depths of the signals due to ^{14}N nuclei will

decrease in ESEEM. This decrease is because the single quantum transition of ^{15}N nuclei does not substantially contribute to the ESEEM signal.[21, 31, 39, 103-105] In our approach ^{14}N ESEEM signal is normalized by the ^{1}H ESEEM signal as the ^{1}H ESEEM modulation depth is not affected by a replacement of ^{14}N with ^{15}N. The decrease in the relative modulation depth of the ^{14}N nuclear transition frequency can be calculated by comparing the relative integrated intensity of the ^{15}N labeled peptide with the non-labeled peptide. For a single ^{14}N nuclei coupled to an electron spin system, this decrease in modulation depth is,[38]

$$\frac{K^{\alpha}_{14(labeled)}/K_{1(labeled)}}{K^{\alpha}_{14(non\ labeled)}/K_{1(non\ labeled)}} = \frac{(1-f)\left[2-\left(K^{\alpha}_{14}+K^{\beta}_{14}\right)\right]}{2-(1-f)\left(K^{\alpha}_{14}+K^{\beta}_{14}\right)} \qquad [3]$$

Where, K is the modulation depth, and f is the fraction of ^{14}N nucleus that has been replaced. Subscripts 14 and 1 denote the ^{14}N spin and ^{1}H spin, respectively. Subscripts α and β represent the α and β spin manifolds of the electron spin, respectively. Shin and Saxena showed that this normalized ^{14}N modulation depth is a monotonic function of the fraction of ^{14}N that is replaced with ^{15}N.[38] It is evident that the decrease in the relative modulation depth of the ^{14}N nuclear transition frequency is greater than that in the fraction of ^{14}N. If K^{α}_{14} and K^{β}_{14} are much smaller than 1, the factor converges to$(1-f)$, which is the fraction of ^{14}N. For example if the K^{α}_{14} and K^{β}_{14} values are approximately 0.15 eq [3] becomes,

$$\frac{K_{14(labeled)}/K_{1(labeled)}}{K_{14(non\ labeled)}/K_{1(non\ labeled)}} = \frac{1.70(1-f)}{1.70+0.30f} \qquad [4]$$

In the case of a 33% replacement of ^{14}N with ^{15}N, the ratio $F(m^{15}N/0^{15}N)$ is approximately 0.63, which indicates that the relative modulation depth of the ^{14}N transition frequency decreases by 37%, just 4% greater than the expected from the fraction of replacement.

However, it is difficult to obtain modulation depths as many components are overlaid in the ESEEM time domain curve. Shin and Saxena showed that the integrated intensity can be used to account for the decrease in the modulation depth upon ^{15}N labeling, in the ^{14}N ESEEM signal.[38] In the frequency domain the ^{1}H signal is well separated from the signal produced by ^{14}N so it is possible to integrate each separately. The ^{14}N ESEEM integrated intensity is obtained by integrating between 0–8 MHz, and for the^{1}H ESEEM the integration is done between 10–14 MHz. Thus relative integrated intensities can be used to calculate the fraction of ^{14}N nuclei coordinated to Cu(II). Detailed equations for multiple histidine coordination are provided in reference 38.[38]

3.3 RESULTS

Zn(II) Competes with Cu(II) for Aβ(1−16) Coordination

Continuous-wave ESR experiments were carried out on the equimolar mixture of Cu(II) and Aβ(1−16) in the presence and absence of Zn(II) in 100 mM NEM (pH 7.4) buffer. These experiments were performed to demonstrate the binding competition between Cu(II) and Zn(II) for Aβ(1−16) coordination. As Zn(II) is a diamagnetic ESR silent species, the change in the Cu(II) signal is used to investigate the effects of Zn(II) in the system. At the physiological pH in NEM buffer, free Cu(II) precipitates and does not contribute to the signal.[81] Figure 3-2 shows the experimentally obtained CW-ESR spectra in the presence and absence of Zn(II). In the presence of 1 equiv of Zn(II), the intensity of the ESR signal decreased as shown in Figure 3-2. Quantitatively the double-integrated intensity was reduced by ∼25%. Upon the addition of 4 equiv of Zn(II), the double-integrated signal intensity of Cu(II) was decreased by ∼40%. The decrease in the double-integrated intensity of the Cu(II) signal clearly illustrates the fact that Zn(II)

competes with Cu(II) for Aβ(1−16) coordination. To understand how the Cu(II) signal intensity changes with the increase in Zn(II) concentration, further CW experiments were carried out. The ratios of Aβ(1−16) and Cu(II) were kept constant, and the Zn(II) ratio was changed from 0 to 10 in these experiments. The double-integrated intensity of these CW spectra was calculated to elucidate the amount of Cu(II) bound to the peptide at different Zn(II) ratios as shown in Figure 3-3. The amount of bound Cu(II) remains approximately constant after the addition of 4 equiv of Zn(II) to the mixture. Approximately 60% of the initially added Cu(II) is still bound to Aβ(1−16) even at large excess concentrations of Zn(II) under conditions where both metal ions compete simultaneously for peptide coordination.

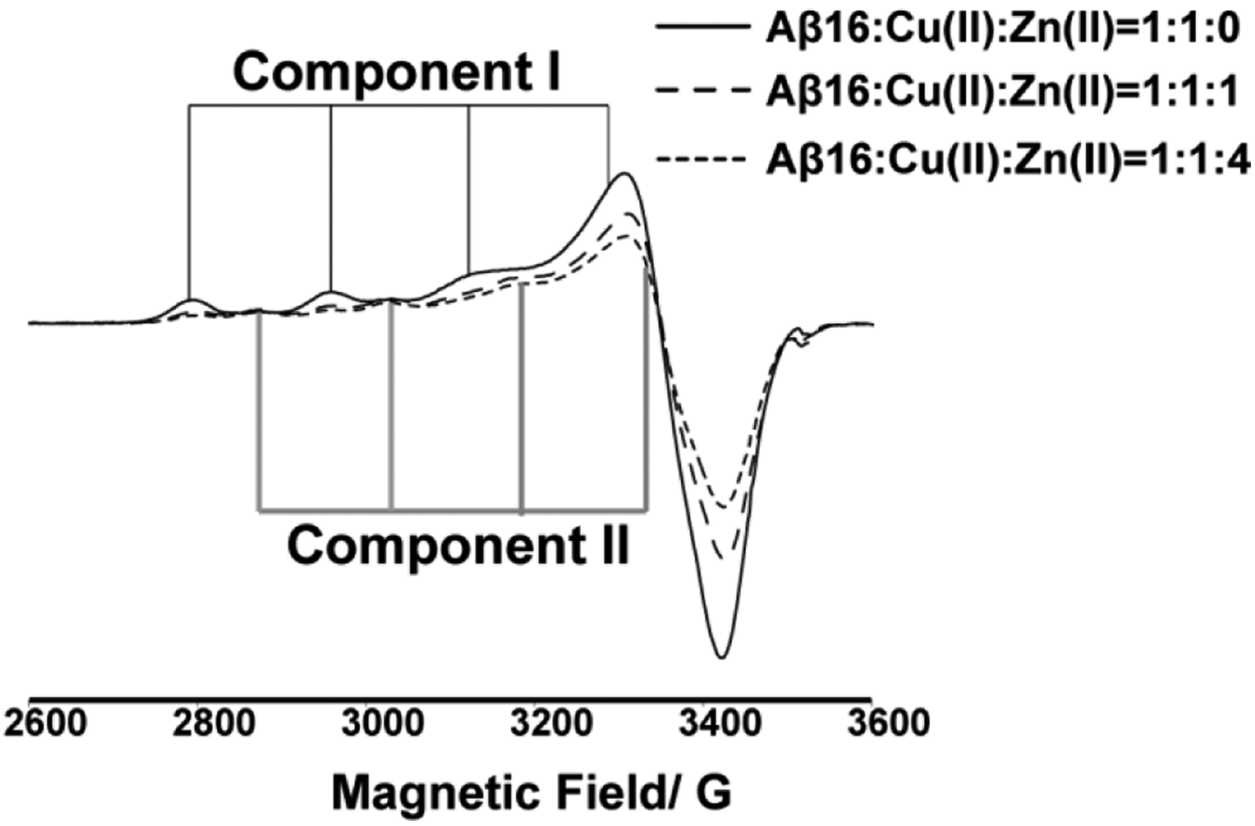

Figure 3-2 CW-ESR spectra illustrating the reduction of Cu(II) intensity in the presence of Zn(II) when coordinated to Aβ(1–16) peptide at physiological pH. At equimolar amount, Zn(II) reduces the double integrated intensity of Cu(II) signal by ~ 25 % with respect to the no Zn(II) spectra, and at four equivalents of Zn(II) the signal intensity is reduced by ~ 40 %.

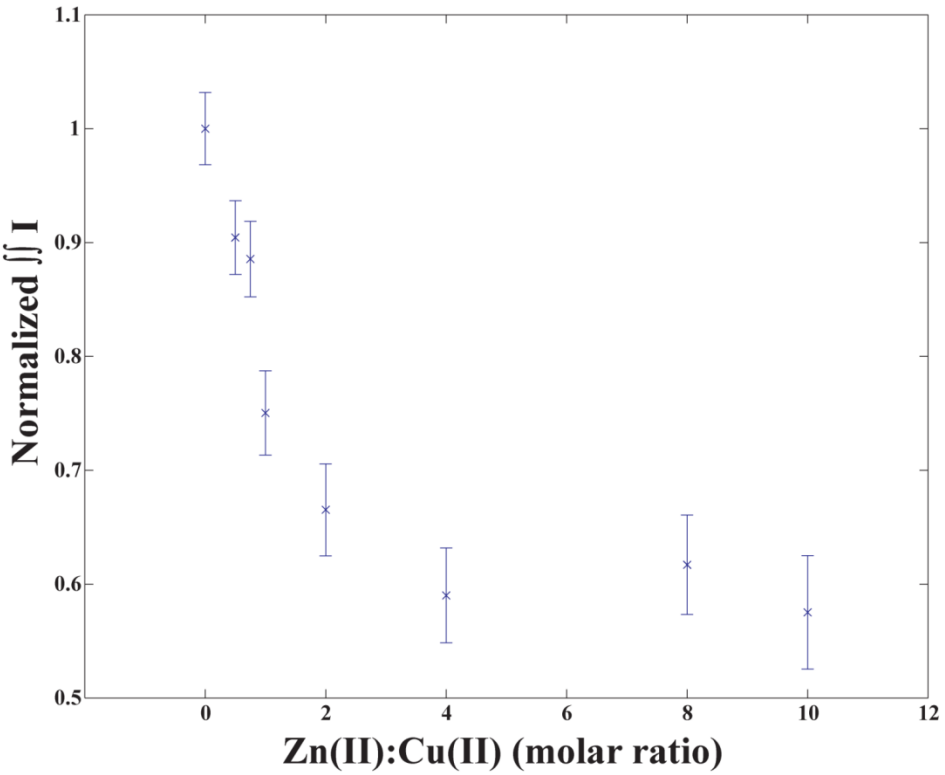

Figure 3-3 Double integrated intensity of Cu(II) signal of Aβ(1–16)-Cu(II)/Zn(II) ternary complex at different equivalents of Zn(II) added at pH 7.4

Zn(II) Competes Only with Component I of Cu(II) at Physiological pH

The Aβ(1−16)-Cu(II) CW spectrum contains two clear components at physiological pH (Figure 3-2). Component I, which is the major component of Cu(II) coordination at physiological pH, has $g_{\parallel}$ and $A_{\parallel}$ values of 2.26 ± 0.005 and 170 ± 1 G, respectively. These ESR parameters are consistent with a type II Cu(II) center, coordinated to three nitrogen ligands and one oxygen ligand in the equatorial plane.[19] Likewise, the $g_{\parallel}$ and $A_{\parallel}$ values of 2.23 ± 0.005 and 156 ± 1 G, respectively, of component II are consistent with coordination of either three nitrogen ligands and one oxygen ligand or four nitrogen ligands.[19]

A close inspection of CW-ESR spectra of Aβ(1−16)-Cu(II) and Aβ(1−16)-Cu(II)/Zn(II) showed an interesting pattern. Figure 3-4a shows the CW-ESR spectra of Aβ(1−16)-Cu(II) and Aβ(1−16)-Cu(II)/Zn(II) complexes at pH 7.4. Interestingly, in the presence of Zn(II) the intensity of only component I was decreased. The intensity of component II remains very similar in both the presence and the absence of Zn(II). Spectral simulations were performed to quantify the proportion of each component in the Aβ(1−16)-Cu(II) complex. ESR parameters used for the CW simulations are tabulated in the Table 3-1. An overlay of experimental and simulation results is shown in, Figure 3-5. In the absence of Zn(II), component I was the major component and account s for ∼65% of the overall signal. However, in the Aβ(1−16)-Cu(II)/Zn(II) equimolar complex the amount of component I is ∼53%. At a 4-fold excess of Zn(II), the proportion of component I is ∼35%. To confirm the selective substitution of Cu(II) by Zn(II), experiments were repeated at pH 8.7. At this pH, only component II of Cu(II) binding is present. The double-integrated intensity of the Cu(II) signal in the presence and absence of 1 equiv of Zn(II) remained approximately the same, as shown in Figure 3-4b, indicating that Zn(II) was unable to displace Cu(II) from component II.

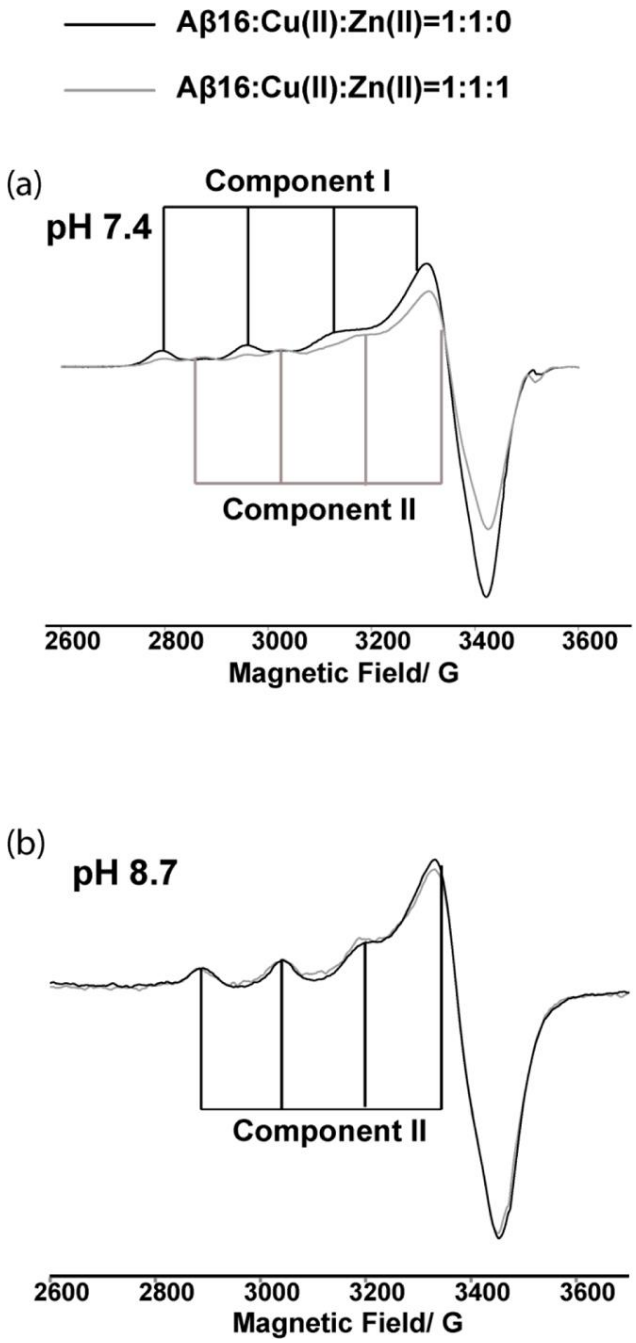

Figure 3-4 (a) Overlay of CW-ESR spectra of Aβ(1−16)-Cu(II) equimolar binary complex (black) and Aβ(1−16)-Cu(II)/Zn(II) equimolar ternary complex (gray) at pH 7.4 and (b) at pH 8.7. At pH 8.7, only component II of Cu(II) binding is present. Interestingly, the double-integrated intensity of the spectra remains almost the same, suggesting Zn(II) cannot compete with Cu(II) for component II coordination.

Table 3-1 Relative proportions of Aβ(1–16)-Cu(II) component I and II at different equivalents of Zn(II) added at pH 7.4.

Equivalents of Zn(II) added	**Component I %**	**Component II %**
0	65	35
0.5	58	42
0.75	56	44
1	53	47
2	40	60
4	35	65
8	31	61

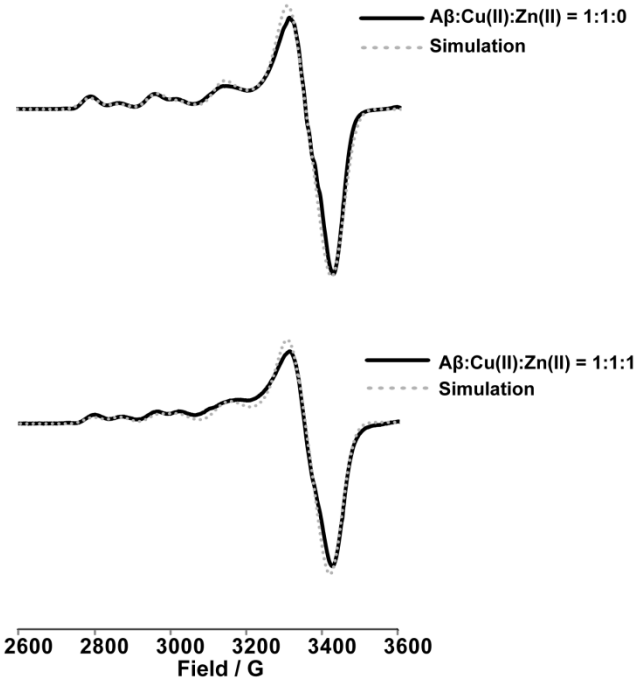

Figure 3-5 Simulated CW spectra for Aβ(1–16)-Cu(II) binary complex and Aβ(1–16)-Cu(II)/Zn(II) ternary complex. Experimental spectra are shown in solid lines and simulated ones are shown in dashed.

Contribution of Each Histidine Residue for Component I in Aβ(1−16)-Cu(II)/Zn(II) Complex

As discussed earlier, all three histidine residues are involved in the Cu(II) coordination at physiological pH[34, 83, 91]and component I consists of three subcomponents (Figure 1).[38] Our CW results show that Zn(II) competes only with Cu(II) for component I coordination. Thus, it is of interest to discover which subcomponents of component I compete with Zn(II) for Aβ(1−16) coordination by evaluating the contribution of each histidine residue to the Cu(II) coordination in component I. Experiments are carried out at a magnetic field strength of 2800 G, where the contribution from component II is negligible.

Figure 3-6 shows the ESEEM spectrum of unlabeled Aβ(1−16) peptide coordinated to Cu(II) and Zn(II) at physiological pH and 2800 G. The spectrum contains three peaks around 0.55, 1.01, and 1.54 MHz. The nuclear quadrupole parameters, e^2qQ/h and η, are determined to be 1.70 ± 0.03 MHz and 0.65 ± 0.02, respectively. These numbers are comparable to those for Cu(II) histidine complexes.[27-30] The broad peak around 3.8 MHz is due to a double quantum (DQ) transition of the remote nitrogen of the imidazole.[24, 41] As two histidine residues are likely simultaneously coordinated to Cu(II) on the equatorial plane, two simultaneous histidine coordinations are assumed to yield the best fit for ESEEM simulation (Figure 3-6). Apart from the peaks arising from ^{14}N, there is another peak around 11.9 MHz which is similar to the ^{1}H Larmor frequency at 2800 G. This peak is a result of hydrogen atom(s) weakly interacting with the electron spin of Cu(II).

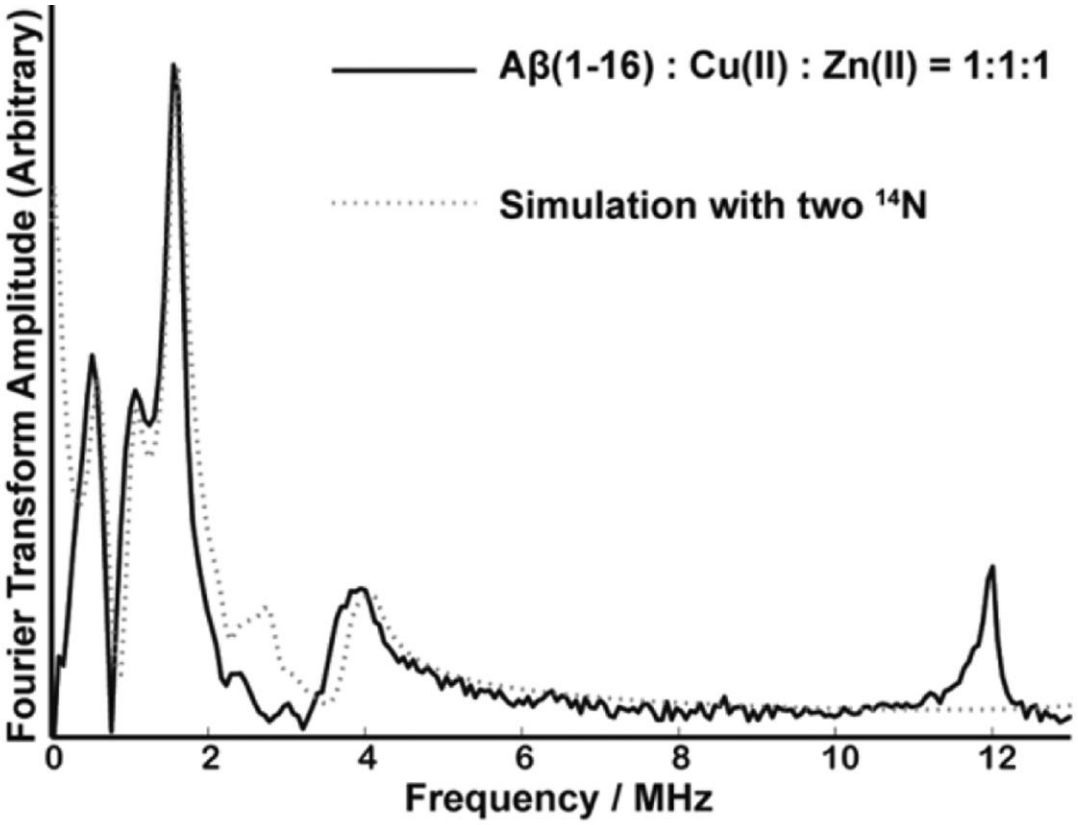

Figure 3-6 Experimentally obtained and simulated three-pulse ESEEM spectra of the nonlabeled Aβ(1−16) peptide mixed with equimolar amounts of Cu(II) and Zn(II) at 2800 G and pH 7.4.

Next, we analyzed the three-pulse ESEEM spectra obtained for three singly labeled Aβ(1−16) peptide variants. The spectra are shown in Figure 3-7. In these peptides, a single histidine at either His 6, His 13, or His 14 is isotopically labeled with ^{15}N. All these Aβ(1−16) variants were mixed with equivalent amounts of Cu(II) and Zn(II) at pH 7.4. The four spectra have similar line shapes and peak positions in the ^{14}N-ESEEM region. The similarity in the peak shapes implies that the ESEEM active ^{14}N of each histidine residue has almost the same nuclear transition frequencies.[30] In ESEEM experiments, the ^{14}N-ESEEM intensity is related to the number of ^{14}N histidine residues coordinated to Cu(II) (see Experimental Section). The single-quantum transition of ^{15}N, a nucleus with a spin of 1/2, contributes minimally (∼2%) toward the ESEEM signal.[31, 39] Hence, when a ^{14}N nucleus is replaced with a ^{15}N the ESEEM signal intensity will decrease.

The three-pulse ESEEM spectra of three single-labeled peptides and the wild type were normalized using their ^{1}H-ESEEM intensities at or around 11.9 MHz. Then the ESEEM spectra were integrated between 0 and 8 MHz and compared between the wild-type and the ^{15}N-labeled peptides (see Experimental Section). As Figure 3-7 illustrates, the ^{15}N-labeled variants have lower intensities in the ^{14}N region below 8 MHz. At physiological pH, the normalized ^{14}N-ESEEM intensity of His 14-labeled peptide decreased by approximately 50% compared to that of the unlabeled ternary complex (Aβ(1−16)H14[^{15}N] in Figure 3-7). The decrease in ^{14}N-ESEEM intensity indicates that ∼50% of the peptides in the ensemble use His 14 as an equatorial ligand in Cu(II) coordination. The reductions of ^{14}N-ESEEM intensity for His 6- and His 13-labeled samples were ∼20% (Aβ(1−16)H6[^{15}N] in Figure 3-7) and 30% (Aβ(1−16)H13[^{15}N] in Figure 3-7), respectively. These values suggest that ∼20% and ∼30% of the peptides in the mixture equatorially coordinate to Cu(II) through His 6 and His 13, respectively. Hence, His 14 becomes the most significant equatorially coordinated histidine ligand in Cu(II) binding (∼50%) in component I. In

the Aβ(1−16)-Cu(II) binary complex, both His 6 and His 14 were equally important in Cu(II) binding, each accounting for ∼40%.26 Thus, the Cu(II) coordination environment is rearranged in the presence of Zn(II).

The same set of experiments was carried out using three double-labeled Aβ(1−16) variants. In these double-labeled peptides, two out of three histidine residues in Aβ(1−16) are isotopically labeled with ^{15}N. As two of the three histidine residues are labeled, ^{14}N-ESEEM signal intensity results only from the nonlabeled histidine. This provides a direct methodology for determining the extent to which each of these residues is involved in the ternary complex. All the experiments were carried out at 2800 G, where only component I is present.

Despite a low signal-to-noise ratio, because of the fact that only one histidine is responsible for the ^{14}N-ESEEM signal, we were able to do the analysis with extensive signal averaging. As shown in Figure 3-8, as expected, His 14 was the highest contributing highest contributing histidine ligand in Cu(II) coordination in the ternary complex. The ESEEM signal intensity of His 6- and His 13-labeled peptide (in which only His 14 gives rise to the signal) is approximately 50% of that of the nonlabeled peptide (Aβ(1−16)H6,13[^{15}N] in Figure 3-8). This signal intensity indicates that ∼50% of the peptides in the mixture use His 14 as an equatorial ligand. The ESEEM signal intensities of Aβ(1−16)H6,13[^{15}N] (His 6 nonlabeled) and Aβ(1−16)H6,13[^{15}N] (His 13 nonlabeled) were ∼20% and ∼30%, respectively. Hence, the percentages of each histidine residue involved as an equatorial ligand in Cu(II), obtained from both single- and double-labeled peptides, were similar. The integrated intensities of each spectrum and the relative contributions from each histidine residue toward the ^{14}N-ESEEM signal are tabulated in the, Tables 3-2 and 3-3.

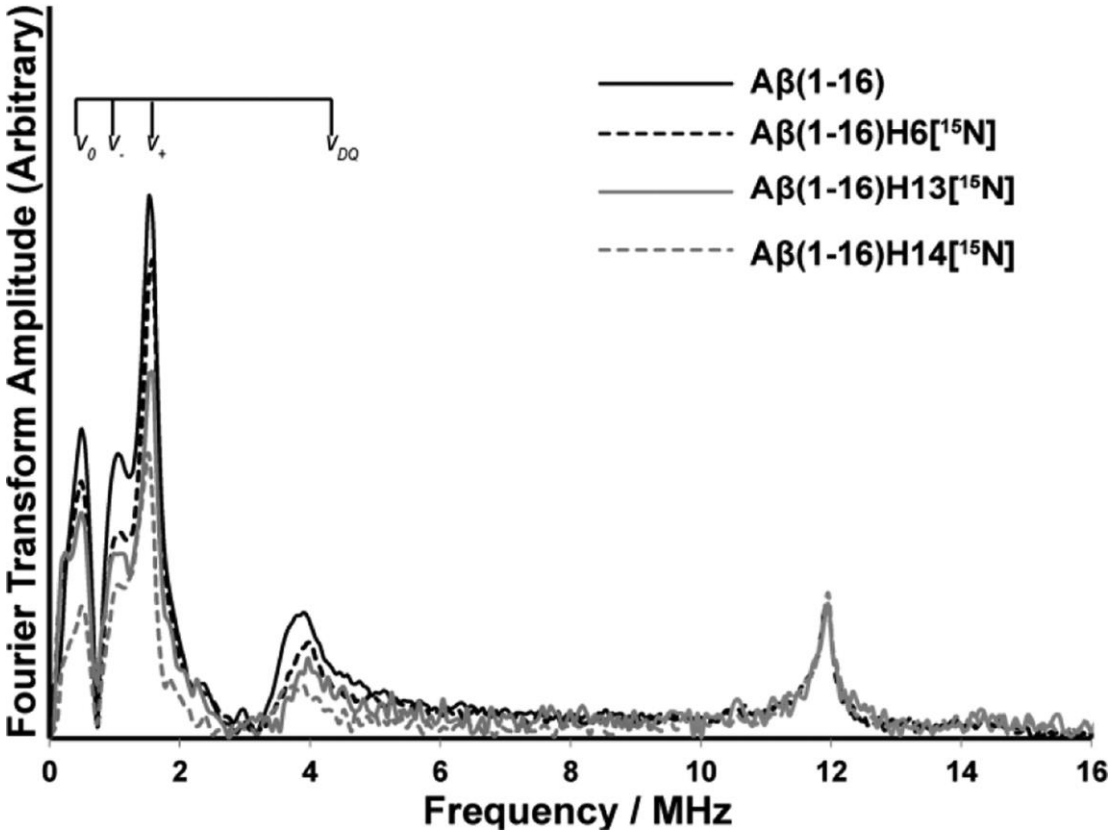

Figure 3-7 Three-pulse ESEEM spectra of the nonlabeled and single-^{15}N-labeled Aβ(1−16) variants mixed with equimolar amounts of Cu(II) and Zn(II) at 2800 G and pH 7.4 (peptide:Cu(II):Zn(II) = 1:1:1). The decrease in intensity below 8 MHz in ^{15}N-labeled Aβ(1−16) variants gives the contribution of each histidine residue for component I in the Aβ(1−16)-Cu(II)/Zn(II) complex. Aβ(1−16)H6[^{15}N], Aβ(1−16)H13[^{15}N], and Aβ(1−16)H14[^{15}N] denote peptides in which His 6, His 13, and His 14 are labeled with ^{15}N, respectively.

Table 3-2 Relative integrated intensities of ESEEM spectra of the nonlabeled and ^{15}N- single labeled Aβ(1–16) variants at pH 7.4 mixed with equimolar amounts of Cu(II) and Zn(II) at the ^{14}N-ESEEM region (0–8 MHz) and ^{1}H-ESEEM region (10–14 MHz) and the relative contribution from each histidine residue.

Sample	**^{14}N-ESEEM**	**^{1}H-ESEEM**	**$^{14}N/^{1}H$**	**% reduction**
Aβ	1400 ± 4	240 ± 3	5.83 ± 0.07	
His 6	1153 ± 4	237 ± 3	4.86 ± 0.06	16.6 ± 1.6
His 13	981 ± 7	236 ± 5	4.16 ± 0.09	28.6 ± 2.0
His 14	637 ± 5	237 ± 3	2.69 ± 0.04	53.8 ± 1.5

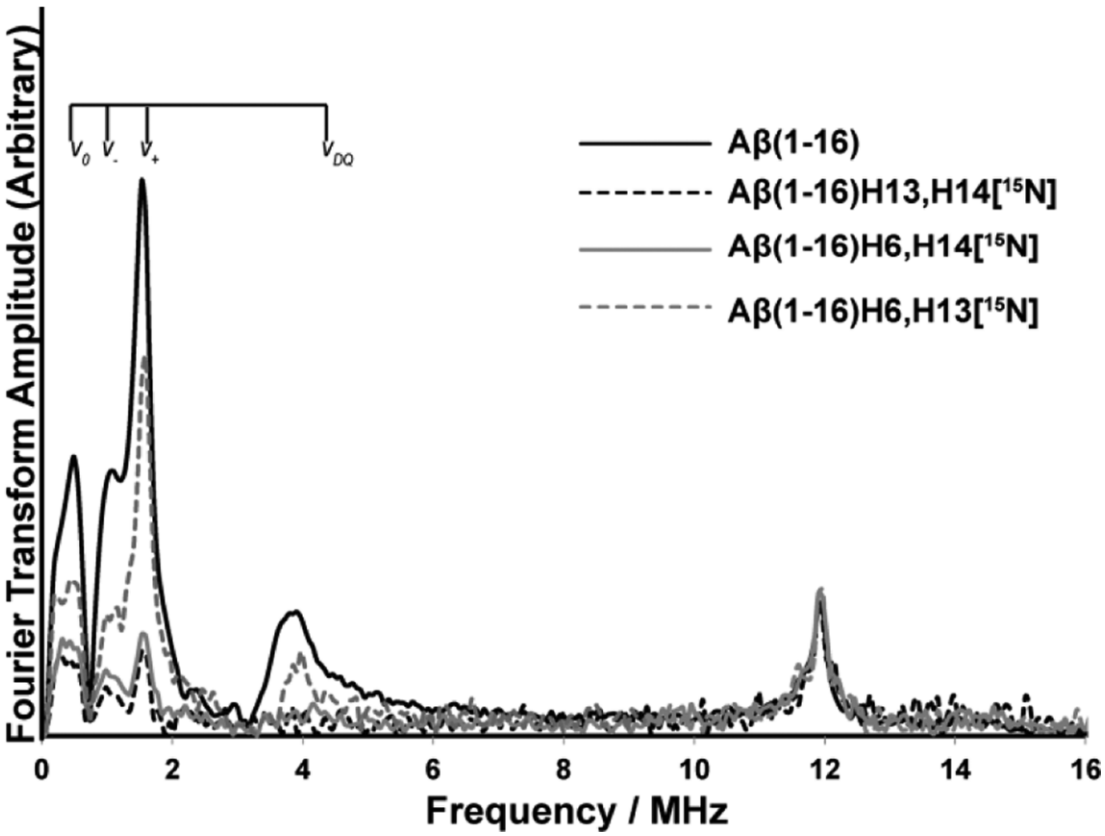

Figure 3-8 Three-pulse ESEEM spectra of the nonlabeled and double ^{15}N labeled Aβ(1–16) variants mixed with equimolar amounts of Cu(II) and Zn(II) at 2800 G at pH 7.4. Integrated area between 0 – 8 MHz gives the contribution of the nonlabeled histidine residue in double labeled Aβ(1–16) variants for component I in Aβ(1–16)-Cu(II)/Zn(II) complex. Aβ(1–16)H13,14[^{15}N], Aβ(1–16)H6,14[^{15}N], Aβ(1–16)H6,13[^{15}N] denote peptides where His 13/14, His 6/14, and His 6/13 are labeled with ^{15}N, respectively.

Table 3-3 Relative integrated intensities of ESEEM spectra of the nonlabeled and ^{15}N- double labeled Aβ(1–16) variants at pH 7.4 mixed with equimolar amounts of Cu(II) and Zn(II) at the ^{14}N-ESEEM region (0–8 MHz) and ^{1}H-ESEEM region (10–14 MHz) and the relative contribution from each histidine residue.

Sample	**^{14}N-ESEEM**	**^{1}H-ESEEM**	**$^{14}N/^{1}H$**	**% involvement**
Aβ	1400 ± 4	240 ± 3	5.83 ± 0.07	
His 6,13 (His 14)	720 ± 7	229 ± 5	3.14 ± 0.08	53.9 ± 1.5
His 6,14 (His 13)	382 ± 6	240 ± 5	1.59 ± 0.05	27.2 ± 1.0
His 13,14 (His 6)	316 ± 10	247 ± 7	1.28 ± 0.05	21.9 ± 1.2

The integrated intensity of the DQ peak depends on the number of ^{14}N-ESEEM active histidine residues.[29] Hence, the double quantum signal was weak in the double-labeled peptides as only one ^{14}N-ESEEM active histidine residue is present. Comparison between the single- and double-labeled peptide showed that the DQ integrated intensity is greater in the single labeled peptide. If there is just single-histidine coordination, the DQ intensity would remain similar between the single- and double-labeled peptides. Therefore, the simultaneous coordination of two histidine residues in component I of the Aβ(1−16)-Cu(II)/Zn(II) ternary complex is preserved as it is in the Aβ(1−16)-Cu(II) binary complex.[34, 38, 91]

HYSCORE experiments were carried out in nonlabeled and labeled Aβ(1−16)-Cu(II)/Zn(II) at physiological pH and at the magnetic field of 3360 G. The spectra obtained showed the same frequency patterns as in the Cu(II) complex,[38, 83] indicating that despite the presence of Zn(II), the coordination of Cu(II) remains essentially unchanged as shown in Figure 2-9. The primary difference between the two sets of spectra was that the intensities of correlation peaks were reduced as Zn(II) replaced approximately 25% of bound Cu(II) at equimolar amounts.

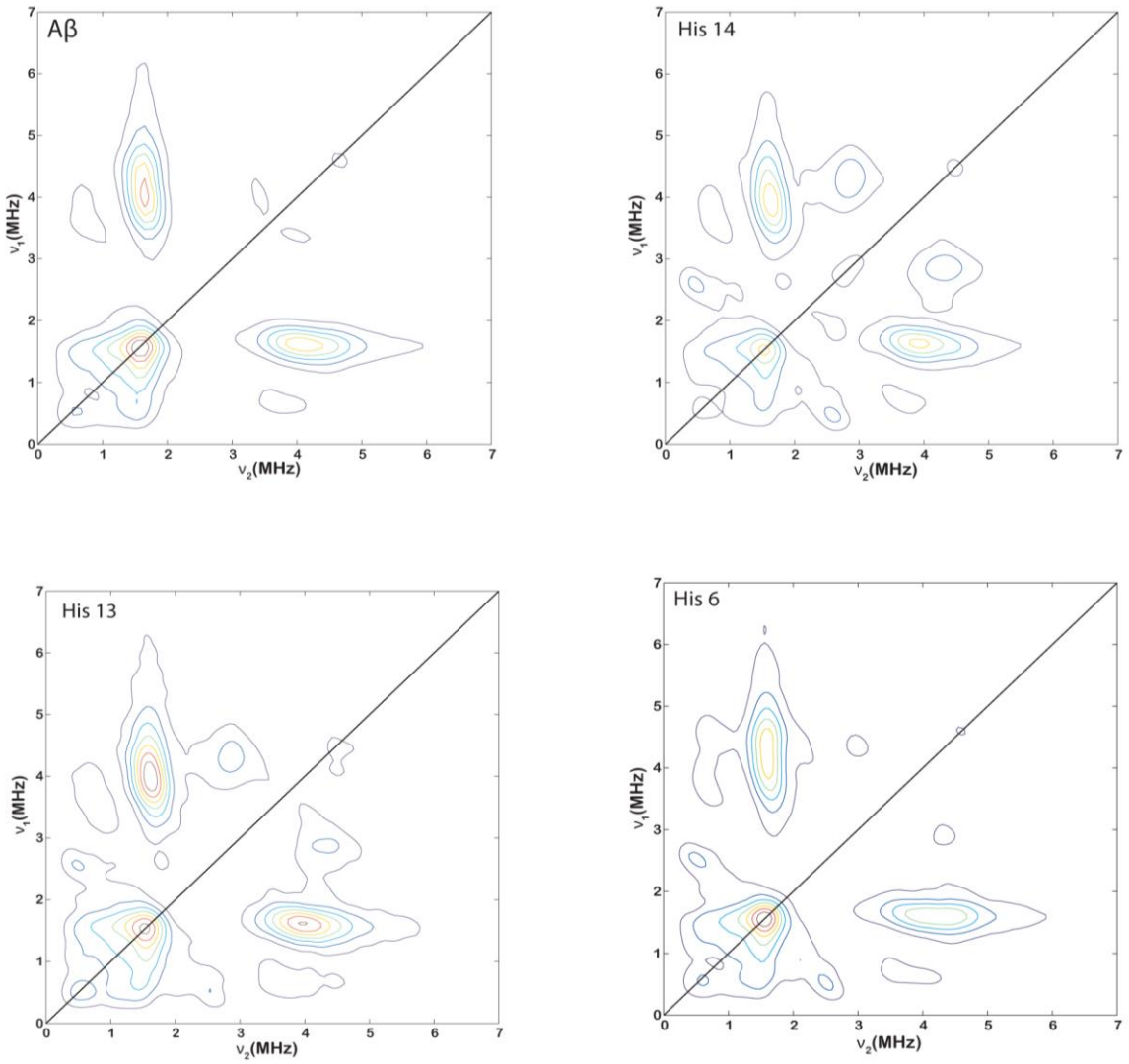

Figure 3-9 ^{14}N and ^{15}N-ESEEM regions of the HYSCORE spectra of the nonlabeled and ^{15}N labeled Aβ(1 – 16) variants mixed with equimolar amounts of Cu(II) and Zn(II) at 3360 G at pH 7.4. Peak shapes and positions remain constant between the binary Aβ(1–16)-Cu(II) and Aβ(1–16)-Cu(II)/Zn(II) ternary complex. The cross peak around 1.8 MHz, 8.0 MHz is not visible in the ternary complex as the signal intensity is decreased ~ 25 % due to Zn(II) substitution.

3.4 DISCUSSION

Selective Zn(II) Competition for Component I Cu(II) Coordination

Much work has been performed to determine the coordination environments and aggregate forms of Aβ in the presence of metal ions such as Cu(II) and Zn(II). However, multiple metal ion interactions in Aβ are not well-understood. The changes in Cu(II) coordination modes in the presence of Zn(II) in prion protein were examined using CW-ESR[73] and X-ray absorption spectroscopy (XAS).[76] These results in Aβ(1−16) show the usefulness of ESEEM to elucidate molecular level details of metal ion competition and coordination. These kinds of experiments are important as multiple metal ions coexist in an in vivo environment. Using CW-ESR and spectral simulations we established that Zn(II) competes only with component I at physiological pH. Our CW-ESR and simulations revealed that at excess amounts of Zn(II), component II becomes the most significant coordination mode. In brain tissues affected with Alzheimer's disease, the concentration of zinc is higher than that of copper.[5] Hence, it will be critical to understand the microscopic details of component II coordination.

Change in Component I Cu(II) Coordination in Aβ(1−16) in the Presence of Zn(II)

The ESEEM results show that at physiological pH proportions of peptides coordinated through histidine residues in the equatorial plane are in the order His 14 > His 13 > His 6. These contributions are significantly different from the contributions reported for component I in the Cu(II)-Aβ(1−16) binary complex. Previous work done in our group reported that the order for the binary complex was His 14 ~ His 6 > His 13.[38] This is the first investigation reporting the contributions of each histidine residue in the Aβ(1−16)-Cu(II)/Zn(II) ternary complex. These results suggest the importance of His 14 in Cu(II) coordination in the presence of Zn(II).

Damante et al.,[131] in their work done using the Aβ(1−16)-polyethylene glycol-ylated peptide, suggested that the addition of Zn(II) does not liberate Cu(II) ions but modifies the metal ion distribution in Aβ(1−16). Also Alies et. al.; recently showed that Zn(II) ions shift Cu(II) coordination toward component II coordination.[94] In our findings, Zn(II) can partially substitute (∼25%) bound Cu(II) from Aβ(1−16) at equimolar concentrations. Also, the present work adds critical details regarding the redistribution of Cu(II). Using the proportions of each histidine residue involved in Aβ(1−16)-Cu(II), the proportion of peptides in each component was calculated.[38] Figure 3-10 shows the overall coordination environment of Cu(II) in Aβ(1−16) in the presence and absence of 1 equiv of Zn(II). Notably, all the Cu(II) ions in subcomponent IA, in which the metal ion is simultaneously coordinated to His 6 and His 13, are replaced by Zn(II). The proportion of Cu(II) coordinated peptides in subcomponent IB is decreased, while the number of peptides in subcomponent IC is increased. These observations can be rationalized using the individual affinities of histidine residues toward Cu(II). The affinity of each histidine residue is in the order His 14 > His 13 ∼ His 6.[38] This order would suggest Zn(II) is more likely to remove Cu(II) coordinated to His 6 and His 13 than it is to remove Cu(II) coordinated to His 14. Hence, Zn(II) is most likely to substitute Cu(II) in subcomponent IA.

Information on Cu(II) and Zn(II) coordination in Aβ will help establish the conformational preferences and structure of the N-terminus. This insight is crucial because current models of structure do not include any metal ions. Furthermore, these results are also likely to guide rational structure-based design of metal chelates as therapeutics for Alzheimer's disease.[132-134]

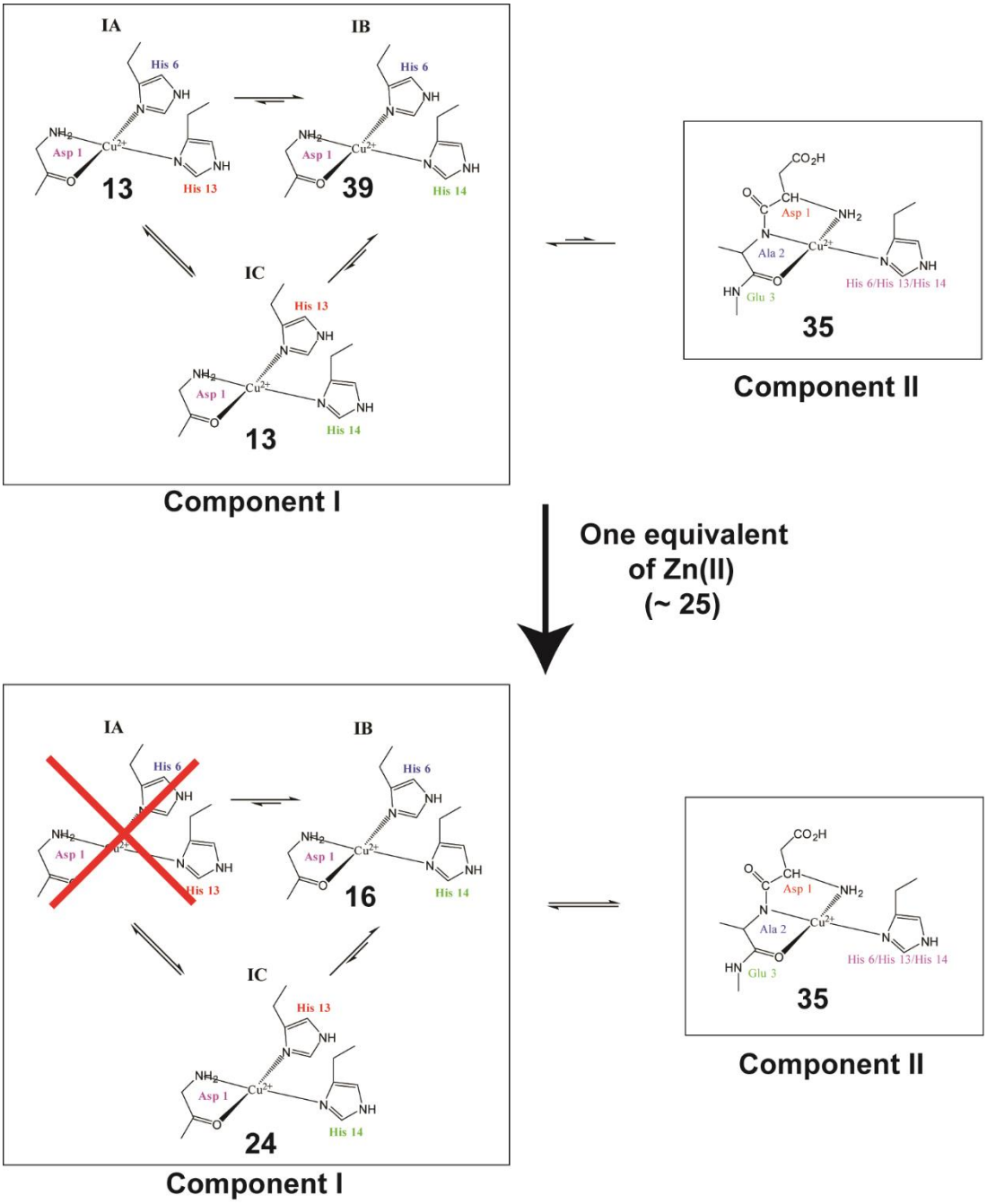

Figure 3-10 Overall population distribution of Cu(II) binding modes in Aβ(1–16) in the presence and the absence of Zn(II) at physiological pH. The proportion of Subcomponent IC, which may inhibit the formation of ordered fibrillar forms, is increased.[38] Subcomponent IA is no longer present in the presence of Zn(II) and IB proportion is decreased.

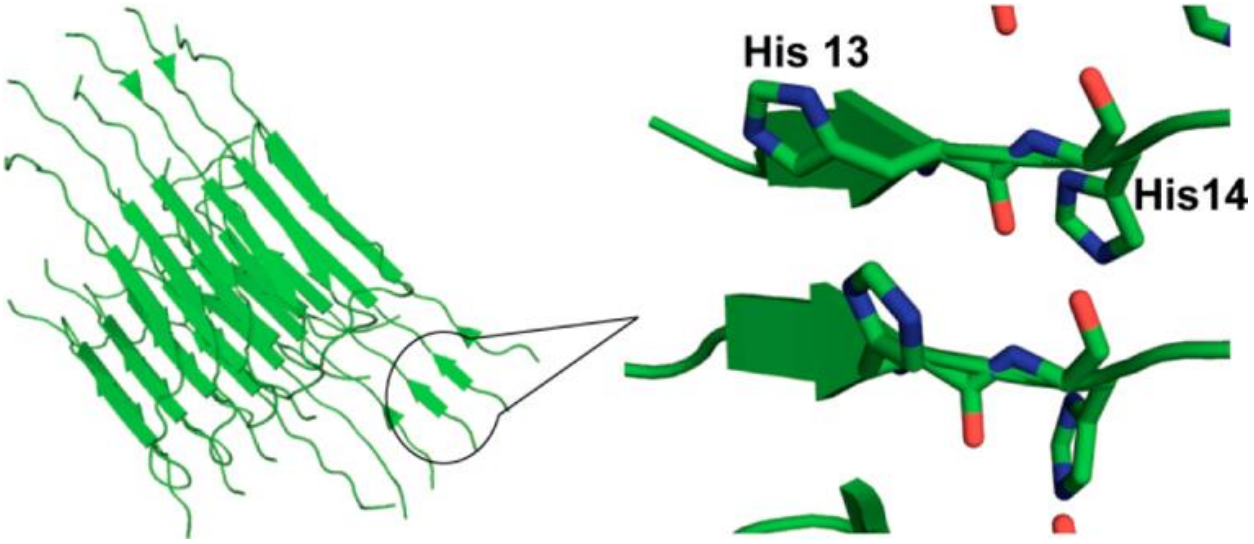

Figure 3-11 Location of His 13 and His 14 in the fibrillar structure of Aβ(1–40). (PDB ID : 2LMN).

Physiological Importance of Simultaneous His 13 and His 14 Coordination

It is known that at greater than equimolar concentrations the proportion of amorphous aggregates is greater than that of the ordered fibrillar aggregates.[4] Previously, we had proposed that simultaneous His 13-His 14 coordination (subcomponent IC) might be the genesis of this effect. Simultaneous coordination of His 13 and His 14 to Cu(II) is expected to prevent the formation of ordered β-sheet structures, as the side chains of the histidine residues would be forced to be on the same side (Figure 3-11). In the presence of Zn(II), the proportion of subcomponent IC increases. It has also been postulated that a salt bridge between His 13 and Asp 23 is important for the formation of a key intermediate toward the formation of ordered fibrils.[135-136] Zn(II) or Cu(II) coordination to His 13, even at very low concentrations, may disrupt the salt bridge, leading to the formation of disordered amorphous aggregates rather than ordered aggregates. We performed AFM imaging to test these hypotheses. In the presence of Zn(II), amyloid-β forms more amorphous aggregates. These AFM experiments were carried out using Aβ(1−40) (Figure 3-12), as this variant contains the hydrophobic region necessary for aggregation of the peptide, which is absent in Aβ(1−16). The trend observed is different when just Cu(II) is used as observed earlier (cf. Figure 2-1).[4] In general, when the metal ion concentration increases, the probability of forming fibrillar aggregates decreases. These results suggest that metal ion coordination to His 13 likely plays a decisive role in dictating the morphology of the aggregates. It would be fascinating to directly monitor the disruption of the His 13-Asp 23 salt bridge by solid state NMR.[137]

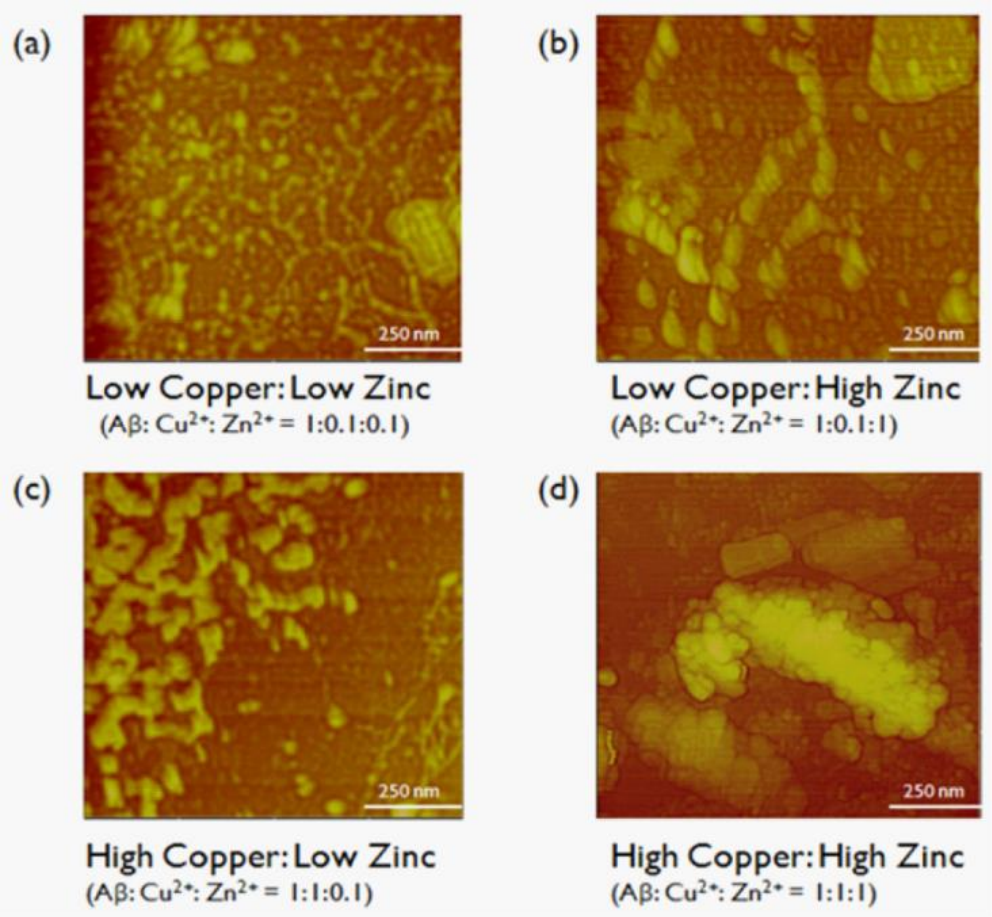

Figure 3-12 Morphology of Aβ(1–40) aggregates formed under (a) low Cu(II): low Zn(II), (b) low Cu(II): high Zn(II), (c) high Cu(II): low Zn(II), (d) high Cu(II): high Zn(II). All samples were incubated along with metal ions at 37° C. In the presence of Zn(II) the probability of forming amorphous aggregates is favored.

3.5 SUMMARY

We used the well-known metal-binding peptide Aβ, which is involved in Alzheimer's disease, to study the metal-binding competition between Cu(II) and Zn(II). The two metal ions, Cu(II) and Zn(II), have different affinities toward Aβ(1−16), and even at large excess of Zn(II), ∼60% of Cu(II) is still bound to Aβ(1−16). Interestingly, Zn(II) was able to replace only Cu(II) coordinated in component I, while component II bound Cu(II) resisted the Zn(II) substitution. Subcomponent IC in which His 13 and His 14 are equatorially coordinated to a Cu(II) ion becomes the most significant coordination mode. This is a very interesting observation as subcomponent IC might be responsible for the formation of amorphous aggregates. This work shows the ability of ESEEM measurements to provide molecular level information of metal ion coordination and competition. Such molecular level details of metal ion coordination may ultimately pave the way to understanding the formation of aggregates of different morphologies and the toxicity associated with Alzheimer's disease.

3.6 ACKNOWLEDGEMENTS

This work was supported by a National Institutes of Health grant (5R01NS053788), and a National Science Foundation (MCB 1157712) grant. The Bruker ElexSys E680 was purchased from the funds from National Institutes of Health grant 1S10RR028701. We are grateful to the peptide synthesis facility at University of Pittsburgh, for peptide preparation. We also thank Dr. Byong-kyu Shin and Brian Michael for helpful discussions.

4.0 ORIGINS OF STRUCTURAL FLEXIBILITY IN PROTEIN-BASED SUPRAMOLECULAR POLYMERS REVEALED BY DEER SPECTROSCOPY

Part of this work is written in collaboration with Nathan A. Tavenor, Sunil Saxena, and W. Seth Horne and has been published in the Journal of Physical Chemistry B, 2014, V. 118, 9881-9889. Author contributions: W.S.H. and S.S. designed research; N.A.T synthesized the peptides, K.I.S performed DEER measurements, K.I.S and S.S analyzed DEER data, W.S.H resolved the X-ray structure, N.A.T performed MD simulations, N.A.T, K.I.S, S.S and W.S.H wrote the paper

4.1 INTRODUCTION

Coiled coils are α-helical folding[138] motifs found in ~ 10% of eukaryotic proteins.[139] These structures are formed when two or more sequences, that demonstrate heptad signatures, coil around each other in a very specific manner.[140] These complexes are highly stable in aqueous environments. Unique characteristics of coiled coil assemblies such as oligomerization state,[141] size,[142-143] stability[144] and direction of binding[145-147] can be modulated by the careful selection of the sequence.[148-149] The noncovalent association of the coiled coils is sensitive to external parameters such as temperature, ionic strength, pH and choice of solvent, which affects both electrostatic and hydrophobic interactions.[150-153] Hence, coiled coils have become useful for the programmed self-assembly of supramolecular polymer materials.

Supramolecular polymers are a class of materials constructed through noncovalent interactions such as metal ion coordination, hydrogen bonding, hydrophobic interactions and π-π

interactions.[154-158] They are dynamic reversible assemblies based on noncovalent interactions frequently found in nature.[159-160] The dynamic nature of these polymers make them sensitive to external stimuli, which makes them ideal candidates for the formation of smart materials. These materials can be used for applications such as analytical devices, organic electronics and regenerative devices.[161-164] An understanding of the molecular origins of the chain dynamics in these polymers is essential in developing smart materials.

Previous work done in the Horne lab has shown two coiled-coil forming peptides linked at their midpoints by an organic linker can lead into the formation of programmed supramolecular polymers.[8, 165] Two organic linkers used for these assemblies are shown in Figure 4-1.[8, 165] These linkers, based on either ethylenediamide (EDA) or piperazine (PIP), connect the two coiled coil peptides through a solvent exposed Cys residue. Despite being structurally similar to each other, these two linkers form supramolecular polymers with different physical properties. Primarily, the apparent hydrodynamic radius of the subunits formed with PIP linkers was larger than the subunits formed with EDA linkers.[8] This result suggests that the rigidity of the linkers plays an important role in controlling the structure of the polymers.

The critical point to understand in the above work is the role of linker flexibility in dictating the overall structure of the polymer. By the first principles, the more rigid linker PIP would lead to the formation of stiffer polymer structures. However, it is difficult to test this hypothesis. To explore different conformational distributions resulting from the linkers used we use double electron-electron resonance (DEER) spectroscopy experimentally. DEER spectroscopy is a pulsed electron spin resonance (ESR) technique that measures a distance between two paramagnetic centers. This method is capable of measuring distances ranging from 1.5 – 10 nm making it an ideal technique to probe protein based structures.[52, 166-168]

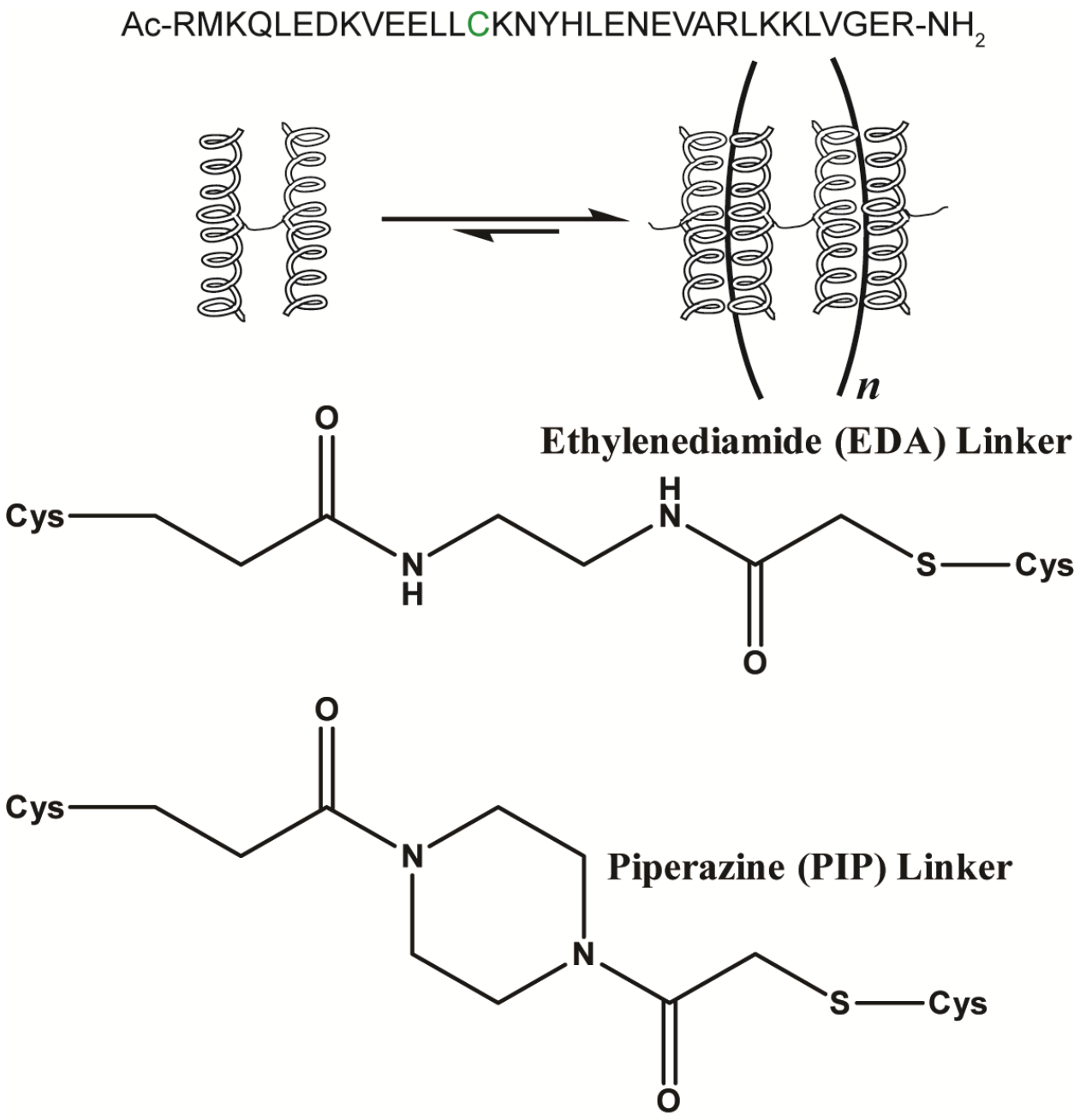

Figure 4-1 The sequence of the GCN4 peptide with the cross linking cysteine shown in green. A subunit building block of the coiled coil forming peptide linked with the linkers. The structures of the two organic linkers that connects the chains.

4.2 EXPERIMENTAL SECTION

Double Electron−Electron Resonance (DEER) Spectroscopy.

DEER experiments were performed on either a Bruker ElexSys E580 or a Bruker ElexSys E680 X-band FT/CW spectrometer equipped with a Bruker ER4118-MD5 or EN4118X-MD4 resonator, respectively. The sample temperature was regulated using an Oxford ITC503 temperature controller and an Oxford CLT650 low-loss transfer tube. For each measurement, ~150 μL of the appropriate sample was transferred into a 3 mm inner diameter quartz tube, flash frozen in liquefied methylacetylene-propadiene and propane (MAPP) gas, and inserted into a sample cavity precooled to 80 K. The four-pulse DEER experiments were carried out using a pulse sequence of $(\pi/2)\nu_1$-τ_1-$(\pi)\nu_1$-T-$(\pi)\nu_2$-τ_2-$(\pi)\nu_1$-τ_2-echo.[169] The pump frequency, ν_2 was set at the maximum of the nitroxide spectrum. The observer frequency, ν_1 was offset by ~70 MHz. The lengths of the $(\pi/2)\nu_1$ and $(\pi)\nu_1$ pulses were 16 and 32 ns, respectively. The $(\pi)\nu_2$ pulse was set to 16 ns. Step sizes of 8 and 16 ns were used to measure shorter and longer distances, respectively, for 128 data points. Deuterated solvent and glycerol-d8 were used to increase the phase memory time of the linker samples. Raw DEER data were analyzed using the DEERAnalysis 2013[63] software. Given the scope of the present work, where general features of the distance distributions were needed, we analyzed the data assuming a Gaussian distance distribution. Although model dependent, such fits improve the reliability of the analysis.[63] The use of Gaussian models also facilitates comparison of trends in closely related samples and minimizes artifacts arising from low signal-to-noise, which can complicate data interpretation.

Details of sample preparation, X-ray crystallography, circular dichroism spectroscopy and molecular dynamics aided modeling are given in reference **170**.[170]

4.3 RESULTS AND DISCUSSION

Selection of the spin label for DEER spectroscopy

After the synthesis of the helix forming peptide GCN4 as shown in Figure 4-1, our goal was to select the best spin label to use for distance measurements. The most widely used spin labels are based on a nitroxide functional group.[171-172] In expressed proteins the nitroxide functional group can be introduced via a covalent modification of a cysteine residue with a thiol-active reagent 1-oxyl-2,2,5,5-tetramethylpyrroline-3-methyl)methanethiosulfonate (MTSSL) (Figure 4-2).[173-175] For synthetic peptides the nitroxide group can also be introduced through an unnatural amino acid, such as 2,2,6,6-tetramethyl-N-oxyl-4-amino-4-carboxylic acid (TOAC). TOAC is an α,α-disubstituted cyclic amino acid, which can be directly incorporated into a peptide sequence (Figure 4-2). TOAC is a significantly more rigid spin label compared to MTSSL. This spin label rigidity enables ESR measurements to more closely mimic the backbone dynamics. In the case of MTSSL, data interpretation is complicated by the dynamics of side chain.[176] Shortcomings of the TOAC label are the difficulty of synthesis and the possible disruption of certain protein folds. TOAC in a coiled-coil fold should not disrupt the structure due to the higher helix forming propensity of the unnatural amino acid.[177]

In the initial experiments, the MTSSL spin label was placed at position 14, where a Ser is mutated into a Cys. This position is located in the solvent exposed outer surface of the coiled-coil. The TOAC label was positioned by replacing a Glu residue at position 10. On the basis of the crystal structure published, position 10 was selected as a possible location that would tolerate the steric bulk.[178-179] A crystal structure made with a simplified analogue of TOAC, confirmed this hypothesis.[170]

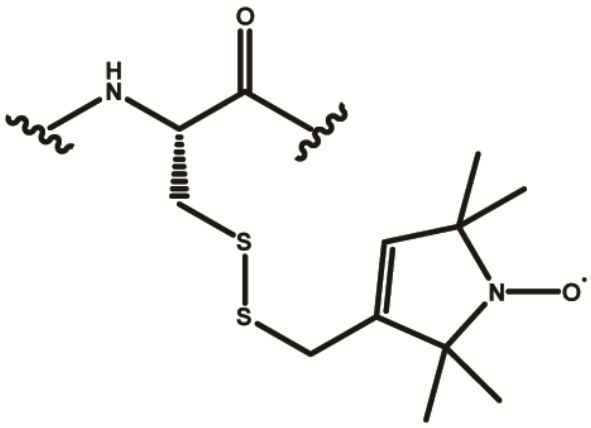

MTSSL (ρ)

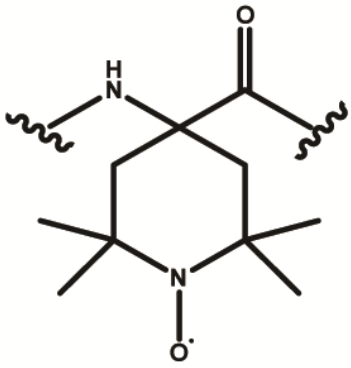

TOAC (∑)

GCN4

Ac-RMKQLEDKVEELLρKNYHLENEVARLKKLVGER-NH$_2$

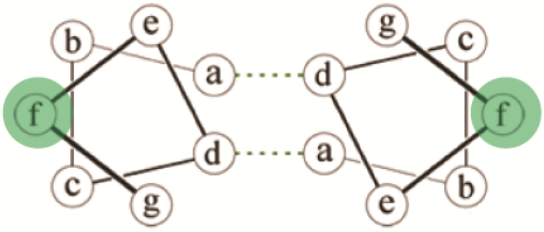

ABA-RMKQLEDKV∑ELLSKNYHLENEVARLKKLVGER-NH$_2$

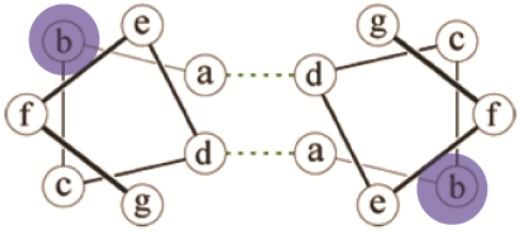

Figure 4-2 Structures of the two spin labels used MTSSL and TOAC. The GCN4 peptide sequence used and the position of the spin labels within the sequence and the helical wheel.

Then, DEER experiments were carried out on the two labeled peptides. The raw DEER data and the background subtracted DEER data are shown in Figure 4-3A and B. The modulation depth difference observed is due to the different labeling efficiencies shown by the two systems (~88% for MTSSL and ~80% for TOAC). The published coordinates of the MTSSL spin label on an α-helix was overlaid on the Ser 14 residue of the peptide to obtain the most probable distance.[180] The most probable distance obtained for MTSSL from the DEER experiment was 2.40 nm (Figure 4-3C) with a standard deviation of 0.26 nm, while the model structure predicted a distance of 2.36 nm. Similarly, a model structure was made for TOAC labeled peptide with the aid of a crystal structure containing TOAC like hexane analogue. This model structure for TOAC predicts a distance of 1.87 nm, while the most probable distance obtained from DEER is 1.95 (Figure 4-3C) nm with a standard deviation of 0.07 nm.

As predicted by previous work, TOAC spin label generated a narrower distance distribution compared to MTSSL.[176] The raw time domain data shows that there are four full periods observed for TOAC, while MTSSL has a single period, indicating the rigidity of the TOAC label. Hence, we decided to select the TOAC spin label to study the chain dynamics of the coiled-coil assemblies. More importantly, due to the sub angstrom standard deviations obtained, the distance distributions maximally reflect the conformational preferences of the supramolecular assemblies.

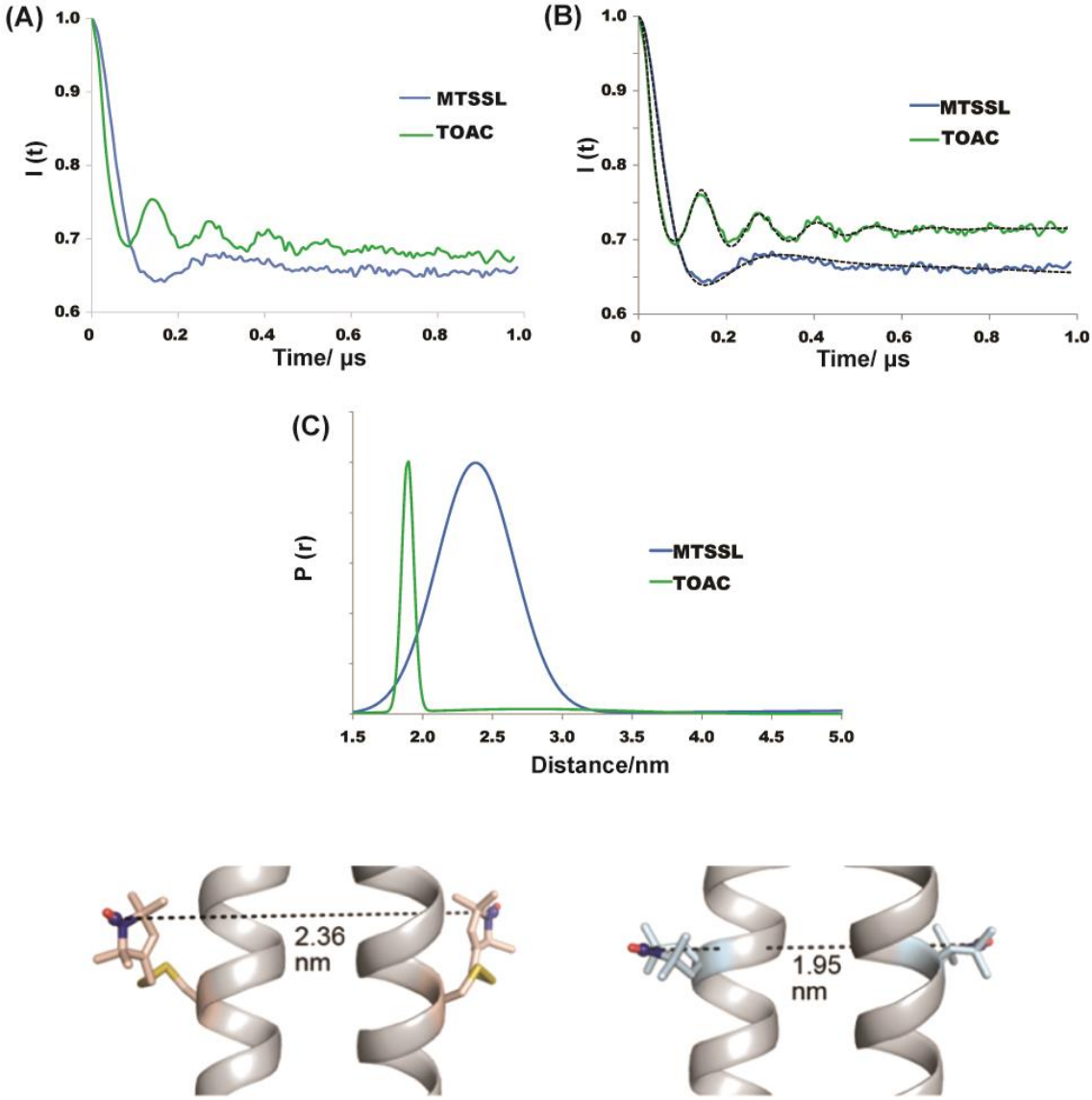

Figure 4-3 Predicted spin label distances from the structural data for peptides and the DEER distance comparison. Crystal structures shown with the permission of American Chemical Society (Tavenor et.al; *J. Phys. Chem. B* **2014**, 118, 9881−9889). The background subtracted DEER data are shown along with the single Gaussian fits. As expected the TOAC label gave a much narrower distance distribution.

DEER spectroscopy on homodimeric capped peptides

With the choice of the TOAC spin label, we extended these experiments to supramolecular polymer chains that are linked by bis-iodoacetamide groups.[8] We decided to compare the differences in the chain dynamics of the two linkers (EDA and PIP) used in the formation of supramolecular polymers (Figure 4-1).

The TOAC labeled peptide was mixed with the cross linked subunits. This mixture should give rise to the two products. First, self-associated spin labeled peptides which gives a shorter distance (~ 2nm) and second, a capped subunit where the spin labeled peptides cap the cross linked peptides, which will result in a longer distance. We mixed these peptides in a ratio which is intended to give a statistical distribution. A high ratio of capped peptide was expected based on prior observations. Hence, a higher proportion of the longer distance (subunit A in Figure 4-4) was expected.

The DEER data obtained for the mixtures and the distance distributions obtained are shown in Figure 4-4. Initially the experiments were carried out using an acquisition time of ~2.5 μs anticipating the capped subunit distance around 4-5 nm. However, as these measurements did not yield a period corresponding to the longer distance around 4-5 nm, the experiments were carried out with a shorter acquisition time (~ 1 μs) to obtain more definitive information about the shorter distance. As shown by Figure 4-4, a single Gaussian distance distribution with a most probable distance around ~1.9 nm was observed. These distance distributions match well with the distance distribution from the TOAC labeled peptide. Hence, the major species in the mixture is the spin labeled dimers (subunit B in Figure 4-4). The lower signal to noise compared to Figure 4-3, may be due to the formation of longer supramolecular polymers where the spins are not in the range for a DEER measurement.

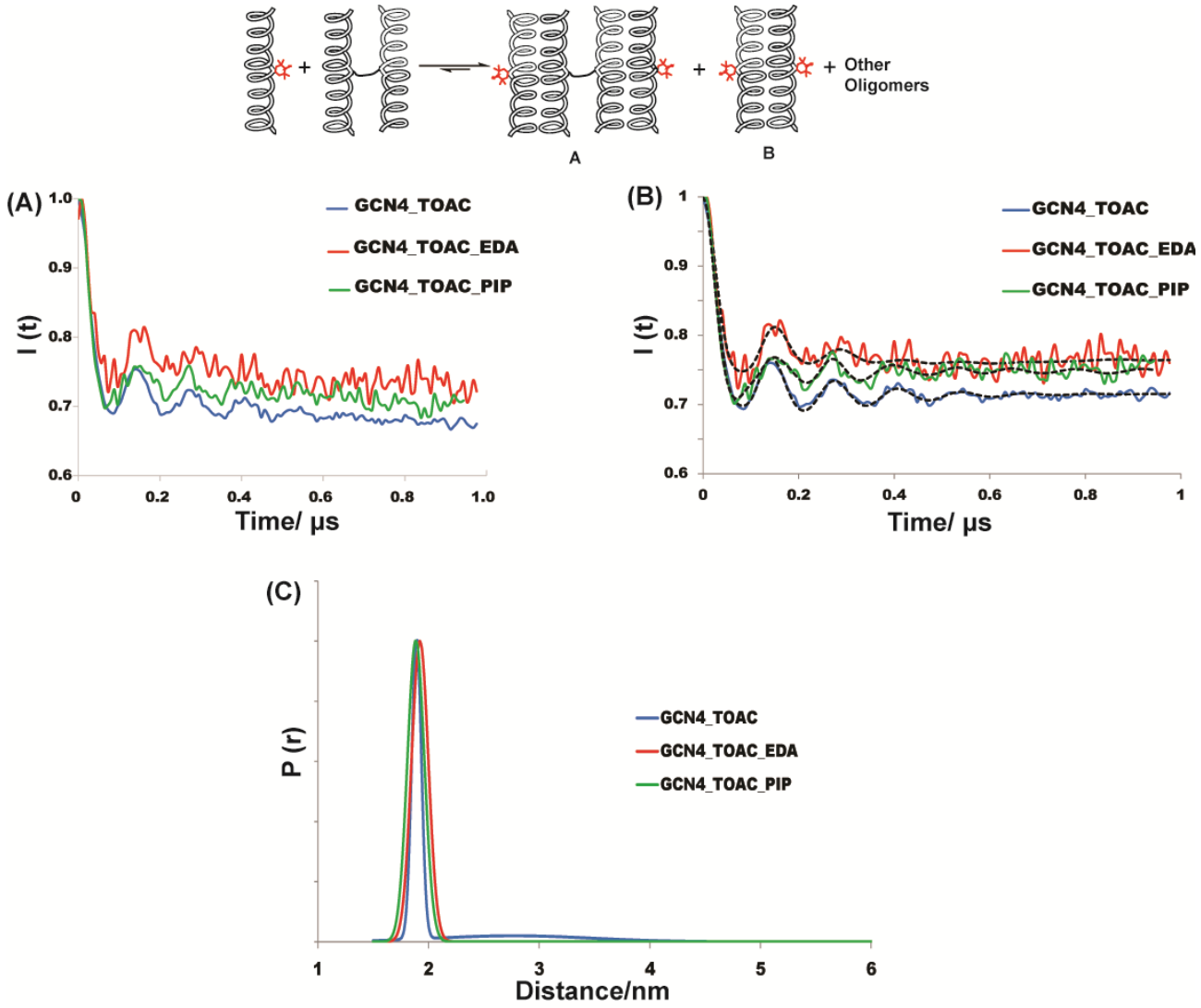

Figure 4-4 Background subtracted DEER data for the GCN4 mixed with GCN4 linker assemblies. Only the shorter distance resulting from homodimerization of the GCN4 is observed. The overlay of DEER data with the GCN4 alone match well with the GCN4+linker assemblies.

Although it is possible to increase the proportion of capped subunit by tuning the stoichiometric ratios, a more general solution would be the design of a heterodimer coiled-coil system. The heterodimer system will specifically form more capped subunits which are essential to measure the flexibilities of the covalent linkers used.

DEER spectroscopy on heterodimeric capped peptides

The design of the heterodimeric coiled-coil sequence was based on sequences reported in literature.[181] The hydrophobic core of the heterodimer assembly was similar to the homodimer system. In $BASEp_1$ peptide, eight Lys residues are introduced at the coiled coil interface in the folded state. Introduction of these Lys residues creates a highly cationic sequence. In $ACIDp_1$ peptide, the Lys residues are replaced with Glu to create a highly anionic sequence. As these different residues result in charge repulsion, the homodimerization of either sequence is unfavorable. Hence, a heterodimeric assembly is formed with complimentary charged sequences.

A Cys mutation is introduced into the $BASEp_1$ for the position corresponding to the cross-linking site. The $ACIDp_1$ peptide was modified by introducing TOAC at two different positions. First, the spin label was positioned at the 9^{th} residue (ACID9) which is located close to the crosslinking site. Then, the labeling was done at position 2 (ACID2), closer to the N-terminus of the peptide. This results in four samples with two different linkers and two spin label positions. The CD data showed that the capped sub units are much more stable than in the statistically controlled homodimer samples.

The DEER experiments were conducted on the four samples and data obtained were much higher quality than what we obtained for the homodimer system. The raw DEER data and the background subtracted DEER data for the ACID9 peptide are shown in Figure 4-5A and B. The differences in modulation depths observed for two linkers in Figures 4-5 are attributed to different

labeling efficiencies (EDA ~85% and PIP ~95%). Resulting distance distributions for both EDA and PIP linkers display a similar most probable distance at ~ 4.2 nm as shown by Figure 4-5. However, the more rigid linker PIP gave a broader distance distribution. The DEER data acquired for ACID2 peptides are shown in Figure 4-6A and B. Again, the differences in modulation depths are attributed to different spin labeling efficiencies (EDA ~77% and PIP ~98%). In these peptides PIP linker exhibits a bimodal distribution as shown by Figure 4-6. The two distributions were centered on ~ 4.2 nm and ~ 2.3 nm. EDA linked peptides gave rise to a distance distribution centered on ~ 4.2 nm. The DEER signal from PIP linker was fit using the double Gaussian function as two modulations were observed in the signal. Also, the truncation of the data preserved the proportions of the bimodal distribution. The Tikhanov regularization fit for the EDA linker showed a minor population at ~2.3 nm. Suppression of this peak did not impact the fit significantly, suggesting a very small population. Hence, both the placement of the spin label and the choice of the linker affects the distance distributions.

Molecular dynamics aided modeling, conducted by the Horne lab, enabled us to rationalize the distances obtained from DEER data. First, the MD simulations were performed on EDA and PIP linkers attached with a thioethyl moiety. Then, a random subset of structures was obtained for the trajectories of the thioethyl moiety. Next, a structure derived from the coiled coil peptides was attached to either end. In the ensuing step, the structures that encounter steric clashes with the newly introduced peptide were filtered. Finally, the structures that match up well with the DEER distances within the standard deviations were selected. For bimodal distances, separate sets of structures were generated for each distance.

To visualize the dynamics of the polymer chain the focus was on the C_α atom of the Ser 14 in the two outer helices of the capped units. The most significant difference in DEER data was

observed when the spin label was placed near the N-terminus. The EDA linker showed a single distance around ~ 4 nm, while PIP linker showed two distances around 4 nm and 2.3 nm. The capped subunits for the ~ 4 nm distance shows a random relative orientation of the two coiled coils as shown in Figure 4-7A and B. This orientation will enable the polymer to grow at a wider distribution. For the ~ 2.3 nm distance, the PIP linker shows more restricted structures, where two coiled coils are aligned in a parallel orientation as shown in Figure 4-7C. With the MD results obtained for EDA linked peptides, we hypothesize a more randomly distributed orientations that give rise to the more compact structures with a short persistence length (Figure 4-7D). The PIP linked coiled coils, with the restricted motion around the cross linked sites, only allow the polymer to grow along the same direction at each sub unit as shown in Figure 4-7D. This will result in an increase in chain stiffness and persistence.

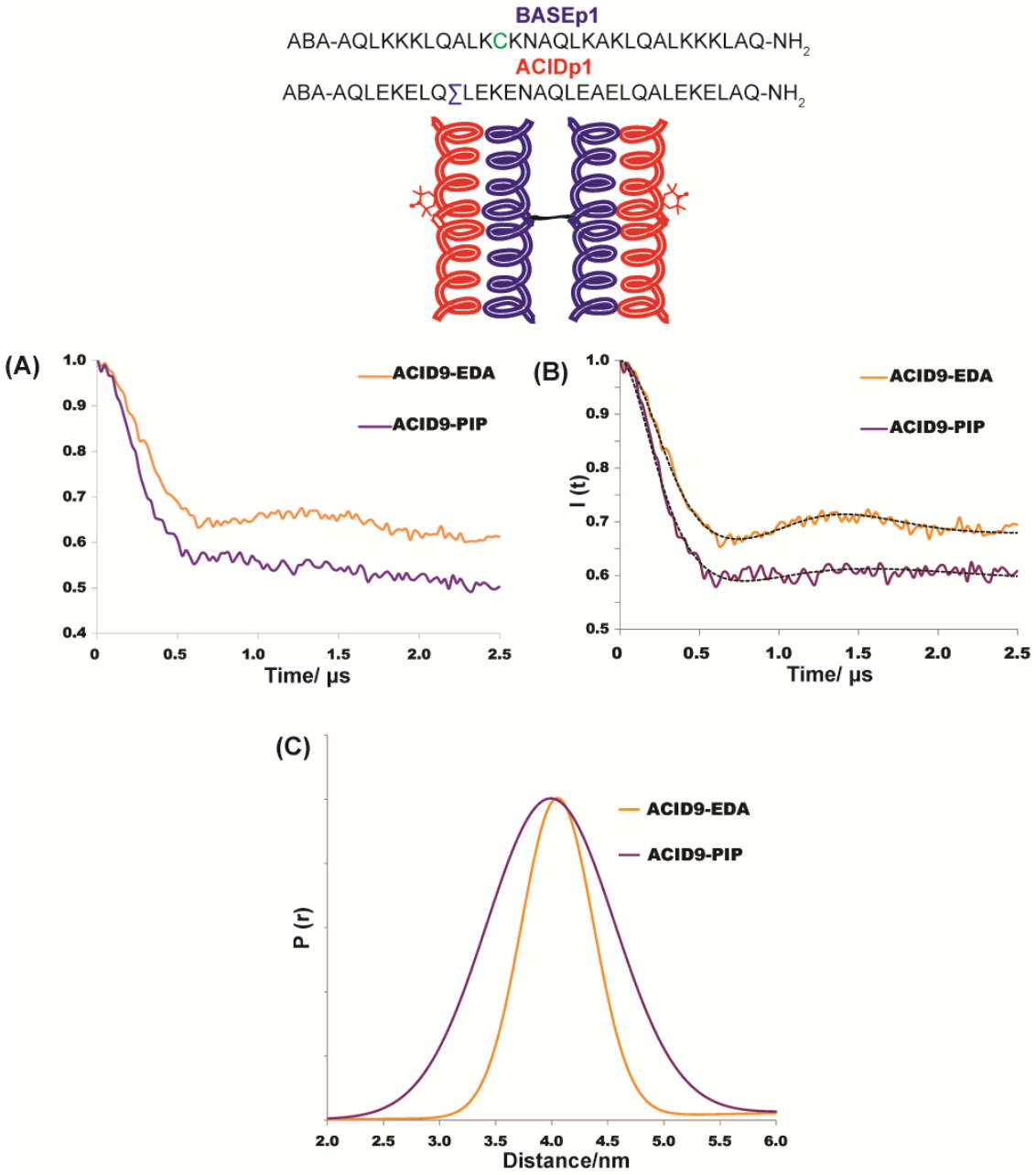

Figure 4-5 The comparison of DEER data for the EDA and PIP linkers with the spin label positioned near the linker position (9). PIP linker shows a much broader distance distribution.

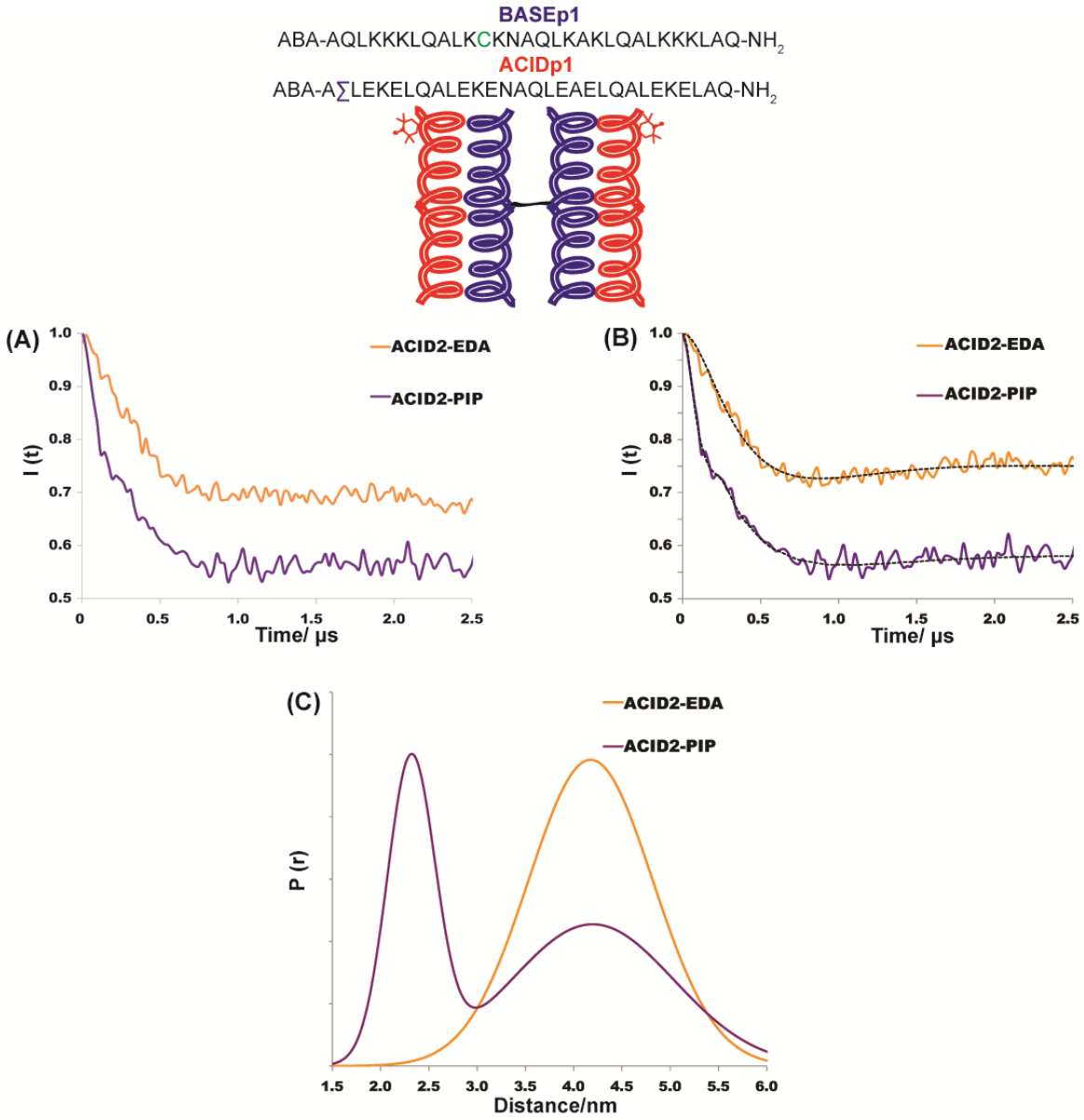

Figure 4-6 The comparison of DEER data for the EDA and PIP linkers with the spin label positioned near the N-terminus (2). PIP linker shows a much bimodal distance distribution.

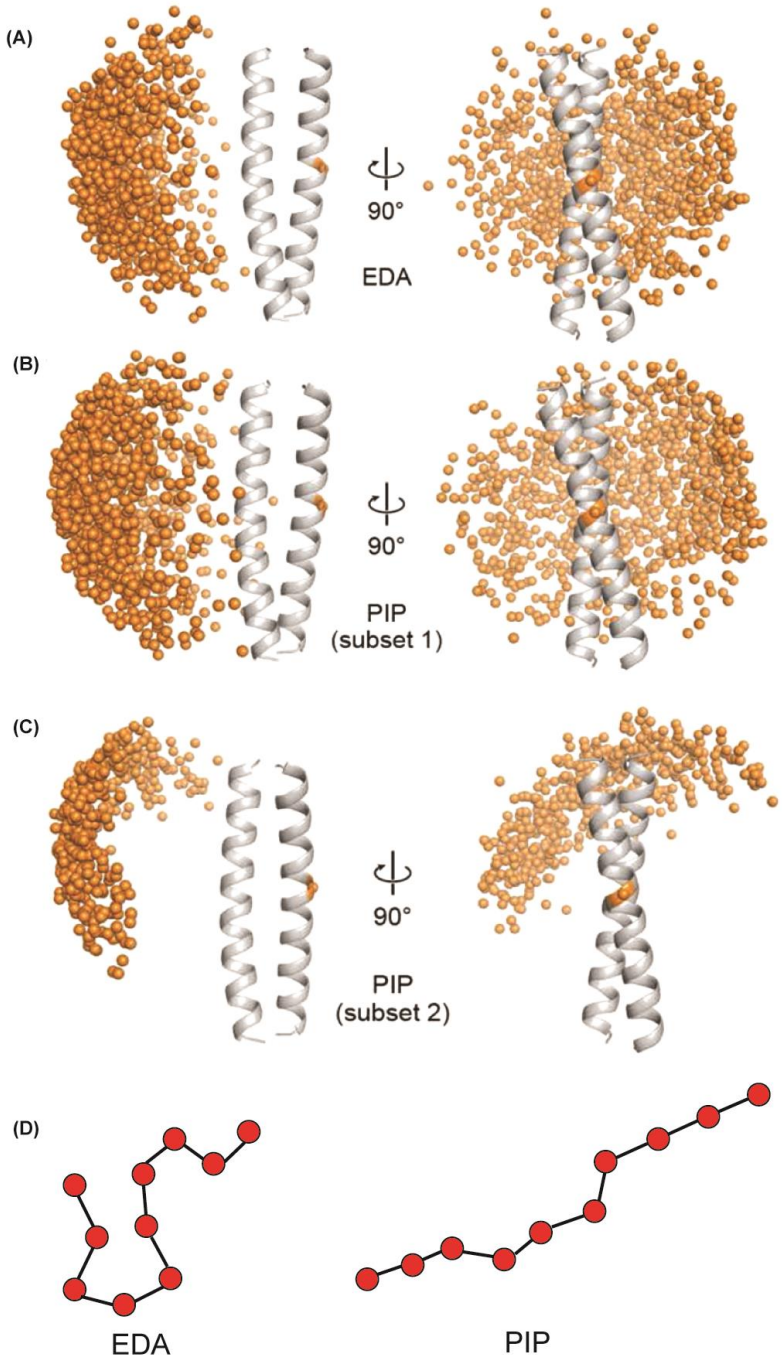

Figure 4-7 Representative ensemble for subunits with EDA linker (A) and PIP linker (B and C). Models are superimposed on two coiled coils and the orange dots represents position of the second coiled coil with respect to the point of attachment. Image reproduced with the permission of American Chemical Society (Tavenor et.al; *J. Phys. Chem. B* **2014**, 118, 9881−9889).

4.4 SUMMARY

In this work we examine the molecular origins of the observation that PIP linked coiled coil subunits form polymers with a larger apparent hydrodynamic radius than EDA linked subunits. To achieve this objective we employed DEER spectroscopy along with molecular modeling. For DEER experiments a TOAC spin label was preferred over the more common MTSSL spin label. Our strategy was to measure the conformation of a single subunit linked with either PIP or EDA by DEER spectroscopy. We found out that stoichiometric mixing of linked monomers was insufficient to generate adequate quantities of isolated subunits, but instead led to longer polymer chains. Therefore, we modified the sequence of the coiled coil such that only capped subunits are formed. In coiled coil assemblies, where the spin label was placed in the middle of the chain, both linked peptides showed a single distance distribution, with PIP linked peptides showing a broader distance distribution compared to EDA linked peptides. When, the spin label was placed near the N-terminus EDA linked peptides showed a single distance distribution, while PIP linked peptides yielded a bimodal distribution. Molecular dynamic simulations guided by the experimental DEER data suggest that the shorter distance associated with PIP linked peptides gives rise to sets of conformers where the coiled coils are oriented parallel and the positioning of the cross linking sites of the outer helices is restricted. This sub population with restricted motions along the chain causes polymer chain to propagate in the same direction, which in turn increases the hydrodynamic radius of the supramolecular assemblies.

4.5 ACKNOWLEDGEMENTS

Funding for this work was provided by the University of Pittsburgh and the National Science Foundation (MCB1157712 to S.S., CAREER award DMR1149067 to W.S.H.). The Bruker ElexSys E680 was purchased with funds from National Institutes of Health Grant 1S10RR028701. This research was supported in part by the University of Pittsburgh Center for Simulation and Modeling through the supercomputing resources provided. We specifically acknowledge the assistance of Albert DeFusco in the use of these computational resources.

5.0 OVERVIEW OF MAJOR ACHIEVEMENTS

The metal ion coordination in amyloidogenic Aβ peptide is highly heterogeneous. Three histidine residues located at positions 6, 13 and 14 are involved in the coordination of both Cu(II) and Zn(II) ions. In this context we experimentally verified a method to quantify the number of histidine residues coordinated to a Cu(II) ion using ESR spectroscopy. A series of model complexes were synthesized with different number of imidazole rings coordinated to a Cu(II) center. These complexes were used to show that the ^{14}N ESEEM integrated intensity increased monotonically with the number of imidazole rings that are coordinated to Cu(II). To check the validity of the method we used two small peptides with known Cu(II) coordination. Then the ESEEM spectroscopy is used to quantify the number of histidine residues coordinated to Cu(II) in component II coordination. We unequivocally showed that only a single histidine residue is coordinated to Cu(II) in component II. This information is critical as our experiments suggest the component II coordination is the most dominant coordination mode in the presence of Zn(II) for Aβ.

Then, we probed the changes that occur in Cu(II) coordination in the presence of Zn(II) with the use of ESR spectroscopy. We showed that Zn(II) competes with only component I of Cu(II) coordination in Aβ at physiological pH. With the aid of ESEEM spectroscopy we measured the changes in proportions of Cu(II) subcomponents in the presence of Zn(II). Our results suggests the proportions Cu(II) binding to simultaneous His13-His14 Cu(II) coordination is increased in the presence of Zn(II). An increase in His13-His14 metal ion coordination possibly leads to an increase in the amount of amorphous aggregates formed, as metal ion coordination by adjacent

amino acid residues prevents the formation of β-sheets. Furthermore, we suggest the importance of His 13 in modulating the morphology of Aβ aggregates.

Finally, we used DEER spectroscopy to determine the molecular level interactions that dictate the formation of supramolecular polymers. Specifically, we determined the factors that govern the formation of polymers with different hydrodynamic radii when ethylenediamide (EDA) and piperazine (PIP) organic linkers are used to append coiled coil domains. Strategic placement of the spin label enable us to observe different conformers for single coiled coil subunits linked with organic linkers. Molecular dynamic simulations guided by DEER data suggest some conformer populations assist the chain propagation in the same direction leading to the formation of polymers with larger hydrodynamic radius. This information is critical in the design of smart materials based on protein structures.

In addition to this research we have helped other researchers by proving valuable ESR data. The published and submitted papers are listed below.

List of publications

1. Sarver, J.; **Silva, K. I**.; Saxena, S. "Measuring Cu(II)-nitroxide distances using double electron-electron resonance and saturation recovery." *Appl. Magn. Reson.* **2013**, 44, 583–594

2. Silva, K. I.; Saxena, S. "Zn(II)-ions substantially perturb Cu(II)-ion coordination in Amyloid-β at physiological pH." *J. Phys. Chem. B* **2013**, 117, 9386–9395

3. Jianfei, J.; Bakan, A,; Kapralov, A.; **Silva, K. I**.; Huang, Z.; Amoscato, A. A.; Peterson, J.; Garapati, V. K.; Saxena, S.; Bayir, H.; Atkinson, J.; Bahar, I.; Kagan, V. E. "Designing Inhibitors of Cytochrome c/Cardiolipin Peroxidase Complexes: Mitochondria-Targeted Imidazole-Substituted Fatty Acids" *Free Radic. Bio. Med.* **2014**, 71, 221–230

4. Silva, K. I.; Micheal, B. C.; Geib, S. J.; Saxena, S. "ESEEM analysis of multi-histidine Cu(II) coordination in model complexes, peptides, and amyloid-β." *J. Phys. Chem. B* **2014**, 118, 8935-8944

5. Tavenor*, N.; **Silva*, K. I.**; Horne, W. S.; Saxena, S. "Origins of structural flexibility in protein- based supramolecular polymers revealed by DEER spectroscopy." *J. Phys. Chem. B* **2014**, 118, 9881-9889 *These authors contributed equally

6. Sarver, J. L**.;** Townsend, J.; **Silva, K. I.**; L. Jen-Jacobson, S. Saxena, "Investigating the dynamics of the arm region of EcoRI using multifrequency electron spin resonance" *Manuscript under preparation*

BIBLIOGRAPHY

(1) Lovell, M. A.; Robertsona, J. D.; Teesdaleb, W. J.; Campbell, J. L.; Markesbery, W. R., Copper, Iron and Zinc in Alzheimer's Disease Senile Plaques. *Journal of the Neurological Sciences* **1998,** *158*, 47–52

(2) Cuajungco, M. P.; Goldstein, L. E.; Nunomurai, A.; Smithi, M. A.; Lim, J. T.; Atwood, C. S.; Huang, X.; Farrag, Y. W.; Perryi, G.; Bush, A. I., Evidence That the β-Amyloid Plaques of Alzheimer's Disease Represent the Redox-Silencing and Entombment of Aβ by Zinc. *J. Biol. Chem.* **2000,** *275*, 9439–19442.

(3) Jun, S.; Saxena, S., The Aggregated State of Amyloid-β Peptide in Vitro Depends on Cu(II) Concentration. *Angew. Chem., Inter. Ed* **2007,** *46*, 3959–3961.

(4) Jun, S.; Gillespie, J. R.; Shin, B. K.; Saxena, S., The Second Cu(II)-Binding Site in a Proton-Rich Environment Interferes with the Aggregation of Amyloid-β(1-40) into Amyloid Fibrils. *Biochemistry* **2009,** *48*, 10724–10732.

(5) Faller, P.; Hureau, C., Bioinorganic Chemistry of Copper and Zinc Ions Coordinated to Amyloid-β Peptide. *Dalton Trans.* **2009**, 1080–1094.

(6) Hureau, C., Coordination of Redox Active Metal Ions to the Amyloid Precursor Protein and to Amyloid-β Peptides Involved in Alzheimer Disease. Part 1: An Overview. *Coordination Chemistry Reviews.* **2012,** *256* 2164–2174.

(7) Hureaua, C.; Dorlet, P., Coordination of Redox Active Metal Ions to the Amyloid Precursor Protein and to Amyloid-β Peptides Involved in Alzheimer Disease. Part 2: Dependence of Cu(II) Binding Sites with Aβ Sequences. *Coordination Chemistry Reviews* **2012,** *256*, 2175–2187.

(8) Staples, J. K.; Oshaben, K. M.; Horne, W. S., A Modular Synthetic Platform for the Construction of Protein-Based Supramolecular Polymers Via Coiled-Coil Self-Assembly. *Chem. Sci.* **2012,** *3*, 3387−3392.

(9) Malmström, B. G.; Leckner, J., The Chemical Biology of Copper. *Curr. Opin. Chem. Biol.* **1998,** *2*, 286–292.

(10) Rubino, J. T.; Franz, K. J., Coordination Chemistry of Copper Proteins: How Nature Handles a Toxic Cargo for Essential Function. *Journal of Inorganic Biochemistry* **2012,** *107*, 129–143.

(11) Pearson, R. G., Hard and Soft Acids and Bases. *J. Am. Chem. Soc.* **1963,** *85*, 3533–3539.

(12) Ahrland, S.; Chatt, J.; Davies, N. R., The Relative Affinities of Ligand Atoms for Acceptor Molecules and Ions. *Q. Rev. Chem. Soc.* **1958,** *12*, 265–276.

(13) Griffith, J. S.; Orgel, L. E., Ligand-Field Theory. *Q. Rev. Chem. Soc.* **1957,** *11*, 381–393.

(14) Jahn, H. A.; Teller, E., Stability of Polyatomic Molecules in Degenerate Electronic States. I. Orbital Degeneracy. *Proceedings of the Royal Society A* **1937,** *161*, 220–235.

(15) Deschampsa, P.; Kulkarnia, P. P.; Gautam-Basakb, M.; Sarkar, B., The Saga of Copper(II)–L-Histidine. *Coordination Chemistry Reviews* **2005,** *249* 895–909.

(16) Ma, K.; Clancy, E. L.; Zhang, Y.; Ray, D. G.; Wollenberg, K.; Zagorski, M. G., Residue-Specific pKa Measurements of the β-Peptide and Mechanism of pH-Induced Amyloid Formation. *J. Am. Chem. Soc* **1999,** *121*, 8698–8706.

(17) Viles, J. H., Metal Ions and Amyloid Fiber Formation in Neurodegenerative Diseases. Copper, Zinc and Iron in Alzheimer's, Parkinson's and Prion Diseases. *Coordination Chemistry Reviews* **2012,** *256*, 2271–2284.

(18) Holm, R. H.; Kennepohl, P.; Solomon, E. I., Structural and Functional Aspects of Metal Sites in Biology. *Chemical Reviews* **1996,** *96*, 2239–2314.

(19) Peisach, J.; Blumberg, W. E., Structural Implications Derived from the Analysis of EPR Spectra of Natural and Artificial Copper Proteins. *Archives of Biochemistry and Biophysics* **1974,** *165*, 691–708.

(20) Yokoi, H.; Addison, A. W., Spectroscopic and Redox Properties of Pseudotetrahedral Copper (II) Complexes. Their Relationship to Copper Proteins. *Inorg Chem* **1977,** *16*, 1341–1349.

(21) Mims, W. B., Envelope Modulation in Spin-Echo Experiments. *Phys. Rev. B* **1972,** *5*, 2409–2419.

(22) Mims, W. B.; Davis, J. L., Proton Modulation of the Electron Spin Echo Envelope in a Nd^{3+}: Aquo Glass. *J. Chem. Phys.* **1976,** *64*, 4836–4846.

(23) Mims, W. B.; Peisach, J., The Nuclear Modulation Effect in Electron Spin Echoes for Complexes of Cu^{2+} and Imidazole with ^{14}N and ^{15}N. *J. Chem. Phys.* **1978,** *69*, 4921–4930.

(24) Deligiannakis, Y.; Louloudib, M.; Hadjiliadis, N., Electron Spin Echo Envelope Modulation (ESEEM) Spectroscopy as a Tool to Investigate the Coordination Environment of Metal Centers. *Coordination Chemistry Reviews* **2000,** *201*,1–112

(25) Schweiger, A.; Jeschke, G., *Principles of Pulse Electron Paramagnetic Resonance*. Oxford University Press: New York, 2001.

(26) Dikanov, S.; Felli, I.; Viezzoli, M.-S.; Spoyalov, A.; Hiittermann, J., X-Band ESEEM Spectroscopy of ^{15}N Substituted Native and Inhibitor-Bound Superoxide Dismutase. Hyperfine Couplings with Remote Nitrogen of Histidine Ligands. *FEBS Lett.* **1994,** *345*, 55–60.

(27) McCracken, J.; Peisach, J.; Dooley, D. M., Cu(II) Coordination Chemistry of Amine Oxidases. Pulsed EPR Studies of Histidine Imidazole, Water, and Exogenous Ligand Coordination. *J. Am. Chem. Soc.* **1987,** *109*, 4064–4072.

(28) McCracken, J.; Desai, P. R.; Papadopoulos, N. J.; Villafranca, J. J.; Peisach, J., Electron Spin-Echo Studies of the Copper(II) Binding Sites in Dopamine β-Hydroxylase. *Biochemistry* **1988,** *27* 4133–4137.

(29) McCracken, J.; Pember, S.; Benkovic, S. J.; Villafranca, J. J.; Miller, R. J.; Peisach, J., Electron Spin-Echo Studies of the Copper Binding Site in Phenylalanine Hydroxylase from Chromobacterium Violaceum. *J. Am. Chem. Soc.* **1988,** *110*, 1069–1074.

(30) Jiang, F.; McCracken, J.; Peisach, J., Nuclear Quadrupole Interactions in Copper(II)-Diethylenetriamine-Substituted Imidazole Complexes and in Copper(II) Proteins. *J. Am. Chem. Soc.* **1990,** *112*, 9035–9044.

(31) McCracken, J.; Peisach, J.; Cote, C. E.; McGuirl, M. A.; Dooley, D. M., Pulsed Epr Studies of the Semiquinone State of Copper-Containing Amine Oxidases. *J. Am. Chem. Soc.* **1992,** *114* 3715–3720.

(32) Flanagan, H. L.; Singel, D. J., Analysis of Nitrogen-14 ESEEM Patterns of Randomly Oriented Solids. *J. Chem. Phys.* **1987,** *87*, 5606–5616.

(33) Goldfarb, D.; Fauth, J.-M.; Tor, Y.; Shanzer, A., Study of Cu(II) Binding to Chiral Tripodal Ligands by Electron Spin Echo Spectroscopy. *J. Am. Chem. Soc.* **1991,** *113*, 1941−1948.

(34) Dorlet, P.; Gambarelli, S.; Faller, P.; Hureau, C., Pulse EPR Spectroscopy Reveals the Coordination Sphere of Copper(II) Ions in the 1–16 Amyloid-β Peptide: A Key Role of the First Two N-Terminus Residues. *Angew. Chem., Int. Ed.* **2009,** *48*, 9273–9276.

(35) Hernández-Guzmán, J.; Sun, L.; Mehta, A. K.; Dong, J.; Lynn, D. G.; Warncke, K., Copper(II)-Bis-Histidine Coordination Structure in a Fibrillar Amyloid β-Peptide Fragment and Model Complexes Revealed by Electron Spin Echo Envelope Modulation Spectroscopy. *ChemBioChem* **2013,** *14*, 1762–1771.

(36) Millhauser, G. L., Copper and the Prion Protein: Methods, Structures, Function,and Disease. *Annu. Rev. Phys. Chem.* **2007.,** *58*, 299–320.

(37) Shin, B.-k.; Saxena, S., Insight into Potential Cu(II)-Binding Motifs in the Four Pseudorepeats of Tau Protein. *J. Phys. Chem. B* **2011,** *115*, 15067–15078.

(38) Shin, B.-k.; Saxena, S., Substantial Contribution of the Two Imidazole Rings of the His13−His14 Dyad to Cu(II) Binding in Amyloid-β(1−16) at Physiological pH and Its Significance. *J. Phys. Chem. A* **2011,** *115*, 9590–9602.

(39) Singh, V.; Zhu, Z.; Davidson, V. L.; McCracken, J., Characterization of the Tryptophan Tryptophyl-Semiquinone Catalytic Intermediate of Methylamine Dehydrogenase by Electron Spin-Echo Envelope Modulation Spectroscopy. *J. Am. Chem. Soc.* **2000,** *122*, 931–938.

(40) Höfer, P.; Grupp, A.; Nebenführ, H.; Mehring, M., Hyperfine Sublevel Correlation (Hyscore) Spectroscopy: A 2D ESR Investigation of the Squaric Acid Radical. *Chem. Phys. Lett.* **1986,** *132*, 279–282.

(41) Burns, C. S.; Aronoff-Spencer, E.; Dunham, C. M.; Lario, P.; Avdievich, N. I.; Antholine, W. E.; Olmstead, M. M.; Vrielink, A.; Gerfen, G. J.; Peisach, J.; Scott, W. G.; Millhauser, G. L., Molecular Features of the Copper Binding Sites in the Octarepeat Domain of the Prion Protein. *Biochemistry* **2002,** *41*, 3991–4001.

(42) Chattopadhyay, M.; Walter, E. D.; Newell, D. J.; Jackson, P. J.; Aronoff-Spencer, E.; Peisach, J.; Gerfen, G. J.; Bennett, B.; Antholine, W. E.; Millhauser, G. L., The Octarepeat Domain of the Prion Protein Binds Cu(II) with Three Distinct Coordination Modes at pH 7.4. *J. Am. Chem. Soc* **2005,** *127*, 12647–12656.

(43) Burns, C. S.; Aronoff-Spencer, E.; Legname, G.; Prusiner, S. B.; Antholine, W. E.; Gerfen, G. J.; Peisach, J.; Millhauser, G. L., Copper Coordination in the Full-Length, Recombinant Prion Protein. *Biochemistry* **2003,** *42*, 6794–6803.

(44) Eaton, S. S.; Eaton, G. R., Distance Measurements in Biological Systems by EPR. In *Biological Magnetic Resonance*, Berliner, L. J.; Eaton, S. S.; Eaton, G. R., Eds. Kluwer Academic: New York, 2000.

(45) Schiemann, O.; Prisner, T. F., Long-Range Distance Determinations in Biomacromolecules by Epr Spectroscopy. *Q. Rev. Biophys.* **2007,** *40*, 1–53.

(46) Eaton, S. S.; More, K. M.; Sawant, B. M.; Eaton, G. R., Use of the ESR Half-Field Transition to Determine the Interspin Distance and the Orientation of the Interspin Vector in Systems with Two Unpaired Electrons. *J. Am. Chem. Soc.* **1983,** *105*, 6560–6567.

(47) Persson, M.; Harbridge, J. R.; Hammarström, P.; Mitri, R.; Mårtensson, L.-G.; Carlsson, U.; Eaton, G. R.; Eaton, S. S., Comparison of Electron Paramagnetic Resonance Methods to Determine Distances between Spin Labels on Human Carbonic Anhydrase II. *Biophys. J.* **2001,** *80*, 2886–2897.

(48) Hustedt, E. J.; Stein, R. A.; Sethaphong, L.; Brandon, S.; Zhou, Z.; DeSensi, S. C., Dipolar Coupling between Nitroxide Spin Labels: The Development and Application of a Tether-in-a-Cone Model. *Biophys. J.* **2006,** *90*, 340–356.

(49) Rabenstein, M. D.; Shin, Y. K., Determination of the Distance between Two Spin Labels Attached to a Macromolecule. *Proc. Natl. Acad. Sci. U. S. A.* **1995,** *92*, 8239–8243.

(50) Milov, A. D.; Salikhov, K. M.; Shirov, M. D., Application of ENDOR in Electron-Spin Echo for Paramagnetic Center Distribution in Solids. *Fiz. Tverd. Tela* **1981,** *23*, 975–982.

(51) Milov, A. D.; Ponomarev, A. B.; Tsvetkov, Y. D., Electron-Electron Double Resonance in Electron Spin Echo: Model Biradical Systems and the Sensitized Photolysis of Declain. *Chem. Phys. Lett* **1984,** *110*, 67–72

(52) Pannier, M.; Veit, S.; Godt, A.; Jeschke, G.; Spiess, H. W., Dead-Time Free Measurement of Dipole-Dipole Interactions between Electron Spins. *J. Magn. Reson.* **2000,** *142*, 331–340.

(53) Saxena, S.; Freed, J. H., Double Quantum Two Dimensional Fourier Transform Electron Spin Resonance: Distance Measurements. *Chem. Phys. Lett.* **1996,** *251*, 102–110.

(54) Saxena, S.; Freed, J. H., Theory of Double Quantum Two Dimensional Electron Spin Resonance with Application to Distance Measurements. *J. Chem. Phys.* **1997,** *107*, 1317–1340.

(55) Jun, S.; Becker, J.; Yonkunas, M.; R.Coalson; Saxena, S., Unfolding of Alanine-Based Peptides Using Electron Spin Resonance Distance Measurements. *Biochemistry* **2006,** *45*, 11666–11673.

(56) Sarver, J. L.; Silva, K. I.; Saxena, S., Measuring Cu^{2+}-Nitroxide Distances Using Double Electron-Electron Resonance and Saturation Recovery *Appl. Magn. Reson.* **2013,** *44*, 583–594.

(57) Altenbach, C.; Flitsch, S. L.; Khorana, H. G.; Hubbell, W. L., Structural Studies on Transmembrane Proteins. 2. Spin Labeling of Bacteriorhodopsin Mutants at Unique Cysteines. *Biochemistry* **1989,** *28*, 7806–7812.

(58) Altenbach, C.; Marti, T.; Khorana, H.; Hubbell, W., Transmembrane Protein Structure: Spin Labeling of Bacteriorhodopsin Mutants. *Science* **1990,** *248*, 1088–1092.

(59) Sonia Longhi; Val´ erie Belle; Andr´e Fournel; Guigliarelli, B.; Carriere F., Probing Structural Transitions in Both Structured and Disordered Proteins Using Site-Directed Spin-Labeling EPR Spectroscopy. *J. Pept. Sci.* **2011,** *17*, 315–328.

(60) Klare J. P., Site-Directed Spin Labeling EPR Spectroscopy in Protein Research. *Biol Chem.* **2013,** *394*, 1281–1300.

(61) Schreier, S.; Bozelli, J.; Marín, N.; Vieira, R.; Nakaie, C., The Spin Label Amino Acid Toac and Its Uses in Studies of Peptides: Chemical, Physicochemical, Spectroscopic, and Conformational Aspects. *Biophys. Rev.* **2012,** *4*, 45−66.

(62) Larsen, R. G.; Singel, D. J., Double Electron--Electron Resonance Spin--Echo Modulation: Spectroscopic Measurement of Electron Spin Pair Separations in Orientationally Disordered Solids. *J. Chem. Phys.* **1993,** *98*, 5134–5146.

(63) Jeschke, G.; Chechik, V.; Ionita, P.; Godt, A.; Zimmermann, H.; Banham, J.; Timmel, C. R.; Hilger, D.; Jung, H., Deeranalysis2006: A Comprehensive Software Package for Analyzing Pulsed Eldor Data. *Appl. Magn. Reson.* **2006,** *30*, 473−498.

(64) Binolfi, A. S.; Lamberto, G. R.; Duran, R.; Quintanar, L.; Bertoncini, C. W.; Souza, J. M.; Cerven˜ansky, C.; Zweckstetter, M.; Griesinger, C.; Ferna´ndez, C. O., Site-Specific

Interactions of Cu(II) with α and β-Synuclein: Bridging the Molecular Gap between Metal Binding and Aggregation. *J. Am. Chem. Soc.* **2008,** *130* 11801–11812.

(65) Binolfi, A.; Rodriguez, E. E.; Valensin, D.; D'Amelio, N.; Ippoliti, E.; Obal, G.; Duran, R.; Magistrato, A.; Pritsch, O.; Zweckstetter, M.; Valensin, G.; Carloni, P.; Quintanar, L.; Griesinger, C.; Fernández, C. O., Bioinorganic Chemistry of Parkinson's Disease: Structural Determinants for the Copper-Mediated Amyloid Formation of Alpha-Synuclein. *Inorg. Chem.* **2010,** *49*, 10668–10679.

(66) Drew, S. C.; Leong, S. L.; Pham, C. L. L.; Tew, D. J.; Masters, C. L.; Miles, L. A.; Cappai, R.; Barnham, K. J., Cu^{2+} Binding Modes of Recombinant α-Synuclein-Insights from EPR Spectroscopy. *J. Am. Chem. Soc.* **2008,** *130*, 7766–7773.

(67) Bortolus, M.; Bisaglia, M.; Zoleo, A.; Fittipaldi, M.; Benfatto, M.; Bubacco, L.; Maniero, A. L., Structural Characterization of a High Affinity Mononuclear Site in the Copper(II)-α-Synuclein Complex. *J. Am. Chem. Soc.* **2010,** *132*, 18057–18066.

(68) Dudzik, C. G.; Walter, E. D.; Millhauser, G. L., Coordination Features and Affinity of the Cu^{2+} Site in the α-Synuclein Protein of Parkinson's Disease. *Biochemistry* **2011,** *50* 1771–1777.

(69) Binolfia, A.; Quintanarb, L.; Bertoncinic, C. W.; Griesingerd, C.; Fernández, C. O., Bioinorganic Chemistry of Copper Coordination to α-Synuclein: Relevance to Parkinson's Disease. *Coordination Chemistry Reviews* **2012,** *256*, 2188– 2201.

(70) Rasia, R. M.; Bertoncini, C. W.; Marsh, D.; Hoyer, W.; Cherny, D.; Zweckstetter, M.; Griesinger, C.; Jovin, T. M.; Fernández, C. O., Structural Characterization of Copper(II) Binding to α-Synuclein: Insights into the Bioinorganic Chemistry of Parkinson's Disease. *Proc Natl. Acad. Sci.* **2005,** *102* 4294–4299.

(71) Aronoff-Spencer, E.; Burns, C. S.; Avdievich, N. I.; Gerfen, G. J.; Peisach, J.; Antholine, W. E.; Ball, H. L.; Cohen, F. E.; Prusiner, S. B.; Millhauser, G. L., Identification of the Cu^{2+} Binding Sites in the N-Terminal Domain of the Prion Protein by EPR and CD Spectroscopy. *Biochemistry* **2000,** *39*, 13760–13771.

(72) Klewpatinond, M.; Davie, P.; Bowen, S.; Brown, D. R.; Viles, J. H., Deconvoluting the Cu^{2+} Binding Modes of Full-Lengt Prion Protein. *J. Biol. Chem.* **2007,** *283*, 1870–1881.

(73) Walter, E. D.; Stevens, D. J.; Visconte, M. P.; Millhauser, G. L., The Prion Protein Is a Combined Zinc and Copper Binding Protein: Zn^{2+} Alters the Distribution of Cu^{2+} Coordination Modes. *J. Am. Chem. Soc.* **2007,** *129* 15440–15441.

(74) Jackson, G. S.; Murray, I.; Hosszu, L. L. P.; Gibbs, N.; Waltho, J. P.; Clarke, A. R.; Collinge, J., Location and Properties of Metal-Binding Sites on the Human Prion Protein. *Proc. Natl. Acad. Sci. U.S.A.* **2001,** *98*, 8531–8535.

(75) Jones, C. E.; Klewpatinond, M.; Abdelraheim, S. R.; Brown, D. R.; Viles, J. H., Probing Cu^{2+} Binding to the Prion Protein Using Diamagnetic Ni^{2+} and 1H NMR: The Unstructured N Terminus Facilitates the Coordination of Six Cu^{2+} Ions at Physiological Concentrations. *J. Mol. Biol.* **2005,** *346*, 1393–1407.

(76) Stellato, F.; Spevacek, A.; Proux, O.; Minicozzi, V.; Millhauser, G.; Morante, S., Zinc Modulates Copper Coordination Mode in Prion Protein Octa-Repeat Subdomains. *Eur Biophys J* **2011,** *40*, 1259–1270.

(77) Morante, S.; González-Iglesias, R.; Potrich, C.; Meneghini, C.; Meyer-Klaucke, W.; Menestrina, G.; Gasset, M., Inter- and Intra-Octarepeat Cu(II) Site Geometries in the Prion Protein Implications in Cu(II) Binding Cooperativity and Cu(II)-Mediated Assemblies. *J Biol Chem* **2004,** *279*, 11753–11759.

(78) Furlan, S.; Penna, G. L.; Guerrieri, F.; Morante, S.; Rossi, G. C., Ab Initio Simulations of Cu Binding Sites on the N-Terminal Region of Prion Protein. *J Biol Inorg Chem* **2007,** *12*, 571–583.

(79) Guerrieri, F.; Minicozzi, V.; Morante, S.; Rossi, G.; Furlan, S.; Penna, G. L., Modeling the Interplay of Glycine Protonation and Multiple Histidine Binding of Copper in the Prion Protein Octarepeat Subdomains. *J Biol Inorg Chem* **2009,** *14*, 361–374.

(80) Quintanar, L.; Rivillas-Acevedo, L.; Grande-Aztatzi, R.; Gómez-Castro, C. Z.; Arcos-López, T.; Vela, A., Copper Coordination to the Prion Protein: Insights from Theoretical Studies. *Coordination Chemistry Reviews* **2013,** *257*, 429–444.

(81) Syme, C. D.; Nadal, R. C.; Rigby, S. E. J.; Viles, J. H., Copper Binding to the Amyloid-β (Aβ) Peptide Associated with Alzheimer's Disease. *J. Biol. Chem.* **2004,** *279*, 18169–18177.

(82) Guilloreau, L.; Damian, L.; Coppel, Y.; Mazarguil, H.; Winterhalter, M.; Faller, P., Structural and Thermodynamical Properties of Cu(II) Amyloid-β16/28 Complexes Associated with Alzheimer's Disease. *Journal of Biological Inorganic Chemistry* **2006,** *11*, 1024–1038.

(83) Shin, B.-k.; Saxena, S., Direct Evidence That All Three Histidine Residues Coordinate to Cu(II) in Amyloid-β(1−16). *Biochemistry* **2008,** *47*, 9117–9123.

(84) Morante, S., The Role of Metals in β-Amyloid Peptide Aggregation: X-Ray Spectroscopy and Numerical Simulations. *Current Alzheimer's Research* **2008,** *5*, 508–524.

(85) Faller, P.; Hureau, C., Impact of Metallic Ions in Alzheimer's Disease: Insights from XAS Spectroscopy. *Actualite Chimique* **2011**, 356–357.

(86) Hureau, C.; Coppel, Y.; Dorlet, P.; Solari, P. L.; Sayen, S.; E, E. G.; Sabater, L.; Faller, P., Deprotonation of the Asp1-Ala2 Peptide Bond Induces Modification of the Dynamic Copper(II) Environment in the Amyloid-Beta Peptide near Physiological pH. *Angew. Chem., Int. Ed.* **2009,** *121*, 9686–9689.

(87) Kowalik-Jankowska, T.; Ruta, M.; Wisniewska, K.; Łankiewicz, L., Coordination Abilities of the 1–16 and 1–28 Fragments of β-Amyloid Peptide Towards Copper(II) Ions: A Combined Potentiometric and Spectroscopic Study. *Journal of Inorganic Biochemistry* **2003,** *95*, 270–282.

(88) Lu, Y.; Prudent, M.; Qiao, L.; Mendeza, M. A.; Girault, H. H., Copper(I) and Copper(II) Binding to β-Amyloid 16 (Aβ16) Studied by Electrospray Ionization Mass Spectrometry. *Metallomics* **2010,** *2*, 474–479.

(89) Raffa, D. F.; Go´mez-Balderas, R.; Brunelle, P.; Rickard, G. A.; Rauk, A., Ab Initio Model Studies of Copper Binding to Peptides Containing a His–His Sequence: Relevance to the β-Amyloid Peptide of Alzheimer's Disease. *J Biol Inorg Chem* **2005,** *10*, 887–902.

(90) Rauk, A., Why Is the Amyloid Beta Peptide of Alzheimer's Disease Neurotoxic? *Dalton Trans.* **2008**, 1273–1282.

(91) Drew, S. C.; Noble, C. J.; Masters, C. L.; Hanson, G. R.; Barnham, K. J., Pleomorphic Copper Coordination by Alzheimer's Disease Amyloid-β Peptide. *J. Am. Chem. Soc* **2009,** *131*, 1195–1207.

(92) Silva, K. I.; Saxena, S., Zn(II) Ions Substantially Perturb Cu(II) Ion Coordination in Amyloid-β at Physiological pH. *J. Phys. Chem. B* **2013,** *117*, 9386–9394.

(93) Gunderson, W. A.; Hernández-Guzmán, J.; Karr, J. W.; Sun, L.; Szalai, V. A.; Warncke, K., Local Structure and Global Patterning of Cu^{2+} Binding in Fibrillar Amyloid-β [Aβ(1–40)] Protein. *J. Am. Chem. Soc.* **2012,** *134* 18330–18337.

(94) Alies, B.; Sasaki, I.; Sayen, S.; Guillon, E.; Faller, P.; Hureau, C., Zn Impacts Cu Coordination to Amyloid-β, the Alzheimer's Peptide, but Not the ROS Production and the Associated Cell Toxicity. *Chem. Commun.* **2013,** *49*, 2130–2132.

(95) Fauth, J. M.; Schweiger, A.; Braunschweiler, L.; Forrer, J.; Ernst, R. R., Elimination of Unwanted Echoes and Reduction of Dead Time in Three-Pulse Electron Spin-Echo Spectroscopy. *Journal of Magnetic Resonance* **1986,** *66*, 74–85

(96) Fransson, G.; Lundberg, B. K. S., Metal Complexes with Mixed Ligands, 4. The Crystal Structure of Tetrakisimidazole Cu(II) Sulphate, $Cu(C_3H_4N_2)_4SO_4$. *Acta Chem. Scand* **1972,** *26*, 3969−3976.

(97) Abuhijleh, A. L.; Woods, C.; Ahmed, I. Y., Synthesis and Molecular Structure of Monomeric Copper(II) Acetates with 2-Methylimidazole and 1,2-Dimethylimidazole. *Inorganica Chim. Acta* **1990,** *190*, 11–17.

(98) Sato, M.; Nagae, S.; Ohmae, K.; Nakaya, J.-I., Preparation and Crystal Structure of an Imidazolate: Bridged Polynuclear Complex [{Cu(Im)(Dien)}N][ClO_4]N (Dien = Diethylenetriamine), and Its Properties in Dimethyl Sulfoxide Solution. *J. Chem. Soc., Dalton Trans.* **1986**, 1949–1953.

(99) Merrifield, R. B., Solid Phase Peptide Synthesis. I. The Synthesis of a Tetrapeptide. *J. Am. Chem. Soc.* **1963,** *85* 2149–2154.

(100) Fields, G. B.; Noble, R. L., Solid Phase Peptide Synthesis Utilizing 9-Fluorenylmethoxycarbonyl Amino Acids. *Int. J. Peptide Protein Res.* **1990,** *35*, 161–214.

(101) Gemperle, C.; Aebli, G.; Schweiger, A.; Ernst, R. R., Phase Cycling in Pulse EPR. *Journal of Magnetic Resonance* **1990,** *88*, 241–256.

(102) Guilloreau, L.; Combalbert, S.; Sournia-Saquet, A.; Mazarguil, H.; Faller, P., Redox Chemistry of Copper–Amyloid-β: Thegeneration of Hydroxyl Radical in the Presenceof Ascorbate Is Linked to Redox-Potentials and Aggregation State. *ChemBioChem* **2007,** *8*, 1317–1325.

(103) Lai, A.; Flanagan, H. L.; Singel, D. J., Multifrequency Electron Spin Echo Envelope Modulation in S=1/2, I=1/2 Systems: Analysis of the Spectral Amplitudes, Line Shapes, and Linewidths. *J. Chem. Phys.* **1988,** *89*, 7161–7166.

(104) Tang, X. S.; Diner, B. A.; Larsen, B. S.; Gilchrist, M. L., Jr.; Lorigan, G. A.; Britt, R. D., Identification of Histidine at the Catalytic Site of the Photosynthetic Oxygen-Evolving Complex. *Proc. Natl. Acad. Sci. USA* **1994,** *91*, 704–708.

(105) Stoll, S.; Calle, C.; Mitrikas, G.; Schweiger, A., Peak Suppression in ESEEM Spectra of Multinuclear Spin Systems. *Journal of Magnetic Resonance* **2005,** *177*, 93–101.

(106) Ma, Q.-F.; Hu, J.; Wu, W.-H.; Liu, H.-D.; Du, J.-T.; Fu, Y.; Wu, Y.-W.; Lei, P.; Zhao, Y.-F.; Li, Y.-M., Characterization of Copper Binding to the Peptide Amyloid-β(1–16) Associated with Alzheimer's Disease. *Biopolymers* **2006,** *83*, 20–31.

(107) Zhang, X.; Tian, Y.; Li, Z.; Tian, X.; Sun, H.; Liu, H.; Moore, A.; Ran, C., Design and Synthesis of Curcumin Analogues for in Vivo Fluorescence Imaging and Inhibiting Copper-Induced Cross-Linking of Amyloid Beta Species in Alzheimer's Disease. *J. Am. Chem. Soc* **2013,** *135*, 16397–16409.

(108) Drew, S. C.; Masters, C. L.; Barnham, K. J., Alanine-2 Carbonyl Is an Oxygen Ligand in Cu^{2+} Coordination of Alzheimer's Disease Amyloid-β Peptide − Relevance to N-Terminally Truncated Forms. *J. Am. Chem. Soc.* **2009,** *131* 8760–8761.

(109) Maret, W., Metalloproteomics, Metalloproteomes, and the Annotation of Metalloproteins. *Metallomics* **2010,** *2*, 117–125.

(110) Kaplan, J. H.; Lutsenko, S., Copper Transport in Mammalian Cells: Special Care for a Metal with Special Needs. *J. Biol. Chem.* **2009,** *284*, 25461–25465.

(111) Turski, M. L.; Thiele, D. J., New Roles for Copper Metabolism in Cell Proliferation, Signaling, and Disease. *J. Biol. Chem.* **2009,** *284*, 717–721.

(112) Kim, B. E.; Nevitt, T.; Thiele, D. J., Mechanisms for Copper Acquisition, Distribution and Regulation. *Nat. Chem. Biol.* **2008,** *4*, 176–185.

(113) Ducea, J. A.; Bush, A. I., Biological Metals and Alzheimer's Disease: Implications for Therapeutics and Diagnostics. *Progress in Neurobiology* **2010,** *92*, 1–18.

(114) Blennow, K.; de Leon, M. J.; Zetterberg, H., Alzheimer's Disease. *Lancet* **2006,** *368*, 387–403.

(115) Mattson, M. P., Pathways Towards and Away from Alzheimer's Disease. *Nature* **2004,** *430*, 631–639

(116) Guy, M.; David, K.; Howard, C.; Bradley, H.; Jr, J. C.; Claudia, K.; William, K.; Walter, K.; Jennifer, M.; Richard, M.; Richard, M.; John, M.; Martin, R.; Philip, S.; Maria, C.; Bill, T.; Sandra, W.; Creighton, P., The Diagnosis of Dementia Due to Alzheimer's Disease: Recommendations from the National Institute on Aging-Alzheimer's Association Workgroups on Diagnostic Guidelines for Alzheimer's Disease. *Alzheimer's & dementia : the journal of the Alzheimer's Association* **2011,** *7* 263–269.

(117) Kepp, K. P., Bioinorganic Chemistry of Alzheimer's Disease. *Chem. Rev.* **2012,** *112*, 5193–5239.

(118) Noy, D.; Solomonov, I.; Sinkevich, O.; Arad, T.; Kjaer, K.; Sagi, I., Zinc-Amyloid-β Interactions on a Millisecond Time-Scale Stabilize Non-Fibrillar Alzheimer-Related Species. *J. Am. Chem. Soc.* **2008** *130* 1376–1383.

(119) Garai, K.; Sahoo, B.; Kaushalya, S. K.; Desai, R.; Maiti, S., Zinc Lowers Amyloid-β Toxicity by Selectively Precipitating Aggregation Intermediates. *Biochemistry* **2007,** *46*, 10655–10663.

(120) Hamley, I. W., The Amyloid Beta Peptide: A Chemist's Perspective. Role in Alzheimer's and Fibrillization. *Chem. Rev.* **2012,** *112*, 5147–5192.

(121) Damante, C. A.; Ősz, K.; Nagy, Z. N.; Pappalardo, G.; Grasso, G.; Impellizzeri, G.; Rizzarelli, E.; Sóvágó, I., Metal Loading Capacity of Aβ N-Terminus: A Combined Potentiometric and Spectroscopic Study of Zinc(II) Complexes with Aβ(1−16), Its Short or Mutated Peptide Fragments and Its Polyethylene Glycol−Ylated Analogue. *Inorg. Chem.* **2009,** *48*, 10405–10415.

(122) Karr, J. W.; Kaupp, L. J.; Szalai, V. A., Amyloid-β Binds Cu^{2+} in a Mononuclear Metal Ion Binding Site. *J. Am. Chem. Soc* **2004,** *126*, 13534–13538.

(123) Karr, J. W.; Akintoye, H.; Kaupp, L. J.; Szalai, V. A., N-Terminal Deletions Modify the Cu^{2+} Binding Site in Amyloid-β. *Biochemistry* **2005,** *44* 5478–5487.

(124) Karr, J. W.; Szalai, V. A., Cu(II) Binding to Monomeric, Oligomeric, and Fibrillar Forms of the Alzheimer's Disease Amyloid-β Peptide. *Biochemistry* **2008** *47*, 5006–5016.

(125) Minicozzi, V.; Stellato, F.; Comai, M.; Serra, M. D.; Potrich, C.; Meyer-Klaucke, W.; Morante, S., Identifying the Minimal Copper- and Zinc-Binding Site Sequence in Amyloid-β Peptides. *J. Biol. Chem.* **2008,** *283*, 10784–10792.

(126) Kozina, S. A.; Zirahc, S.; Rebuffatc, S.; Hoad, G. H. B.; Debey, P., Zinc Binding to Alzheimer's Aβ(1–16) Peptide Results in Stable Soluble Complex. *Biochem. Biophys. Res. Commun.* **2001,** *285*, 959–964.

(127) Zirah, S. V.; Kozin, S. A.; Mazur, A. K.; Blond, A.; Cheminant, M.; Se´galas-Milazzo, I.; Debey, P.; Rebuffat, S., Structural Changes of Region 1–16 of the Alzheimer's Disease Amyloid β - Peptide Upon Zinc Binding and in-Vitro Aging *J. Biol. Chem.* **2006,** *281*, 2151–2161.

(128) Syme, C. D.; Viles, J. H., Solution ^{1}H NMR Investigation of Zn^{2+} and Cd^{2+} Binding to Amyloid-Beta Peptide (Aβ) of Alzheimer's Disease. *Biochem. Biophys. Res. Commun.* **2006,** *1764, 246*, 246–256.

(129) Danielsson, J.; Pierattelli, R.; Banci, L.; Gräslund, A., High-Resolution NMR Studies of the Zinc-Binding Site of the Alzheimer's Amyloid Beta-Peptide. *FEBS J.* **2007,** *274* 46.

(130) Tsvetkov, P. O.; Kulikova, A. A.; Golovin, A. V.; Tkachev, Y. V.; Archakov, A. I.; Kozin, S. A.; Makarov, A. A., Minimal Zn^{2+} Binding Site of Amyloid-β. *Biophys. J.* **2010,** *99*, L84– L86.

(131) Damante, C. A.; Ösz, K.; Nagy, Z. N.; Grasso, G.; Pappalardo, G.; Rizzarelli, E.; Sóvágó, I., Zn^{2+}'S Ability to Alter the Distribution of Cu^{2+} among the Available Binding Sites of Aβ(1–16)-Polyethylenglycol-Ylated Peptide: Implications in Alzheimer's Disease. *Inorg. Chem.* **2011,** *50*, 5342–5350.

(132) Braymer, J. J.; Choi, J.-S.; DeToma, A. S.; Wang, C.; Nam, K.; Kampf, J. W.; Ramamoorthy, A.; Lim, M. H., Development of Bifunctional Stilbene Derivatives for Targeting and Modulating Metal-Amyloid-β Species. *Inorg. Chem.* **2011,** *50*, 10724–10734.

(133) Jones, M. R.; Service, E. L.; Thompson, J. R.; Wang, M. C. P.; Kimsey, I. J.; DeToma, A. S.; Ramamoorthy, A.; Lim, M. H.; Storr, T., Dual-Function Triazole–Pyridine Derivatives as Inhibitors of Metal-Induced Amyloid-β Aggregation. *Metallomics* **2012,** *4*, 910–920.

(134) Collin, F.; Sasaki, I.; Eury, H.L.N.; Faller, P.; Hureau, C., Pt(II) Compounds Interplay with Cu(II) and Zn(II) Coordination to the Amyloid-β Peptide Has Metal Specific Consequences on Deleterious Processes Associated to Alzheimer's Disease. *Chem. Commun.* **2013,** *49*, 2130–2132.

(135) Kirkitadze, M. D.; Condron, M. M.; Teplow, D. B., Identification and Characterization of Key Kinetic Intermediates in Amyloid Beta-Protein Fibrillogenesis. *J Mol Biol.* **2001,** *312*, 1103–1119.

(136) Fraser, P. E.; Nguyen, J. T.; Surewicz, W. K.; Kirschner, D. A., pH-Dependent Structural Transitions of Alzheimer Amyloid Peptides. *Biophysical J.* **1991,** *60*, 1190–1201.

(137) Mithu, V. S.; Sarkar, B.; Bhowmik, D.; Chandrakesan, M.; Maiti, S.; Madhu, P. K., Zn^{++} Binding Disrupts the Asp^{23}-Lys^{28} Salt Bridge without Altering the Hairpin-Shaped Cross-B Structure of $A\beta_{42}$ Amyloid Aggregates. *Biophys. J.* **2011,** *101*, 2825–2832.

(138) Crick, F., The Packing of α-Helices: Simple Coiled-Coils. *Acta Crystallogr.* **1953,** *6*, 689−697.

(139) Liu, J.; Rost, B., Comparing Function and Structure between Entire Proteomes. *Protein Science* **2001,** *10*, 1970–1979.

(140) Litowski J. R.; S., H. R., Designing Heterodimeric Two-Stranded Alpha-Helical Coiled-Coils. Effects of Hydrophobicity and Alpha-Helical Propensity on Protein Folding, Stability, and Specificity. *J Biol Chem.* **2002,** *277*, 37272–37279.

(141) Liu, J.; Deng, Y.; Cheng, C.-S.; Kallenbach, N. R.; Lu, M., A Seven-Helix Coiled Coil. *Proc. Natl. Acad. Sci. U.S.A.* **2006,** *103*, 15457–15462.

(142) Dong, H.; Hartgerink, J. D., Short Homodimeric and Heterodimeric Coiled Coils. *Biomacromolecules* **2006,** *8*, 617–623.

(143) Burkhard, P.; Meier, M.; Lustig, A., Design of a Minimal Protein Oligomerization Domain by a Structural Approach. *Protein Sci.* **2000,** *9*, 2294–2301.

(144) Yu, Y. B., Coiled-Coils: Stability, Specificity, and Drug Delivery Potential. *Adv. Drug Delivery Rev.* **2002,** *54*, 1113–1129.

(145) N., W. D., The Design of Coiled-Coil Structures and Assemblies. *Adv Protein Chem.* **2005,** *70*, 79–112.

(146) G., O. M.; J., H. J., The Design of Antiparallel Coiled Coils. *Curr Opin Struct Biol.* **2001,** *4*, 450–457.

(147) Hadley, E. B.; Testa, O. D.; Woolfson, D. N.; Gellman, S. H., Preferred Side-Chain Constellations at Antiparallel Coiled-Coil Interfaces. *Proc. Natl. Acad. Sci. U.S.A.* **2008,** *105*, 530–535.

(148) Tang, Y.; Ghirlanda, G.; Vaidehi, N.; Kua, J.; Mainz, D. T.; Goddard, W. A., III; DeGrado, W. F.; Tirrell, D. A., Stabilization of Coiled-Coil Peptide Domains by Introduction of Trifluoroleucine. *Biochemistry* **2001,** *40*, 2790–2796.

(149) Ryan, S. J.; Kennan, A. J., Variable Stability Heterodimeric Coiled-Coils from Manipulation of Electrostatic Interface Residue Chain Length. *J. Am. Chem. Soc.* **2007,** *129*, 10255–10260.

(150) Schnarr, N. A. Kennan, A.J., pH Triggered Strand Exchange in Coiled-Coil Heterotrimers. *J. Am. Chem. Soc.* **2003,** *125*, 6364–6365.

(151) Stevens, M. M.; Allen, S.; Sakata, J. K.; Davies, M. C.; Roberts, C. J.; Tendler, S. J. B.; Tirrell, D. A.; Williams, P. M., Ph-Dependent Behavior of Surface-Immobilized Artificial Leucine Zipper Proteins. *Langmuir* **2004,** *20*, 7747–7752.

(152) Naik, R. R.; Kirkpatrick, S. M.; Stone, M. O., The Thermostability of an Alpha-Helical Coiled-Coil Protein and Its Potential Use in Sensor Applications. *Biosens. Bioelectron.* **2001,** *16*, 1051–1057.

(153) Wendt, H.; Leder, L.; Harma, H.; Jelesarov, I.; Baici, A.; Bosshard, H. R., Very Rapid, Ionic Strength-Dependent Association and Folding of a Heterodimeric Leucine Zipper. *Biochemistry* **1997,** *36*, 204–213.

(154) Brunsveld, L.; Folmer, B. J. B.; Meijer, E. W.; Sijbesma, R. P., Supramolecular Polymers. *Chem. Rev.* **2001,** *101*, 4071−4098.

(155) Lehn, J.-M., Supramolecular Polymer Chemistry - Scope and Perspectives. *Polym. Int.* **2002,** *51*, 825−839.

(156) Yan, Y.; Lin, Y.; Qiao, Y.; Huang, J., Construction and Application of Tunable One-Dimensional Soft Supramolecular Assemblies. *Soft Matter* **2011,** *7*, 6385−6398.

(157) Gruber, M.; Lupas, A. N., Historical Review: Another 50th Anniversary—New Periodicities in Coiled Coils. *Trends Biochem. Sci.* **2003,** *28*, 679–685.

(158) Lupas, A. N.; Gruber, M., The Structure of α-Helical Coiled Coils. *Adv. Protein Chem* **2005,** *70*, 37−78.

(159) Ohlson, S.; Strandh, M.; Nilshans, H., Detection and Characterization of Weak Affinity Antibody Antigen Recognition with Biomolecular Interaction Analysis. *J. Mol. Recognit.* **1994,** *10*, 35–138.

(160) Vandermerwe, P. A.; Barday, A. N., Transient Intercellular Adhesion: The Importance of Weak Protein-Protein Interactions. *Trends Biochem. Sci.* **1994,** *19*, 354–358.

(161) Aida, T.; Meijer, E. W.; Stupp, S. I., Functional Supramolecular Polymers. *Science* **2012,** *335*, 813−817.

(162) Lehn, J.-M., Dynamers: Dynamic Molecular and Supramolecular Polymers. *Prog. Polym. Sci.* **2005,** *30*, 814−831.

(163) Hirst, A. R.; Escuder, B.; Miravet, J. F.; Smith, D. K., High-Tech Applications of Self-Assembling Supramolecular Nanostructured Gel-Phase Materials: From Regenerative Medicine to Electronic Devices. *Angew. Chem., Int. Ed.* **2008,** *47*, 8002−8018.

(164) Krieg, E.; Rybtchinski, B., Noncovalent Water-Based Materials: Robust yet Adaptive. *Chem. Eur. J.* **2011,** *17*, 9016−9026.

(165) Oshaben, K. M.; Horne, W. S., Tuning Assembly Size in Peptide-Based Supramolecular Polymers by Modulation of Subunit Association Affinity. *Biomacromolecules* **2014,** *15*, 1436−1442.

(166) Milov, A. D.; Ponomarev, A. B.; Tsvetkov, Y. D., Electron−Electron Double Resonance in Electron Spin Echo: Model Biradical Systems and the Sensitized Photolysis of Decalin. *Chem. Phys. Lett.* **1984,** *110*, 67−72.

(167) Jeschke, G., Deer Distance Measurements on Proteins. *Annu. Rev. Phys. Chem.* **2012,** *63*, 419−446.

(168) Bowman, A.; Hammond, C. M.; Stirling, A.; Ward, R.; Shang, W.; El-Mkami, H.; Robinson, D. A.; Svergun, D. I.; Norman, D. G.; Owen-Hughes, T., The Histone Chaperones Vps75 and Nap1 Form Ring-Like, Tetrameric Structures in Solution. *Nucleic Acids Res.* **2014,** *42*, 6038−6051.

(169) Martin, R. E.; Pannier, M.; Diederich, F.; Gramlich, V.; Hubrich, M.; Spiess, H. W., Determination of End-to-End Distances in a Series of Tempo Diradicals of up to 2.8 Nm Length with a New Four-Pulse Double Electron Electron Resonance Experiment. *Angew. Chem., Int. Ed.* **1998,** *37*, 2833–2837.

(170) Tavenor, N. A.; Silva, K. I.; Saxena, S.; Horne, W. S., Origins of Structural Flexibility in Protein-Based Supramolecular Polymers Revealed by DEER Spectroscopy. *J. Phys. Chem. B* **2014,** *118*, 9881−9889.

(171) Stone, T. J.; Buckman, T.; Nordio, P. L.; McConnell, H. M., Spin-Labeled Biomolecules. *Proc. Natl. Acad. Sci. U.S.A.* **1965,** *54*, 1010−1017.

(172) Keana, J. F. W., Newer Aspects of the Synthesis and Chemistry of Nitroxide Spin Labels *Chem. Rev.* **1978,** *78*, 37–64.

(173) Altenbach, C.; Flitsch, S. L.; Khorana, H. G.; Hubbell, W. L., Structural Studies on Transmembrane Proteins. 2. Spin Labeling of Bacteriorhodopsin Mutants at Unique Cysteines. *Biochemistry* **1989,** *28*, 7806−7812.

(174) Altenbach, C.; Marti, T.; Khorana, H.; Hubbell, W., Transmembrane Protein Structure: Spin Labeling of Bacteriorhodopsin Mutants. *Science* **1990,** *248*, 1088−1092.

(175) Columbus, L.; Hubbell, W. L., A New Spin on Protein Dynamics. *Trends Biochem. Sci.* **2002,** *27*, 288−295.

(176) Smythe, M. L.; Nakaie, C. R.; Marshall, G. R., A-Helical Versus 310-Helical Conformation of Alanine-Based Peptides in Aqueous Solution: An Electron Spin Resonance Investigation. *J. Am. Chem. Soc.* **1995,** *117*, 10555−10562.

(177) Toniolo, C. E. A., Synthesis and Conformational Studies of Peptides Containing Toac, a Spin-Labelled Cα,A-Disubstituted Glycine. *J. Pept. Sci.* **1995,** *1*, 45−57.

(178) O'Shea, E. K.; Klemm, J. D.; Kim, P. S.; Alber, T., X-Ray Structure of the Gcn4 Leucine Zipper, a Two-Stranded, Parallel Coiled Coil. *Science* **1991,** *254*, 539−544.

(179) Oshaben, K. M.; Salari, R.; McCaslin, D. R.; Chong, L. T.; Horne, W. S., The Native Gcn4 Leucine-Zipper Domain Does Not Uniquely Specify a Dimeric Oligomerization State. *Biochemistry* **2012,** *51*, 9581−9591.

(180) Cunningham, T. F.; McGoff, M. S.; Sengupta, I.; Jaroniec, C. P.; Horne, W. S.; Saxena, S., High-Resolution Structure of a Protein Spin-Label in a Solvent-Exposed β-Sheet and Comparison with Deer Spectroscopy. *Biochemistry* **2012,** *51*, 6350−6359.

(181) O'Shea, E. K.; Lumb, K. J.; Kim, P. S., Peptide 'Velcro': Design of a Heterodimeric Coiled Coil. *Curr. Biol.* **1993,** *3*, 658−667.